

**FACULTY  
OF MATHEMATICS  
AND PHYSICS**  
**Charles University**

**DOCTORAL THESIS**

Peter Matvija

**Influence of Si surface passivation on growth  
and ordering of nanostructures**

Department of Surface and Plasma Science

Supervisor of the master thesis: doc. RNDr. Pavel Kocán, Ph.D.

Study programme: Physics

Study branch: Physics of surfaces and interfaces

Prague 2017

I declare that I carried out this master thesis independently, and only with the cited sources, literature and other professional sources.

I understand that my work relates to the rights and obligations under the Act No. 121/2000 Sb., the Copyright Act, as amended, in particular the fact that the Charles University has the right to conclude a license agreement on the use of this work as a school work pursuant to Section 60 subsection 1 of the Copyright Act.

In Prague date .....

signature of the author

Title: Influence of Si surface passivation on growth and ordering of nanostructures

Author: Peter Matvija

Department: Department of Surface and Plasma Science

Supervisor: doc. RNDr. Pavel Kocán, Ph.D.

**Abstract:**

Silicon is currently the most widely used semiconductor material with applications ranging from solar cells and sensors to electronic devices. Surface functionalization of silicon with molecular monolayers can be used to tune properties of the material toward a desired application. However, site-specific adsorption of molecules or molecular patterning on silicon surfaces is a difficult task due to the high reactivity of silicon.

In this work, we use scanning tunneling microscopy, ab-initio calculations and kinetic Monte Carlo simulations to study adsorption of organic molecules on a bare and thallium-passivated Si(111) surface. We show that the polarity of molecules has a large impact on bonding of the molecules with the bare surface. We demonstrate that, in comparison with the bare surface, molecules or single-atom adsorbates deposited on the Tl-passivated surface have significantly higher mobility. The increased mobility induces formation of 2D gases on the surface and enables formation of self-assembled molecular structures. We propose a novel method to directly visualize the 2D surface gases and we show that a phase of surface gases containing molecule-bound dipoles can be controlled by a non-homogeneous electric field.

Keywords: thallium, silicon, self-assembly, phthalocyanine, 2D gas

## Acknowledgments

Before mentioning anybody else, I want to thank my parents. They supported me throughout my whole studies, even though they often did not know what I actually do. I wrote this thesis with an idea that one day I will use it to answer them all the questions they have been asking me so far.

My biggest gratitude goes to my supervisor Pavel Kocán, not only for the useful knowledge I learned from him, but also for his guidance that steered me through my academic life.

I would also like to thank my other colleagues from the group of thin films at Department of Surface and Plasma Science, namely Ivan Oštádal, Pavel Sobotík, Ondřej Krejčí, Filip Rozbořil, Karel Majer, Petr Zimmermann and Michael Kučera. Beside help and knowledge, they were able to provide a pleasant working place, where even an introvert like me was able to feel good.

Last, but definitely not least, I would like to thank my fiancée for her constant support in almost everything I do. This thesis would have never been written without the love that she brings into my life.

# List of papers

## Paper I (page 52)

**Diverse growth of Mn, In and Sn islands on thallium-passivated Si(111) surface**

[1] P. Matvija, P. Sobotík, I. Oštádal and P. Kocán

Applied Surface Science, vol. **331**, pp. 339–345 (2012)

**My contribution:** I performed all the STM experiments. In collaboration with co-authors, I analyzed the data and wrote the manuscript.

## Paper II (page 65)

**Pair correlation function of a 2D molecular gas directly visualized by scanning tunneling microscopy**

[2] P. Matvija, F. Rozbořil, P. Sobotík, I. Oštádal and P. Kocán

The Journal of Physical Chemistry Letters, vol. **8**, pp. 4268–4272 (2017)

**My contribution:** I performed all the STM experiments. In collaboration with co-authors, I analyzed the data and wrote the manuscript.

## Paper III (page 77)

**Electric-field-controlled phase transition in a 2D molecular layer**

[3] P. Matvija, F. Rozbořil, P. Sobotík, I. Oštádal, B. Pieczyrak, L. Jurczyszyn and P. Kocán

Scientific Reports, vol. **7**, p. 7357 (2017)

**My contribution:** I performed all the STM experiments. In collaboration with co-authors, I analyzed the data and wrote the manuscript.

## Paper IV (page 45)

**An STM study of desorption-induced thallium structures on the Si(111) surface**

[4] P. Kocán, P. Sobotík, P. Matvija, M. Setví and I. Oštádal

Surface Science, vol. **606**, pp. 991–995 (2012)

**My contribution:** I participated in the experimental work and the analysis of the measured data.

## Paper V (page 28)

**Chemisorption of Acetophenone on Si(111)-7×7. Polar Aromatic Molecule on Electronically Complex Surface**

[5] O. Krejčí, P. Matvija, P. Zimmermann, P. Sobotík, I. Oštádal and P. Kocán, Journal of Physical Chemistry C, vol. **120**, pp. 9200–9206 (2016)

**My contribution:** I performed all the STM and STS experiments. In collaboration with co-authors, I analyzed the experimental data. I participated in writing of the manuscript.

# Contents

<b>Preface</b>	<b>3</b>
<b>1 Theory of scanning tunneling microscopy</b>	<b>6</b>
1.1 History of STM . . . . .	6
1.2 Quantum tunneling . . . . .	7
1.2.1 Electronic states in solids . . . . .	9
1.2.2 Probability of the single-electron tunneling . . . . .	9
1.3 Tunneling in STM . . . . .	10
1.3.1 Bardeen's tunneling theory . . . . .	10
1.3.2 Tersoff-Hamann theory . . . . .	12
1.4 Scanning tunneling spectroscopy . . . . .	13
<b>2 Experimental apparatus of the STM</b>	<b>16</b>
2.1 Operation of the STM . . . . .	16
2.1.1 Modes of operation . . . . .	16
2.1.2 Limiting factors . . . . .	18
Electrical and mechanical noise . . . . .	18
Thermal drift . . . . .	18
Piezo creep . . . . .	19
Unknown tip apex . . . . .	19
2.2 Our experimental setup . . . . .	19
2.2.1 The ultra-high vacuum system . . . . .	21
2.2.2 Sample preparation . . . . .	21
2.2.3 Deposition of adsorbates . . . . .	22
2.2.4 Temperature measurement . . . . .	22
<b>3 Direct adsorption of molecules on the Si(111) surface</b>	<b>24</b>
3.1 Bulk structure of the silicon crystal . . . . .	24
3.2 The Si(111)-(7 × 7) surface reconstruction . . . . .	24
3.3 Adsorption of acetophenone on the Si(111)-(7 × 7) surface . . . . .	25
3.3.1 Paper V . . . . .	28
3.3.2 Paper V - supplementary information . . . . .	35
<b>4 Thallium passivation of the Si(111) surface</b>	<b>42</b>
4.1 Surface passivation . . . . .	42
4.2 The Si(111)/Tl-(1 × 1) surface . . . . .	43
4.3 Desorption-induced thallium structures . . . . .	43
4.3.1 Paper IV . . . . .	45
<b>5 Single-atom adsorbates on the Si(111)/Tl-(1×1) surface</b>	<b>50</b>
5.1 Growth of Mn, In and Sn layers on the Tl-passivated Si(111) surface . . . . .	50
5.1.1 Paper I . . . . .	52
5.2 Thallium-mediated growth of Si-metal surface reconstructions . . . . .	59

<b>6</b>	<b>Organic molecules on the Si(111)/Tl-(1 × 1)</b>	<b>62</b>
6.1	Phthalocyanines . . . . .	62
6.2	Direct observation of a 2D molecular gas on the Si(111)/Tl-(1 × 1) . . . . .	63
6.2.1	Paper II . . . . .	65
6.2.2	Paper II - supplementary information . . . . .	70
6.3	Electric-field-induced self-assembly of organic molecules on the Si(111)/Tl-(1×1) surface . . . . .	76
6.3.1	Paper III . . . . .	77
6.3.2	Paper III - supplementary information . . . . .	85
	<b>Summary</b>	<b>95</b>
	<b>List of Abbreviations</b>	<b>106</b>
	<b>Nomenclature</b>	<b>107</b>

# Preface

In the past decades we got used to the fact that the computing power of electronic devices is notably increasing every year. This goes hand in hand with the ability to produce smaller and more effective electronic components. However, the decrease of the size is coming to the breaking point. This year (2017), the mass-production of chips with the 10-nanometer transistor size has been announced [6]. By the end of the year 2020, 5 nm transistor size could be commercially available. Even smaller transistors, based on the same technology, would experience quantum tunneling effect, which would impede their proper functioning. The question is, how will we push the size even further after the conventional lithography methods and the Si-based transistor technology will come to their limits.

Molecular self-assembly, using organic molecules as building blocks of spontaneously grown molecular structures, offers a solution to the problem. In the molecular electronic devices, molecules, or groups of the molecules, are foreseen to be designed in a way that they would be able to execute computations internally and would be able to output or store the results. Because of the sub-nanometer size of the molecules, such computations would inevitably include quantum effects. But mastering the manufacture of the quantum molecular devices will probably be a long and gradual process. Some elements essential for the molecular computing, such as molecular switches [7–9], molecular wires [10], molecular motors [11] etc., were already demonstrated in a single-molecule form or a many-molecule but non-addressable form [12]. The biggest difficulty today lies in connecting the molecule-size components to each other or to bulk electrodes in order to form a functional molecular-electronic device. In this regard, direct 'on-chip' combination of the silicon-based and molecular-based electronics seems to be the solution that would enable the use of advantages of both worlds: the world of lithographically prepared semiconductive silicon and the world of self-assembled molecular elements with potential of quantum effects embedded inside.

The process of self-assembly starts after deposition. Initially, deposited molecules are distributed randomly on a surface. The initial positions can be changed and molecules may order only if they are sufficiently mobile after the deposition. The mobility may be directed through weak noncovalent inter-molecular interactions (e.g. hydrogen bonding, metal coordination, van der Waals forces etc.) by tailoring the structure and composition of deposited molecules. As a result of the directed mobility, molecules should self-assemble into desired functional patterns.

Bare semiconductor surfaces are typical for their high density of unsaturated dangling bonds, high reactivity and therefore very low mobility of adsorbates. Most atoms and molecules are fixed by a strong covalent bonds immediately after deposition on the silicon surface. The fixation hinders diffusion of the molecules and their assembly. However, the high reactivity can be suppressed if the dangling bonds are saturated before the deposition of molecules. This process is called surface passivation and in the case of silicon it is usually achieved by deposition of one monolayer of hydrogen [13–15].

In this work, we use passivation by one monolayer of thallium in the reconstruction  $(1 \times 1)$ . Among other passivated surfaces, the  $\text{Si}(111)/\text{Tl} - (1 \times 1)$  [16] has been shown to have outstanding properties such as Rashba splitting of electronic bands [17, 18].

Despite the fact that the surface is stable, inert and with completely saturated surface dangling bonds [19,20], it has never been used as a substrate for molecular self-assembly before.

From all possible adsorbates, metalo-phthalocyanines (MPcs) are the molecules of our choice. MPcs are  $\pi$ -conjugated, square-shaped molecules with a rigid structure and remarkably high thermal and chemical stability [21]. Electronically in a bulk form, most of the phthalocyanines fall into the category of p-type semiconductors with a typical direct band gap of about 1.8 eV [22]. The electronic structure can be significantly altered by substitution of a central transition metal atom and peripheral hydrogen atoms (for instance, fluorination of copper phthalocyanine (CuPc) changes it from a p-type semiconductor to an n-type [23]). Thanks to the variety of electrical and optical properties obtainable by the substitutions, phthalocyanines are ones of the most widely used organic molecules with applications in organic thin-film transistors [24,25], organic light-emitting diodes [26], flexible solar cells [27] etc.

To study the Si(111) substrate, the Tl – (1 × 1) passivation layer and the growth of ordered molecular layers, a combination of experimental and theoretical approach has been used. From the experimental side, we use the scanning tunneling microscopy (STM), which offers real-space and real-time images of the surface with atomic resolution. From the theory side, we use ab-initio calculations and kinetic Monte Carlo (KMC) simulations. Ab-initio methods are used to calculate different static configurations and adsorption energies of the configurations. Comparison of the calculated space structure and the electronic structure of the configurations with STM images and STS spectra allows us to identify exact geometries of the observed configurations. On the other hand, dynamic processes on the surface can be modeled by kinetic Monte Carlo (KMC) simulations. These simulations take input parameters determined by STM or ab-initio calculations and model the time evolution of the surface. This allows us to simulate fast processes that are inaccessible by the relatively slow STM technique.

The thesis is divided into two parts. The first part describes the theory of STM and the experimental apparatus that we use. The second part is devoted to experimental results. The results begin with a study of adsorption of a simple organic molecule - acetophenone - on the Si(111) – (7 × 7) surface (chapter 3, paper V). It shows how the molecular polarity affects adsorption on the electronically complex surface. Results of the paper V are later used to signify differences between adsorption on the bare and Tl-passivated Si(111) surface. The Tl-passivated surface and its thermal and chemical stability are studied in chapters 4 and 5, papers IV and I. In these papers we tackle the problem of the valency of Tl on the surface and the effect of the Tl-passivation on the mobility of single-atom adsorbates, namely Mn, In and Sn. Mobility and self-assembly of organic molecules are studied in the chapter 6, papers II and III. Here, we found out that depending on the temperature and local coverage both molecules of our interest, CuPc and fluorinated CuPc, form a disordered 2D gas phase or ordered solid phase on the surface. We propose a novel method for direct visualization of the 2D molecular gas phase and we show that the STM can be used to induce a 2D-gas/solid phase transition of the molecules on the surface.

My contribution to the work presented in the thesis concerns mainly its experimental aspects. First of all I obtained all displayed STM and STS data. As a first author, I

analyzed and prepared the data for publication in three peer-reviewed papers (papers I, II and III). As a co-author, I carried out all experimental work, including a data analysis, of the paper V. I participated in STM experiments of the paper IV. My part of the work is specified in more details before full-texts of the papers in the main part of the thesis.

# 1. Theory of scanning tunneling microscopy

If you close your eyes and put one finger on the computer keyboard you can tell whether the finger is placed above a button or between two buttons. Pushing the finger against the corrugated surface of the keyboard activates pressure receptors in your skin. The pressure signal is converted to the electrical signal, which is sent to the brain. If the brain had a capability to precisely remember the information, you would be able to map the entire keyboard topography, just by moving the finger across the surface.

The same principle is used in various surface imaging methods falling into the category of scanning probe microscopy SPM. In the SPM, the skin receptors are replaced by atomically sharp tips, the hand muscles are replaced by piezo-ceramics and the brain is replaced by a computer. On top of that, modifications of the tips and detection units of the microscopes allow surface mapping based on the different types of tip-surface interactions, ranging from quantum tunneling to electric and magnetic forces.

In an STM, a sharp metallic tip is brought close to an electrically conductive surface biased at a voltage  $V_{ts}$ . When the tip-surface separation  $d_{ts}$  is small enough, a potential barrier for the electrons reduces to the point when quantum tunneling occurs. The tunneling electrons form electric current whose amplitude exponentially decreases with  $d_{ts}$ . The current is used in the STM feedback to position the tip in a precise distance above the surface. Employing the exponentially dependent tunneling current in the feedback is the key factor that made STM the first method with a real-space atomic resolution and one of the most widespread methods in the present-day surface science. In this chapter, we briefly describe the history of the STM, the physical principles behind STM functioning and the practical issues related to the operation of the microscope.

## 1.1 History of STM

The first successful scanning probe microscope, called topografiner, was constructed by Russell Young in 1972 [28]. The topografiner consisted of the metallic tip mounted on three piezoceramic actuators (see Fig.1.1a). Z-piezoceramic, perpendicular to the surface plane, adjusted the  $d_{ts}$  according to the feedback. Two remaining ceramics provided the lateral scanning motion of the tip. Similarly to its non-scanning predecessor "field emission ultramicrometer" [29], the topografiner employed the field emission current between the tip and the sample for the feedback stabilization of the tip-sample distance. The field emission can work even at large distances, provided the large enough electric field, but it lacks the exponential sensitivity to  $d_{ts}$  [29]. Young was aware of the fact, but was unable to operate the microscope in the direct tunneling regime because of the feedback instabilities in the exponential region [30]. He estimated the ultimate resolution of his apparatus to 0.3 nm perpendicular to the surface, limited by noise, and 20 nm in the lateral direction, limited by a tip radius. The possibility of lateral imaging of individual atoms was not suspected by anyone at the time [31].

Ten years later, the idea of a tunneling microscope was brought to life by Binnig,

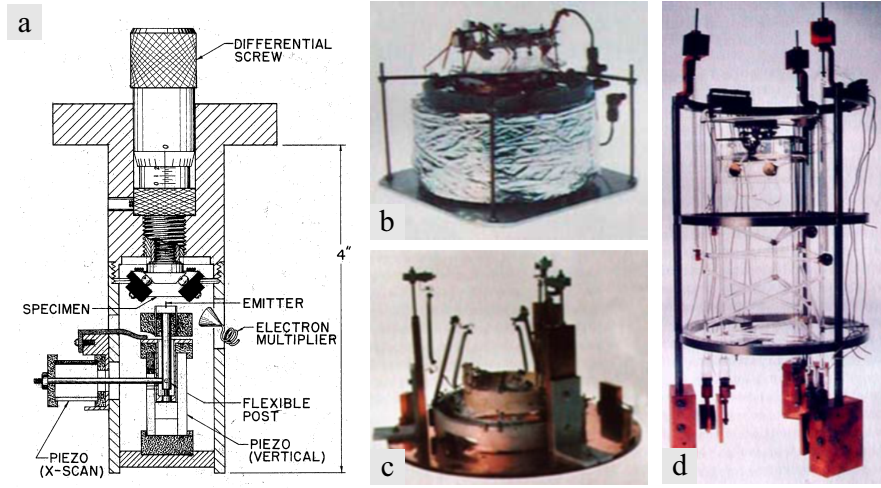


Fig. 1.1: Evolution of the STM between 1971 and 1986. **a:** schematic of the topografiner (reprinted from Ref. [28]). **b, c, d:** first three generations of STM constructed by Binning and Rohrer (reprinted from Ref. [32]).

Rohrer, Gerber and Weibel [33]. Their improvements in the vibration isolation and the feedback control enabled the microscope to achieve the resolution of individual surface atoms. One of the first atomically resolved STM images, the STM image of the Si(111)-(7×7) adatom layer [34], together with the results of X-ray scattering and electron scattering, helped Takayanagi et al. [35] to unfold the dimer-adatom-stacking fault (DAS) model for the Si(111)-(7×7) surface, probably the most intriguing problem of the surface science in the 20<sup>th</sup> century. Shortly after the demonstration of the atomic resolution, Binning and Rohrer were awarded with the Nobel Prize in Physics (1986). The amazing spatial resolution of the STM and the relative simplicity of the method triggered the evolution of further SPM methods, which are now indispensable part of the surface science.

## 1.2 Quantum tunneling

This section provides a brief description of the quantum tunneling effect and electronic states in solids. Conclusions of this section will be used to derive equations of the tunneling process between two solids separated by a vacuum barrier, especially between an STM tip and a sample.

Tunneling is a quantum-mechanical effect that occurs when a particle moves through a classically insurmountable barrier. In classical terms, a particle should not surmount a barrier if the energy of the particle is lower than the height of the barrier. However, in quantum mechanics, particles like electrons have wavelike properties. The waves do not end abruptly at a barrier, but the amplitude of the waves decreases quickly in the region of the barrier. If the barrier is thin enough, there is a non-zero probability to find a particle on the other side of the barrier (see Fig. 1.3).

A simple example of the tunneling is the tunneling of an electron through a potential

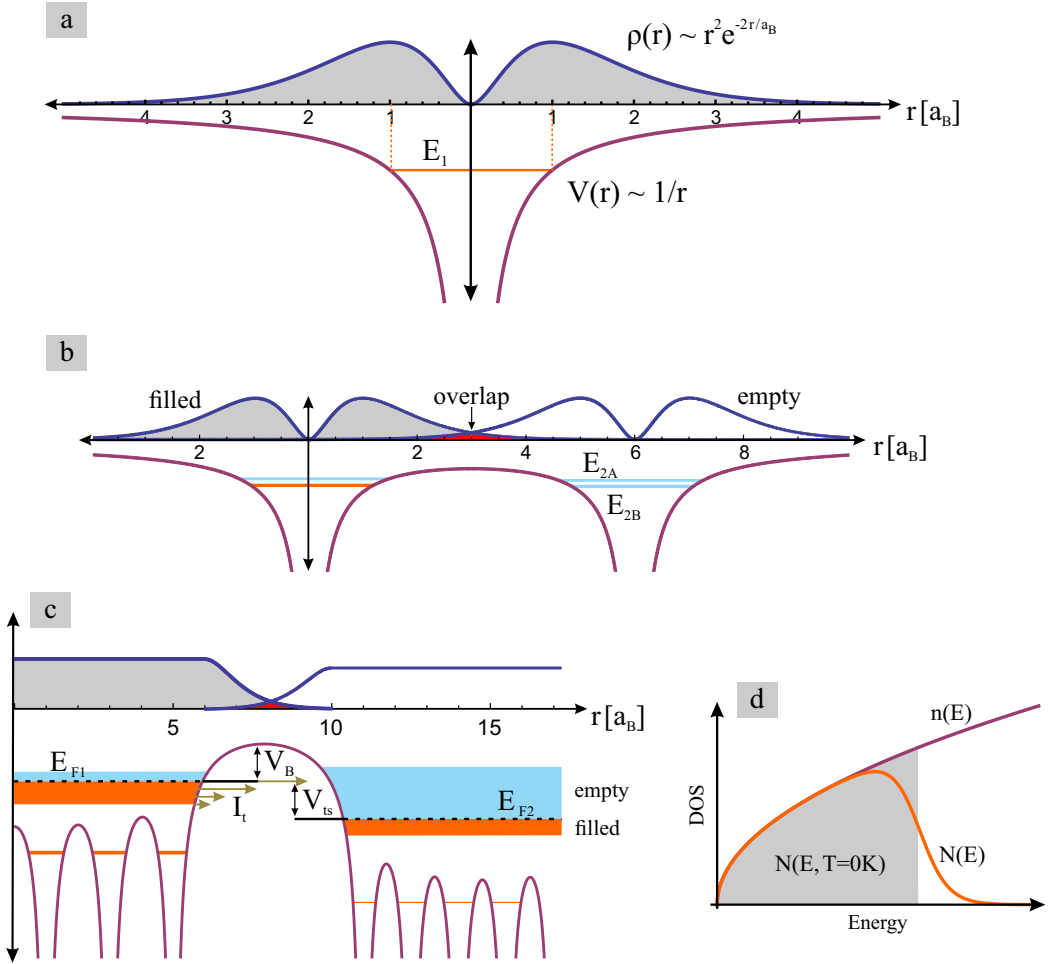


Fig. 1.2: Cross-sections of electron radial probability densities (blue curves) of the 1s orbital in an isolated hydrogen-like atom (a nucleus surrounded by a single-electron cloud) (a), two close hydrogen-like atoms (b) and at a metal-vacuum-metal interface (c). The corresponding electron potentials (in units of energy per electron) are depicted as violet curves at the bottom parts of the panels a, b and c. Panel d depicts density of all states  $n$  and density of occupied states  $N$  in a conduction band of a metal.

barrier between two atomic nuclei, e.g. two hydrogen nuclei, with an electrostatic potential  $V(r) \propto 1/r$  (Fig. 1.2a). When two nuclei approach, the potential changes from  $1/r$  to  $1/r + 1/(r - r_p)$ , where  $r_p$  is the relative position of the nuclei (Fig. 1.2b). Between the nuclei, electron potential barrier emerges. A macroscopic particle would be able to cross the barrier only if its energy was higher than the peak value of the barrier. However, as Fig. 1.2b shows, there is always a non-zero overlap of two neighboring electronic orbitals. Because of the overlap, electrons are able to tunnel through the barrier. Probability of the tunneling is proportional to the overlap. In addition to the tunneling, atomic orbitals split into two molecular orbitals, a bonding orbital  $E_{1B}$  and an antibonding orbital  $E_{1A}$ .

### 1.2.1 Electronic states in solids

In crystals, nuclei are bound into tight lattices. Similarly to two neighboring nuclei, where one energy level splits into two levels, here, if a lattice contains  $m$  atoms, electronic energy levels splits into  $m$  sublevels. For high  $m$ , the close sublevels form quasi-continuously filled intervals of energy, i.e. electronic bands (Fig. 1.2c). The quasi-continuous character of the bands is described by a quantity called density of states (DOS), which is defined as a number of states per interval of energy. A typical DOS of a band in a three-dimensional crystal has a square-root dependence on a difference between the energy of an electron  $E$  and the lowest energy of the band  $E_0$ <sup>1</sup> [36]:

$$n(E) = \frac{1}{2\pi^2} \left( \frac{2m_e}{\hbar^2} \right)^{3/2} \sqrt{E - E_0} \quad (1.1)$$

Electrons available in the crystal fill the states according to the Fermi-Dirac probability distribution function<sup>1</sup> [37]:

$$f_{FD}(E, T) = \frac{1}{e^{(E-\mu)/k_B T} + 1}. \quad (1.2)$$

Metals are special cases of solids whose Fermi level - the energy of the highest occupied state at  $T = 0$  K - lies inside a band. In thermal equilibrium, the number of occupied conduction-band states per a unit volume at a given energy  $E$  above the bottom of the band  $E_c$  can be expressed simply as a product of DOS (1.1) and the Fermi-Dirac distribution function (1.2) (see Fig. 1.2d)<sup>2</sup>:

$$N(E, T) = n(E)f_{FD}(E, T) = \frac{1}{2\pi^2} \left( \frac{2m_e}{\hbar^2} \right)^{3/2} \sqrt{E - E_c} \left( \frac{1}{e^{(E-E_F)/k_B T} + 1} \right). \quad (1.3)$$

Electrons near the Fermi level can space-propagate and enable the flow of electric current in metals.

### 1.2.2 Probability of the single-electron tunneling

In the STM, tunneling occurs at a metal-vacuum-conductor interface between a metallic tip and a conductive sample. At the interface biased at a voltage  $V_{ts}$ , occupied and empty electronic states of the surfaces are on the same energy level, thus electrons from the occupied states can tunnel through the barrier. In order to quantify the probability of tunneling of an individual electron, we assume the 1D case of the barrier with the height  $V_B \gg V_{ts}$ . The barrier can be approximated by a rectangle  $V_B \times d_{ts}$  (see Fig. 1.2 and Fig. 1.3).

A wave function of an electron approaching the barrier with the wave vector

$$k = \frac{\sqrt{2m_e E}}{\hbar} \quad (1.4)$$

can be expressed as a simple plane wave

$$\psi(x) = e^{ikx}. \quad (1.5)$$

---

<sup>2</sup>The following notation is used in the equations:  $n$  - density of states,  $\hbar$  - reduced Planck constant,  $m_e$  - mass of an electron,  $\mu$  - electrochemical potential (often referred to as a Fermi level  $E_F$ ),  $k_B$  - Boltzmann constant,  $T$  - absolute temperature of a system.

To account for possibility of the electron reflection on the left side of the barrier, the wave function changes into the superposition of the plane wave  $e^{ikx}$  and  $e^{-ikx}$ . The same principle applies in the area of the barrier, where the complex exponential function changes to the real exponential function with the decay constant

$$\kappa = \frac{\sqrt{2m_e(V_B - E)}}{\hbar}. \quad (1.6)$$

On the other side of the barrier, electron with the original wave vector  $k$ , but a different amplitude is transmitted. The amplitude can be obtained from the following set of equations

$$\psi_I(x) = Ae^{ikx} + Be^{-ikx} \quad (1.7)$$

$$\psi_{II}(x) = Ce^{i\kappa x} + De^{-i\kappa x} \quad (1.8)$$

$$\psi_{III}(x) = Ee^{ikx} \quad (1.9)$$

if we require the continuity of the wave function and the continuity of the first derivation of the wave function at points 0 and  $d_{ts}$  (for detailed solution see [38]).  $\psi_I$ ,  $\psi_{II}$  and  $\psi_{III}$  represent the wave functions in the areas I, II, III. A, B, C, D and E are the unknown amplitudes of the wave-function components. Ratio of the outgoing amplitude E and the incoming amplitude A determines the tunneling probability of the electron

$$p_T = \left| \frac{E}{A} \right|^2 = \frac{1}{1 + \frac{1}{4} \left( \frac{k}{\kappa} + \frac{\kappa}{k} \right)^2 \sinh^2 \kappa d_{ts}} \propto e^{-2\kappa d_{ts}}. \quad (1.10)$$

For the most metals, with the work function  $\Phi \approx 5$  eV,

$$\kappa \approx \frac{\sqrt{2m_e\Phi}}{\hbar} \approx 10 \text{ nm}^{-1}. \quad (1.11)$$

It means that even the 1 Å thick barrier can change the amplitude of the wave function by one order of magnitude ( $e^{-2 \times 10 \text{ nm}^{-1} \times 0.1 \text{ nm}} \approx 0.1$ ). Over a typical atomic diameter of e.g. 0.3 nm, the tunneling current changes by a factor 1000.

From the relation (1.10), we can see that the tunneling current from a sample to an STM tip, viewed as a flow of non-interacting electrons, is exponentially proportional to  $V_B$  and  $d_{ts}$ :

$$I_t \propto e^{-2\kappa d_{ts}}. \quad (1.12)$$

The two exponential dependencies are crucial for understanding the STM because they determine that the occupied states which are (i) the highest in energy and (ii) the closest to the empty states contribute to the current the most.

## 1.3 Tunneling in STM

### 1.3.1 Bardeen's tunneling theory

The first analytic expression of the tunneling current was introduced in 1961 by John Bardeen [39], who was trying to explain tunneling through superconductor-oxide-superconductor interfaces from a many-particle point of view. A simple way to derive

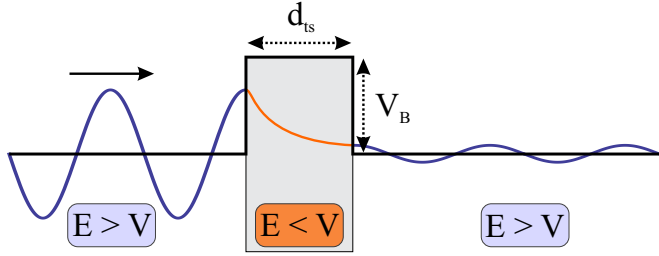


Fig. 1.3: Single-electron quantum tunneling through a potential barrier. Note that after the tunneling, the amplitude of the wave function is decreased, but its frequency remains unchanged.

Bardeen's tunneling theory is to compute electronic states of the two electrodes (E1 and E2) as if they were isolated<sup>3</sup>

$$\hat{H}_1\psi_1(\mathbf{r}) = -\frac{\hbar^2}{2m_e}\Delta\psi_1(\mathbf{r}) + V_1(\mathbf{r})\psi_1(\mathbf{r}) \quad (1.13)$$

$$\hat{H}_2\psi_2(\mathbf{r}) = -\frac{\hbar^2}{2m_e}\Delta\psi_2(\mathbf{r}) + V_2(\mathbf{r})\psi_2(\mathbf{r}). \quad (1.14)$$

Then regard the second electrode as a perturbation of the stationary states of the first electrode  $\hat{H}_1\psi_1(\mathbf{r}) = E_1\psi_1(\mathbf{r})$ . A time evolution of the initial electronic states in the electrode E1 can be written as

$$\Psi_1(\mathbf{r}, t) = \psi_1(\mathbf{r}, 0)e^{E_1 t / i\hbar} + \sum_k a_k(t)\psi_{2,k}(\mathbf{r}), \quad (1.15)$$

where the first term is the time evolution of an initial state without the perturbation and the second term is the sum over all bound states  $\psi_{2,k}$  of the electrode E2 satisfying the equation  $H_2\psi_2(\mathbf{r}) = E_2\psi_2(\mathbf{r})$ . If we assume that (i) tunneling is weak enough so that the first-order Born-Oppenheimer approximations can be applied [40] and (ii) states of the two electrodes are nearly orthogonal, the coefficients  $a_k$  can be evaluated as [41]

$$a_k(t) = \frac{e^{E_1 t / i\hbar} - e^{E_{2,k} t / i\hbar}}{E_1 - E_{2,k}} \langle \psi_{2,k} | \hat{H} - \hat{H}_1 | \psi_1 \rangle, \quad (1.16)$$

where  $\hat{H} - \hat{H}_1$  is a difference between the perturbed and initial Hamiltonians of a tunneling electron. Because probability density  $\rho$  is related to a wave function as  $\rho(\mathbf{r}, t) = |\Psi(\mathbf{r}, t)|^2$ , the rate at which an electron initially in a state  $\psi_1$  of the electrode E1 scatters into a state in the electrode E2 is

$$p_T = \frac{d}{dt} \sum_k |a_k(t)|^2. \quad (1.17)$$

---

<sup>3</sup>The following notation is used in the equations:  $\hat{H}$  - Hamiltonian of an electron in a potential  $V$ ,  $\psi(\mathbf{r})$  - space dependent electron wave function,  $\Psi(\mathbf{r}, t)$  - space and time dependent electron wave function,  $n$  - density of states,  $\hbar$  - reduced Planck constant,  $m_e, e$  - mass and charge of an electron,  $a_k$  - complex expansion coefficients.

Combining (1.16) and (1.17) with Fermi's golden rule [42] gives [41]

$$p_T \approx \frac{d}{dt} \left( \frac{2\pi t}{\hbar} \mathbf{M}^2 n_2(E_1) \right), \quad (1.18)$$

where the matrix element  $\mathbf{M}^2 = \left| \langle \psi_{2,k} | \hat{H} - \hat{H}_1 | \psi_1 \rangle \right|^2$  and  $n_2(E_1)$  is the DOS of the electrode E2 at the initial energy of the electron  $E_1$ . To substitute the matrix element  $\mathbf{M}$ , Bardeen employed a general equation for the probability current density [38]

$$\mathbf{j} = \frac{\hbar}{2im_e} (\psi^* \nabla \psi - \psi \nabla \psi^*). \quad (1.19)$$

integrated over an arbitrary closed surface  $\mathbf{S}$  separating the electrodes:

$$\mathbf{M} = \frac{\hbar^2}{2m_e} \int (\psi_1 \nabla \psi_2^* - \psi_2^* \nabla \psi_1) d\mathbf{S}. \quad (1.20)$$

Knowing the value of  $\mathbf{M}$ , a formula for the tunneling current  $I$  can be obtained from (1.18), if we consider that

$$I_{1 \rightarrow 2} = en_1(E)p_T(E), \quad (1.21)$$

$$I = I_{1 \rightarrow 2} - I_{2 \rightarrow 1} \quad (1.22)$$

and that electrons from occupied DOS of the electrode E1 can tunnel only to empty DOS of the electrode E2 (see eq. (1.3) and Fig. 1.2) [41]:

$$I = \frac{4\pi e}{\hbar} \int_{-\infty}^{\infty} [f_{FD}(E_F + eV_{12} + \epsilon) - f_{FD}(E_F + \epsilon)] n_2(E_F + eV_{12} + \epsilon) n_1(E_F + \epsilon) |\mathbf{M}|^2 d\epsilon \quad (1.23)$$

The formula can be simplified at the limit of low voltages and low temperatures, when  $f_{FD}$  converges to a step function

$$I = \frac{4\pi e}{\hbar} \int_0^{eV_{12}} n_2(E_F + eV_{12} - \epsilon) n_1(E_F - \epsilon) |\mathbf{M}|^2 d\epsilon. \quad (1.24)$$

In other words, if the magnitude of  $\mathbf{M}$  does not vary significantly within the interval  $\langle 0, V_{12} \rangle$ , the tunneling current is given by a convolution of the DOS of the electrodes. Note that throughout the whole derivation we assumed that the tunneling process does not significantly affect the original Hamiltonians of the separated electrodes, i.e. (i) the electron-electron interaction can be ignored, (ii) occupation probabilities for the tip and sample are independent of each other, and do not change, despite the tunneling and (iii) the electrodes are each in electrochemical equilibrium.

### 1.3.2 Tersoff-Hamann theory

So far, we have quantitatively described the quantum tunneling of individual electrons (1.10) and the flow of the tunneling current through the 1D (or planar) rectangular barrier (1.23). After the invention of the STM in early 1980s, a new theory describing the lateral resolution of the STM and the local tunneling in a 3D space was necessary. The first theory that successfully approximated the tunneling process was

published by Tersoff and Hamann [43, 44]. The theory builds on the Bardeen's formula (1.23) and uses the fact that the major part of the current flows only through the outermost atom of the tip. In the original paper, Tersoff and Hamann [44] replaced the unknown electronic structure of the tip by a simple model, in which the outermost atom is assumed to have the spherical s-orbital shape (see Fig. 1.4). To evaluate the matrix element  $\mathbf{M}$ , they expanded the surface wave function in the form<sup>4</sup>

$$\psi_s(\mathbf{r}) = \frac{1}{\Omega_s} \sum_G a_G \times \exp \left[ \sqrt{\kappa^2 + |\mathbf{k}_G|^2} z \right] \times \exp(i\mathbf{k}_G \cdot \mathbf{x}). \quad (1.25)$$

The s-orbital of the tip can be expanded analogously. When the two expressions are inserted into the formula (1.20), the matrix element  $\mathbf{M}$  reduces to<sup>4</sup>

$$\mathbf{M} = \frac{2\pi\hbar^2}{m_e\Omega_t} \text{Re}^{\kappa R} \psi_s(\mathbf{r}_0), \quad (1.26)$$

where  $\mathbf{r}_0$  is the center of the tip s-orbital. For the simple form of  $\mathbf{M}$ , the tunneling current  $I$  can be expressed as [44]

$$I \propto \int_0^{eV_{ts}} n_s(\mathbf{r}_0, E_F - \epsilon) d\epsilon. \quad (1.27)$$

In a limit of small voltages, the expression simplifies to

$$I \propto n_s(\mathbf{r}_0, E_F). \quad (1.28)$$

It means that within the approximations above, an STM image is simply a contour of constant  $n_s(\mathbf{r}, E_F)$  of the surface. The property  $n_s(\mathbf{r}, E)$  is usually referred to as a local density of states (LDOS).

Even though the Tersoff-Hamann model has been very successful, it fails to predict the corrugation amplitudes of atomically resolved surfaces [45]. As Chen in his extension of the STM theory pointed out: "The corrugation amplitude of the LDOS contour of atom-sized features in the Tersoff-Hamann model, even at an extremely short tip-sample distance and with an unrealistically small  $R$ , is still too small to be observable." [46]. The discrepancy arises partly as a result of the oversimplified s-orbital tip modeling. Nowadays, the ever-increasing computing power allows the simulation of STM images with more complex tip structure. Tip apexes can be modeled to have p-, d- or f-orbital shape or their combinations (Fig. 1.4). On top of that, it has been recently shown that even flexible surface-interacting tip apexes are necessary to accurately simulate high-resolution STM images [47].

## 1.4 Scanning tunneling spectroscopy

The equation 1.27 shows that the local electronic properties of surfaces can be probed directly by measuring the dependence of the tunneling current on the tip-sample voltage, i.e. the volt-ampere characteristic (VAC). Differentiating the equation

---

<sup>4</sup>The following notation is used in the equations:  $\psi_s$  - surface wave function,  $\Omega_s, \Omega_t$  - volume of a sample and a tip,  $a_G$  - complex expansion coefficients,  $\kappa$  is defined same as in the relation (1.11),  $\mathbf{k}_G = \mathbf{k}_{||} + \mathbf{G}$ , where  $\mathbf{k}_{||}$  is the surface Bloch wave vector of the wave function and  $\mathbf{G}$  is a surface reciprocal-lattice vector,  $R$  - local radius of tip's curvature about the center located at  $\mathbf{r}_0$ ,  $\mathbf{r} = [\mathbf{x}, z]$ , where  $\mathbf{x}$  is a 2D space vector parallel to the surface and  $z$  is a distance from the surface, .

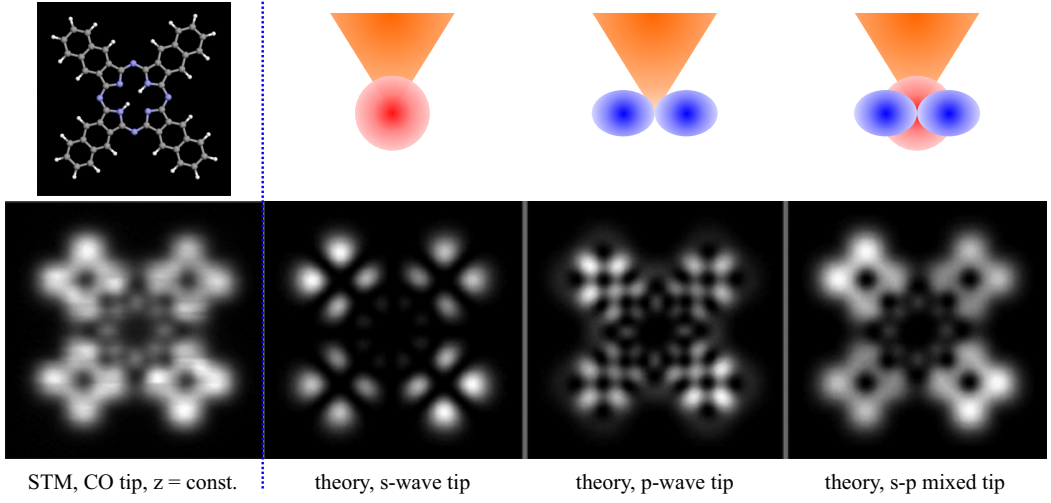


Fig. 1.4: Comparison of the high resolution STM image of naphthalocyanine molecule with Tersoff-Hamann simulation using s-wave tip apex and an extension of Tersoff-Hamann simulation using p-wave and s-p mixed tip apex. Simulated images are reprinted from [48].

leads to the relation

$$n_s(\mathbf{r}_0, eV_{ts}) \propto \frac{dI}{dV_{ts}}, \quad (1.29)$$

where the LDOS is proportional to the derivative of the VAC. In practice, the normalized derivative [49]:

$$\frac{n_s(\mathbf{r}_0, eV_{ts})}{\frac{1}{eV_{ts}} \int_0^{eV_{ts}} n_s(\mathbf{r}_0, E_F - \epsilon) d\epsilon} \propto \frac{\frac{dI}{dV_{ts}}}{\frac{I}{V_{ts}}}. \quad (1.30)$$

is used instead to compensate for a different resistance of a tunneling junction. The derivative  $dI/dV_{ts}$  can be obtained by numerical differentiation of the VAC, however, the differentiation amplifies a noise in the signal. The noise is usually suppressed by a synchronous lock-in detection. In the method, during the measurement of the VAC, a small harmonic signal with amplitude  $V_m$  is superimposed on a tip-sample voltage:

$$V_{ts} = V_{ts0} + V_m \cos(\omega t). \quad (1.31)$$

Harmonic part of the voltage causes oscillations of the tunneling current, with the same frequency  $\omega$  but different amplitude  $I_m$  (Fig. 1.5). A lock-in detector measures the amplitude by suppressing all frequencies of the tunneling current signal that differ from the frequency of the superimposed signal. The derivative of the VAC in the vicinity of  $V_{ts0}$  is then computed as the ratio of  $I_m$  and  $V_m$ .

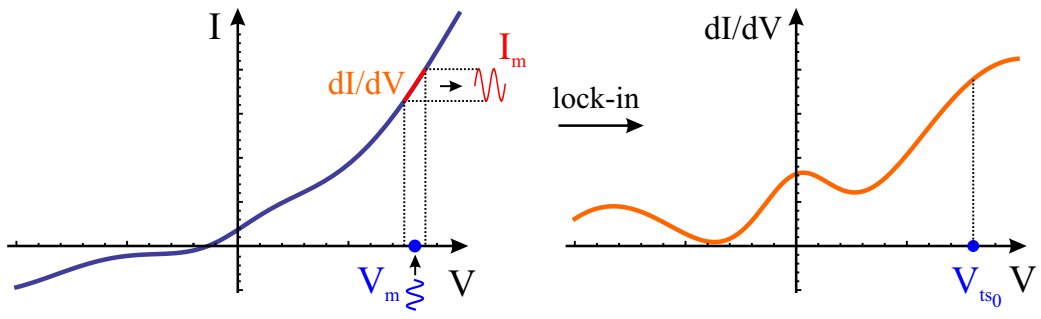


Fig. 1.5: Principle of the synchronous lock-in detection of  $dI/dV$ .

## 2. Experimental apparatus of the STM

In this chapter we briefly introduce the basic experimental aspects of STM and how they affect the measured data. We follow the introduction by the description of our experimental setup and procedures that we use to prepare the apparatus and samples.

### 2.1 Operation of the STM

In the most basic setup, the STM consists only of a conductive tip, an XYZ positioning unit, a sensitive ammeter, a controllable source of voltage and a computer (see Fig. 2.1). When the tip is approached to the surface, the computer reads the value of the tunneling current and compares it with the value of  $I_{set}$  defined by the operator. If  $I < I_{set}$  ( $I > I_{set}$ ), the computer uses the XYZ positioning unit and approaches (retracts) the tip. The positioning unit is usually realized by a piezo-ceramic component (see Fig. 2.1). In this arrangement, contraction (expansion) of the Z ceramics retracts (approaches) the tip, while the scanning motion of the tip is realized by simultaneous applying of the opposite voltage to opposing lateral ceramics.

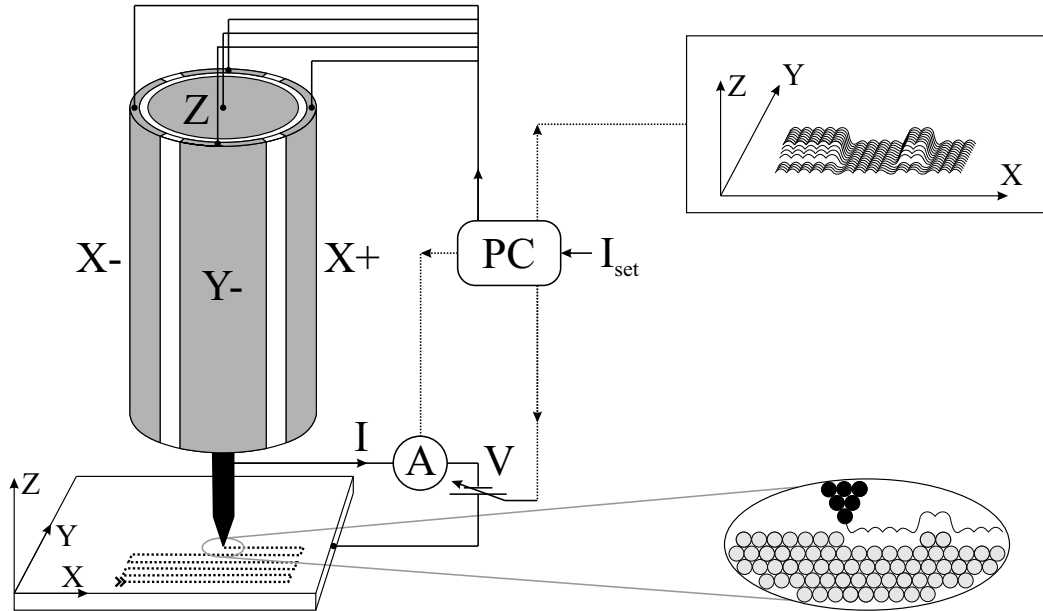


Fig. 2.1: Schematic drawing of the STM feedback mechanism.

#### 2.1.1 Modes of operation

In the STM, the tunneling current is used in the feedback loop to adjust the position of the tip. Depending on the type of the feedback loop, two modes of operation are

commonly used:

### The constant current mode

The tunneling current is stabilized by the feedback at a constant level  $I_{set}$ . The constancy is achieved by adjusting the voltage on the Z ceramic. Surface topography is reconstructed by sampling the voltage applied on the Z ceramic at different coordinates X and Y. Because of the active feedback, the mode can be used even for scanning rough surfaces. On the other hand, the rougher the surface, the slower the scanning has to be in order to give the feedback enough time to avoid the highest surface features.

### The constant height mode

Compared to the previous mode, the scanning speed in the constant height mode may be significantly higher, but only on atomically flat surfaces. The following steps are necessary to operate in this mode. First, the operator needs to approach the surface, to scan a flat area of the surface in the constant current mode and to identify the orientation of the surface plane. Then the operator turns off the feedback loop and switches to the scanning in the identified plane. The distance between the tip and the surface can be adjusted simply by adding an offset to the voltage on the Z ceramic. In this case the tunneling current is not involved in the feedback, but serves as a signal.

Comparison of the two modes is depicted in Fig. 2.2. The constant current mode of the scanning is the predominant mode used in this work. The cases where the constant height mode is used are pointed out in the main text or in the description of figures.

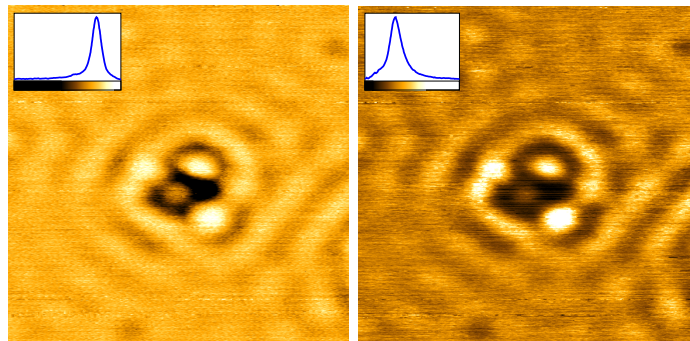


Fig. 2.2: The same area of the surface scanned in the constant current mode (left) and the constant height mode (right). Plots in the top left corners of the images are histograms describing the relative frequency of colors in the images. Different colors represent different heights (in the constant current mode) and different currents (in the constant height mode). Size of the displayed area is 9 nm × 9 nm.

### 2.1.2 Limiting factors

#### Electrical and mechanical noise

A typical width of the tunneling barrier  $d_{ts}$  is about 0.2 nm [50]. Operation of the STM requires stability of  $d_{ts}$  and stability of the lateral position of the tip at sub-angstrom level. Such stability can be achieved thanks to various methods of mechanical damping, like springs, magnetic dampers, laminar flow isolators etc. (see Fig. 2.6e and 2.6f). These methods should contain a combination of low-pass and high-pass mechanical filters, to effectively block most of the outside noise frequencies. From the electrical point of view, the apparatus should be completely isolated from any outside signals, especially the 50 Hz signal from power sockets.

#### Thermal drift

Temperature is another factor that needs to be stabilized during STM measurements. Most solid materials have a linear thermal expansion coefficient  $\alpha_T$  between  $10^{-6}$  and  $10^{-4} \text{ K}^{-1}$ . For instance,  $\alpha_T(\text{Si}) \approx 3 \times 10^{-6} \text{ K}^{-1}$  [51] and  $\alpha_T(\text{steel}) \approx 12 \times 10^{-6} \text{ K}^{-1}$  [52]. If the rigid structure of the apparatus between the sample and the tip is made of materials with different coefficients  $\alpha_T$ , any change of the temperature manifests as a change of the relative position of the tip and the sample. On the basis of this mechanism, two ends of two 1 cm long silicon and iron parts of the apparatus change their relative position by  $\approx 1 \text{ nm}$  if the temperature changes only by 0.01 K. Such a thermal stability is rarely obtained in room-temperature setups, especially when we take into account that the sample is often heated to hundreds of degrees Celsius before the measurement. As a result of the thermal expansion, the effect called thermal drift can be seen in raw STM images (see Fig. 2.3). The drift can be compensated during the measurement or corrected afterwards.

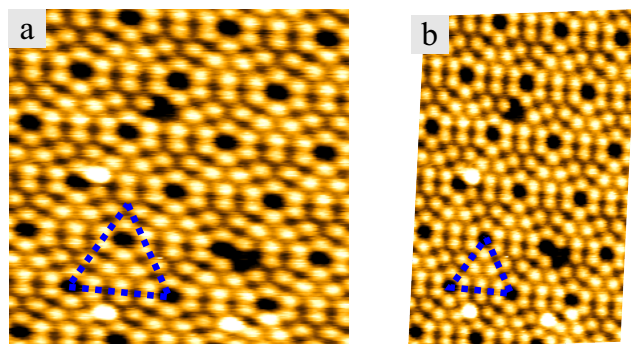


Fig. 2.3: STM image with a thermal drift (**a**) and after the correction of the drift (**b**). Vertices of the blue equilateral triangle should lie in the middle of black spots in the image without the drift.

### Piezo creep

Similar effect as the thermal drift can be caused by XYZ actuators. The actuators usually contain a piezoelectric ceramic material that generates a mechanical strain resulting from an applied electrical field. Internally, the strain originates from partial polarization of crystal domains in the material. If the operating voltage of piezo ceramics is changed, after the voltage change is complete, the remnant polarization continues to change, reflecting itself in a slow creep. In the STM, fast changes of the actuator voltage occur when the operator changes the position of the tip above a surface (in the XY direction, see Fig. 2.4) or after approaching the surface (in the Z direction).

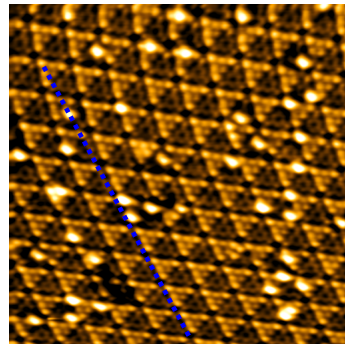


Fig. 2.4: STM image with a piezo creep. The image was taken after a position of the tip above the surface was changed by the operator. The piezo creep manifests as a gradually changing apparent distortion of the triangular symmetry of the surface.

### Unknown tip apex

As has been shown in chapter 1, tip apex has a crucial role in the interpretation of STM images. From the whole tip only the topmost part is involved in the tunneling process, thanks to the exponential dependence of the tunneling current on the tip-sample distance. As a consequence, atomically flat surfaces can be scanned with atomic resolution even with microscopically blunt tips. But the blunter the tip, the higher the probability of the multiple apex formation. Images resulting from scanning with multiple tip apexes contain ghost features, shifted from the main features by the distance  $d_g$  (see Fig. 2.5). This images can be interpreted as a geometric convolution of the tip shape and the sample shape. In the case of rough surfaces, the readability of images is determined by the radius and the roughness of the tip together with the roughness of the sample. Generally, the tip shape is unknown and some caution for spurious tip effects is necessary.

## 2.2 Our experimental setup

The experimental part of this work was performed using the STM apparatus which is placed at the Department of Surface and Plasma Science of the Faculty of Mathematics and Physics of the Charles University. The apparatus is non-commercial.

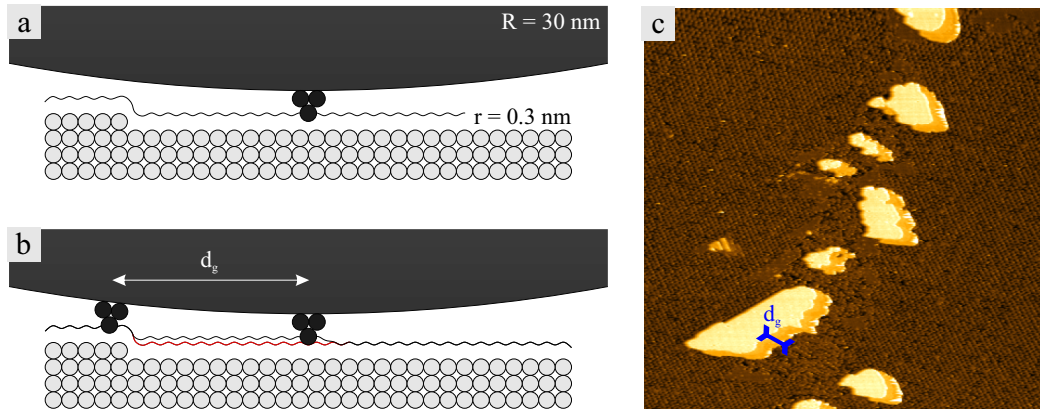


Fig. 2.5: **a:** scale drawing of the tip with the radius 30 nm and the tip apex formed by three atoms with the radius 0.3 nm. **b:** explanation of the multiple-apex artifacts in STM images. Black and red lines mark the real and ideal path of the main tip apex, respectively. **c:** an example of the STM image obtained by a double tip. Size of the displayed area is 140 nm × 140 nm.

Its creator is doc. Ivan Oštádal. The operating software of the apparatus was developed by doc. Pavel Sobotík. In the following sections we describe the parts of the apparatus which are crucial for the preparation of our samples and we present the procedures that are necessary for the preparation of the apparatus before an STM measurement.

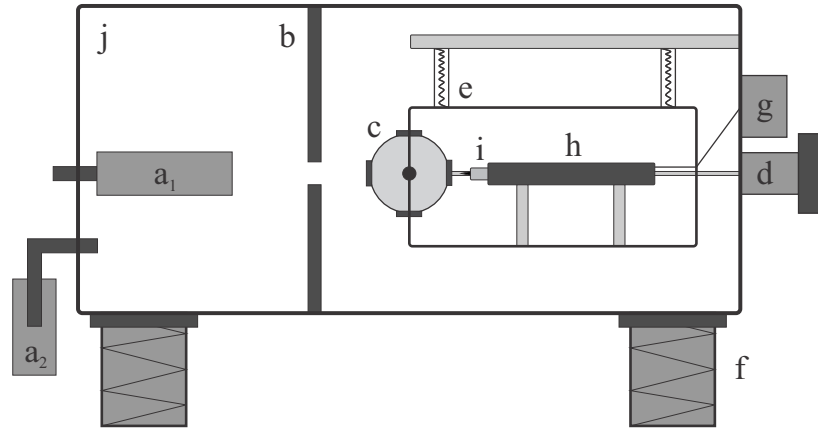


Fig. 2.6: Schematic drawing of our experimental apparatus. **a<sub>1</sub>**, **a<sub>2</sub>**: solid-state and liquid-state evaporation cells, **b**: shading plate, **c**: rotary carousel with samples, **d**: rotary motion feedthrough, **e**: internal cage with mechanical and magnetic damping systems, **f**: laminar flow isolators, **g**: electrical amplifier, **h**: inchworm motor, **i**: piezo-ceramic system with the STM tip, **j**: vacuum chamber.

### 2.2.1 The ultra-high vacuum system

One of the key ingredients of any surface science study is the ability to maintain well-defined conditions of experiments. In this regard, vacuum is an indispensable working environment. It keeps the surface clean and suppresses any undesirable atmospheric influence. The usual rule of a thumb is that it takes about 1 second to cover a surface by contaminants at pressure  $10^{-4}$  Pa. To keep a surface clean during the whole experiment for hours, the pressure lower than  $10^{-7}$  Pa is usually required.

In our apparatus, the ultra-high vacuum (UHV) is maintained by a multi-level pump system which consists of a membrane vacuum pump, a two-level turbomolecular high vacuum pump and a titanium ion pump (see Fig. 2.7). As an additional pumping method, a titanium sublimation is used before each experiment. The base pressure of about  $8 \times 10^{-9}$  Pa is reached after baking the apparatus at a temperature above 125 °C and subsequent degassing of all evaporation cells and samples. Pressure during all presented experiments is sustained within the order of  $10^{-8}$  Pa.

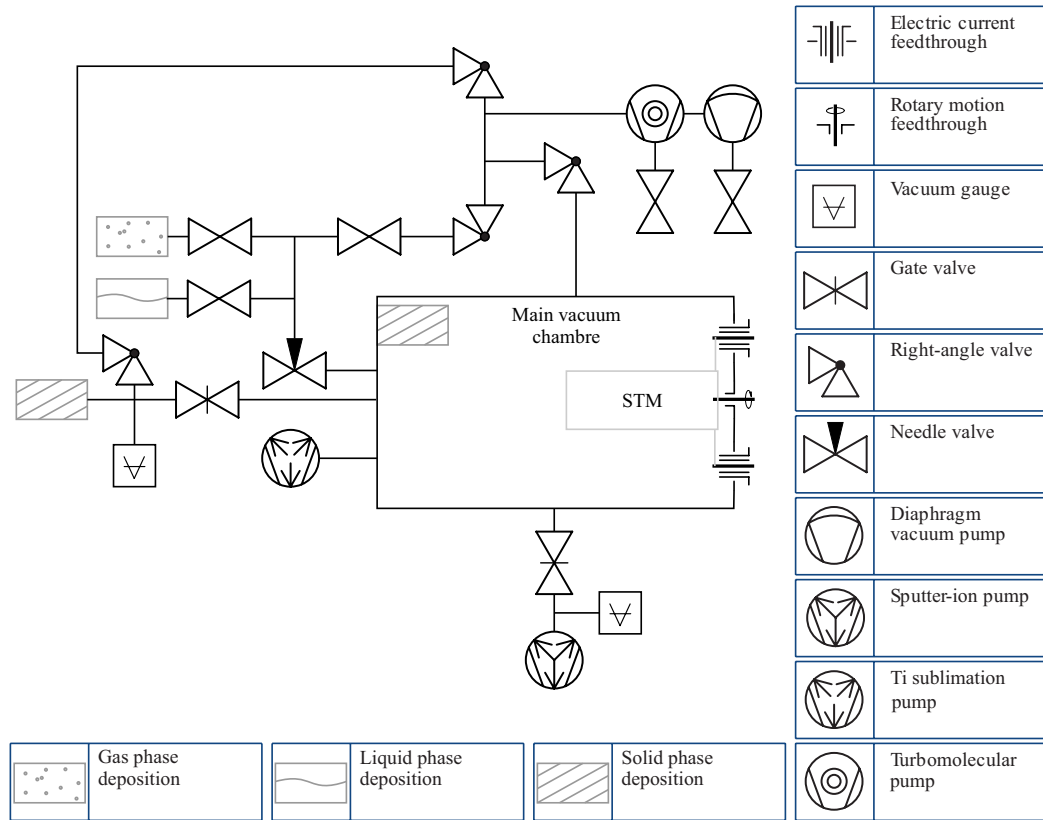


Fig. 2.7: Schematic diagram of the UHV setup.

### 2.2.2 Sample preparation

In all our experiments we use  $0.3\text{ mm} \times 2\text{ mm} \times 8\text{ mm}$  samples cut from Sb-doped Si(111) wafers with resistivity  $0.005 \pm 0.01\Omega\text{cm}$  and miscut  $\pm 0.1^\circ$ . In the apparatus,

samples are firmly attached to the carousel. The rotary motion of the carousel can transfer the samples between two main positions: facing the deposition cells or facing the STM tip. In these two positions, samples can be electrically connected and heated by passing a direct current.

Preparation of the samples before an experiment comprises several steps:

- degassing at  $\approx 600\text{ }^\circ\text{C}$  for  $\approx 12\text{ h}$
- flashing to  $\approx 1200\text{ }^\circ\text{C}$  for  $\approx 10\text{ s}$
- flashing to  $\approx 1200\text{ }^\circ\text{C}$  for  $\approx 10\text{ s}$ , jump decrease of the temperature to  $\approx 900\text{ }^\circ\text{C}$  and slow decrease of temperature from  $\approx 900\text{ }^\circ\text{C}$  to the room-temperature

This procedure leads to the almost perfect  $(7 \times 7)$  reconstruction of the Si(111) surface. The surface can be used for a direct deposition organic molecules or it can be passivated by a layer of Tl. The Tl layer is formed as follows:

- deposition of 1 ML of Tl
- heating the surface for 2 minutes at  $\approx 300\text{ }^\circ\text{C}$

Longer heating at  $\approx 300\text{ }^\circ\text{C}$  or heating at a higher temperature induces desorption of Tl and creation of TlSi- $(\sqrt{3} \times \sqrt{3})$  mosaic reconstruction (see chapter 4 for details).

### 2.2.3 Deposition of adsorbates

Two types of deposition mechanisms are available in the apparatus:

- **Solid phase evaporation**

The evaporation cells are heated by passing of a direct electrical current. Before the deposition, a cell is preheated by the current for up to 10 minutes while the shading plate is closed (see Fig. 2.6). The shading is opened after the stabilization of the deposition rate. We determine the deposition rate and the amount of the deposited material from a thickness quartz monitor. The monitor is calibrated separately for each adsorbate-substrate combination by the STM measurement after deposition of a full monolayer on the surface. We estimate the accuracy of the calibrated values to  $\pm 10\text{ \%}$ .

- **Liquid/gas phase deposition**

A needle valve is used for the controlled exposure of the surface by gasses. The valve separates the vacuum chamber from a tubing which connects the valve to a liquid or gas container. Before the exposure, the tubing is heated and pumped by a turbomolecular pump. The pumped tubing is then filled by a gas or vapors of a liquid. Deposition rate and the amount of a deposited material are estimated from readings of two ion gauges and calibrated afterwards by STM measurements.

### 2.2.4 Temperature measurement

Temperature of the sample was not measured directly during experiments, but indirectly via measuring the power of the electric current used for the heating. As can

be seen on Fig. 2.8, the supplied power and the temperature depends linearly on each other. The linear coefficient of the dependence was calibrated after measurements by placing a thermocouple on the sample. Since the linear coefficients vary up to 15 % from the mean value, we can estimate the temperature of a sample with the accuracy of 15 % even before the calibration of the given sample.

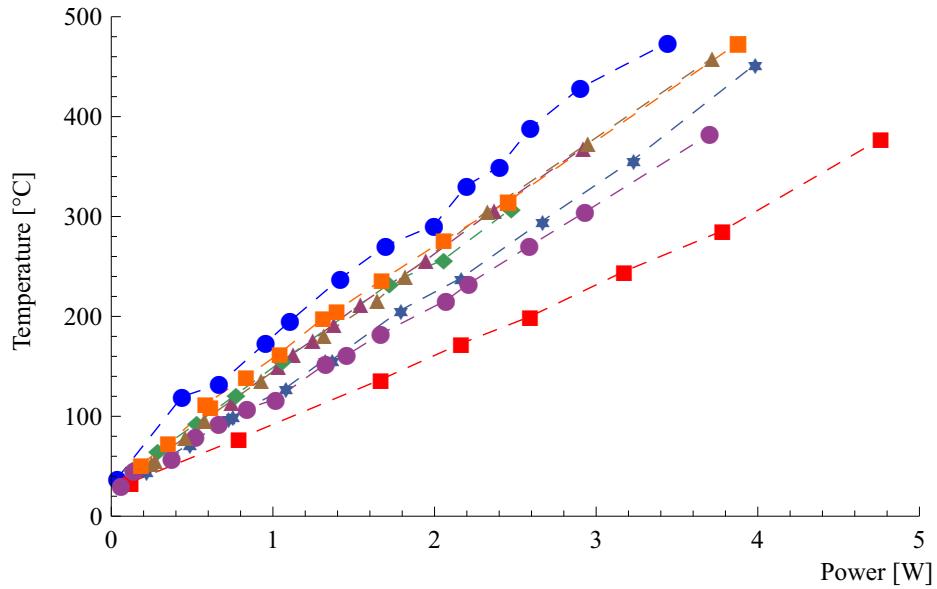


Fig. 2.8: Temperature calibration of different samples [53].

# 3. Direct adsorption of molecules on the Si(111) surface

## 3.1 Bulk structure of the silicon crystal

Silicon is a solid at room temperature, with a melting point of 1410 °C [54]. It crystallizes in the same pattern as diamond, in a structure which can be viewed as two interpenetrating face-centered cubic primitive lattices (see Fig. 3.1). All bulk Si atoms are  $sp^3$  hybridized and form four 0.235 nm long covalent bonds with the neighboring atoms. When a surface is created, a part of the bonds is broken. Depending on the termination of the crystal, the surface has different density of broken (dangling) bonds and different reactivity. Three main bulk-like crystal terminations have the following densities of dangling bonds:  $\sigma_{(111)} = 7.83 \times 10^{14} \text{ cm}^{-2}$ ,  $\sigma_{(100)} = 6.78 \times 10^{14} \text{ cm}^{-2}$  and  $\sigma_{(110)} = 9.59 \times 10^{14} \text{ cm}^{-2}$ . Because of the high densities, silicon surfaces at room temperature reconstruct to energetically more favorable structures. In this work, we use the most stable reconstruction of the Si(111) surface, the  $(7 \times 7)$  reconstruction.

## 3.2 The Si(111)-(7 × 7) surface reconstruction

The Si(111) –  $(7 \times 7)$  reconstruction belongs to the class of dimer-adatom-stacking fault (DAS) reconstructions [35]. It is considered to be one of the most complex but also one of the technologically most important surfaces. The base of the reconstruction is formed by three sets of parallel and equidistant dimer rows which intersect at 60° angles and divide the surface into equilateral triangular areas (see Fig. 3.2). There are two types of the triangular areas - unfaulted and faulted ones - depending on the exact position of the area over bulk Si atoms. Two neighboring triangular areas form a unit cell of the reconstruction.

Each triangular half-unit-cell (HUC) contains 18 surface atoms that are saturated by 6 adatoms. The adatoms remain unsaturated and positively charged, due to the redistribution of the excessive charge to neighboring unsaturated atoms, restatoms. In addition to 9 unsaturated bonds inside the HUC, one dangling bond remains outside the cells in the corner hole. In total, there are 19 dangling bonds per a unit cell, giving the surface density of dangling bonds  $\sigma_{(7 \times 7)} = 3.04 \times 10^{14} \text{ cm}^{-2}$ . Note the density is more than 60 % lower compared to the bulk-terminated surface.

The charge redistribution on the surface significantly affects the chemical reactivity of different sites. A dangling bond of the corner hole atom is saturated by the charge transfer from neighboring fully saturated Si atoms. It usually does not participate in chemical reactions due to its low accessibility. The most reactive sites on the surface are adatoms and restatoms (red and orange in Fig. 3.2) that are respectively positively and negatively charged. The charge results in the generally higher reactivity of adatoms.

The geometric and electronic structure of the  $(7 \times 7)$  surface can be probed by STM. A typical STM image of the surface is dominated by adatoms and corner holes (see in Fig. 3.3). In empty states images (positive surface bias), all adatoms are imaged

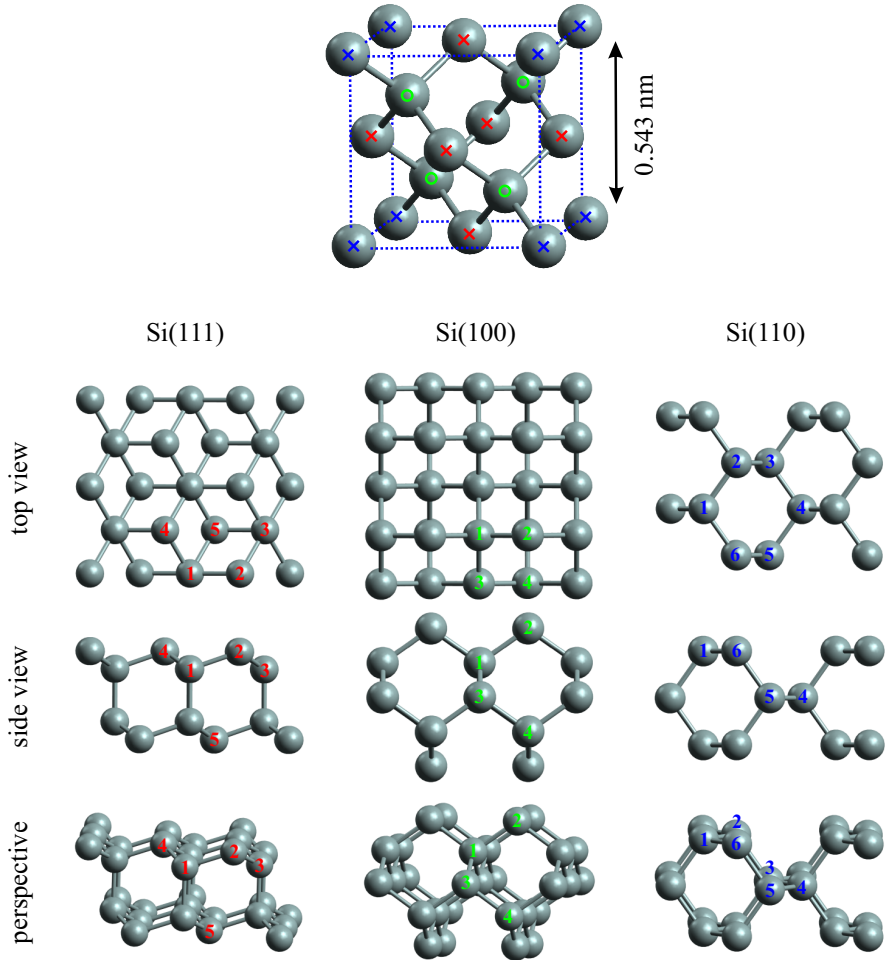


Fig. 3.1: Structure of the silicon crystal and its main surface planes. Top: a unit cell of a silicon crystal. Blue crosses, red crosses and green circles mark equivalent corner, side, and inside atoms of the displayed cell, respectively. Bottom: three main surface planes viewed from top, side and perspective.

with the approximately equal apparent height. The equality is broken in occupied states images (negative surface bias) where (i) the corner adatoms appear brighter than center adatoms and (ii) faulted HUCs appear brighter than unfaulted ones. The faulted HUCs are imaged differently, especially at small negative voltages (up to  $-0.5$  V), because of the higher density of occupied states close to the Fermi level.

### 3.3 Adsorption of acetophenone on the Si(111)-(7 $\times$ 7) surface

Chemisorption of single-atoms [55–60] and small organic molecules [61–66] on silicon surfaces has been extensively studied since the invention of the STM due to the

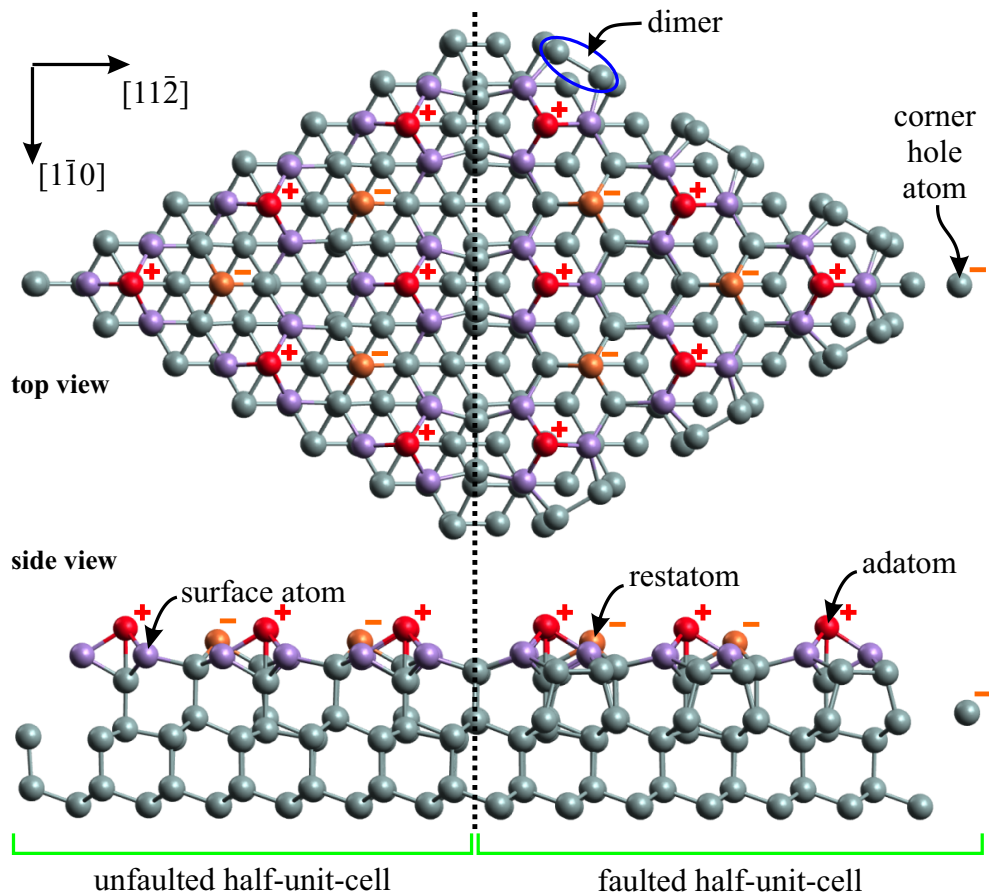


Fig. 3.2: Structural model of the  $(7 \times 7)$  reconstruction. Plus and minus signs indicate charges of atoms.

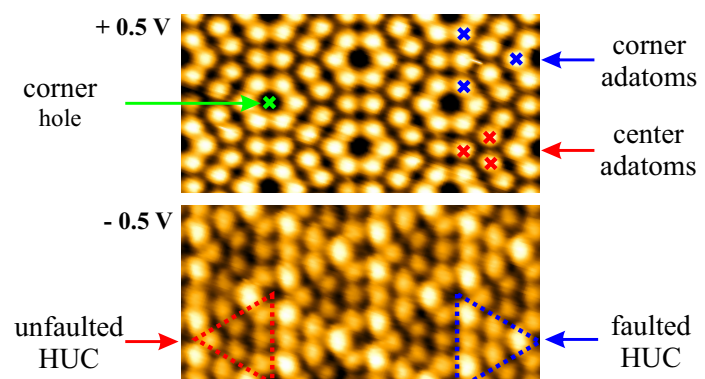


Fig. 3.3: Two STM images of the same area of the  $(7 \times 7)$  reconstruction taken at the opposite sample voltage.

promise of enhancing existing silicon technology with molecular properties such as biosensitivity [67], nonlinear optical response [68] etc. To achieve this goal, one needs to find a molecule that, on one hand, selectively binds to specific sites on the surface and, on the other hand, remains functional after the adsorption. The process of adsorption on the Si(111) – (7 × 7) surface, which can lead to various configurations depending on the structure of a molecule, is not fully understood yet [61, 63, 69, 70]. Because of this, molecules whose adsorption is studied (i) should be small in order to reduce complexity of the problem, (ii) should contain a reactive center that allow specific bonding to the surface and (iii) should be electronically related to more complex molecules used in electronic or optical applications.

In the following study (see paper V, page 28), we chose the smallest aromatic ketone, acetophenone (AP). The ketonic part of the molecule includes the polar C=O group which is reactive and should ensure strong bonding with the substrate. The aromatic part contains delocalized  $\pi$ -orbitals that give rise to a small band gap of the molecule and relate it to the molecules used in opto-electronic applications.

Chemisorption of AP was already studied on the Si(100) surface [66, 71, 72]. It was shown that the most stable adsorption configuration of AP is formed by dissociation of two hydrogen atoms and by bonding to the surface via C–Si and O–Si bonds of the ketonic part.

Compared to the Si(100) surface the Si(111) – (7 × 7) surface provides more spatially and electronically inequivalent reactive sites. Because of the large difference in electron density among atoms containing dangling bonds (see page 24), an adatom coupled with one adjacent rest atom act as a strong dipole. This enables molecules like alkanes or ketones to react with the surface via addition [63, 69]. Other small carbonyl molecules like acetone or acetaldehyd are reported to dissociate on the surface [65, 73].

In the paper V, we show that the adsorption of AP on the Si(111) – (7 × 7) surface qualitatively differs from the adsorption of AP on the Si(100) – 2 × 1 surface and also from the adsorption of other small carbonyl molecules on the Si(111) – (7 × 7) surface. Our detailed STM analysis shows that the most frequent AP structure on the Si(111) – (7 × 7) surface is neither dissociated nor bound to the adatom-restatom pair. We interpret this structure with help of extensive ab-initio simulations and STS measurements as a 1,6-adduct bound to two adatoms in neighboring HUCs. We suggest that the difference between the adsorption of AP and other small organic molecules sources from the presence of a polar carbonyl group in the AP molecule. The strong effect of the molecular polarity on the reaction pathway can be also utilized to direct the adsorption of other functional molecules on the Si(111) – (7 × 7) surface.

My contribution to the paper V consists mainly in STM and STS measurements of the Si(111) – (7 × 7)/AP surface. I carried out three sets of STM measurements: at the room temperature, 75 °C and 150 °C. I identified several irregular and three regular adsorption configurations of AP. I determined the relative occurrence of the adsorption configurations on the surface (see table S2 and Fig. S3 in the Supplementary materials of the paper V). The statistics revealed the most stable adsorption configuration on the surface (the configurations is referred to as object B in the paper V). I measured STS spectra of the two most stable adsorption configurations (Fig. 4 of the paper V). The spectra were used to identify the structure of the configurations. Finally, I prepared the experimental data for the publication and I participated in writing of the manuscript.

## Chemisorption of Acetophenone on Si(111)-7 × 7. Polar Aromatic Molecule on Electronically Complex Surface

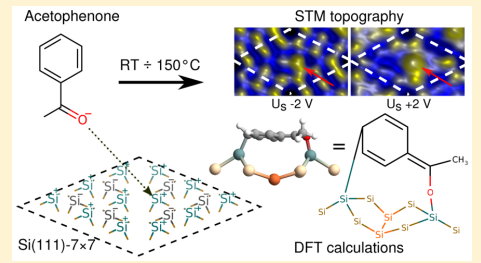
O. Krejčí,<sup>†,‡</sup> P. Matvija,<sup>‡</sup> P. Zimmermann,<sup>‡</sup> P. Sobotík,<sup>‡</sup> Ivan Ošťádal,<sup>‡</sup> and P. Kocán<sup>\*§,‡</sup>

<sup>†</sup>Institute of Physics of the Czech Academy of Sciences, Cukrovarnická 10, 162 00, Prague, Czech Republic

<sup>‡</sup>Charles University in Prague, Faculty of Mathematics and Physics, Department of Surface and Plasma Science, V Holešovičkách 2, 180 00, Prague, Czech Republic

### Supporting Information

**ABSTRACT:** Temperature-dependent chemisorption of acetophenone molecules on the Si(111)-7 × 7 reconstruction was studied by means of scanning tunneling microscopy, scanning tunneling spectroscopy, and density functional theory calculations. A configuration interpreted as a silyl enoether has been repeatedly observed on the surface at room temperature and after annealing to 75 °C. The most frequent structure on the surface stable up to 150 °C is identified as a 1,6-adduct to two adatoms of the neighboring half unit cells. The results suggest that presence of the polar group in the molecule affects the chemisorption in a way that leads to bonding with two adatoms.



### INTRODUCTION

The chemisorption of small organic molecules on silicon surfaces has been extensively studied<sup>1–11</sup> due to the promise of enhancing current silicon technology with interesting electronic or optical properties of the molecules. For potential utilization of the surfaces with suitable molecules one has to deal with an uneasy task of finding a surface structure that would bind a molecule strongly enough to form a stable configuration while the adsorbed molecule should have properties that would allow using it as a functional element. In order to find suitable molecules, it is necessary to understand how various functional groups affect the adsorption of the molecules on different substrates. The interplay between atomic and electronic structure of surfaces and various functional groups of molecules, which leads to different chemisorption patterns, is not fully understood yet.<sup>3,6,11</sup> The studied precursor molecules should have properties that allow very specific binding to the surface and at the same time they should be electronically related to more complex molecules designed for electronic or optical applications.

Aromatic ketones are promising for the following reasons. The aromatic part of the molecules evinces a small gap because the highest occupied molecular orbital (HOMO) and the lowest unoccupied molecular orbital (LUMO) are delocalized  $\pi$ -orbitals. On the other hand, the polar C=O group of the ketonic part is highly reactive and ensures strong bonding to the semiconductor surface.<sup>5,11</sup>

For this study, we chose the smallest aromatic ketone, acetophenone (hereafter AP for short, schematic formula shown in the Figure 2e). The chemisorption of AP has been already studied on the Si(100) surface using scanning tunneling microscopy (STM),<sup>7</sup> near-edge X-ray adsorption spectroscopy

py,<sup>9</sup> and density functional theory (DFT) calculations.<sup>7,8</sup> On the Si(100) surface, the most stable chemisorbed configuration of AP is formed by dissociation of two hydrogens (that bind to the surface) and by bonding to the surface via C-Si and O-Si bonds of the molecule ketonic tail.<sup>7,9</sup>

As a substrate, we used the 7 × 7 dimer-adatom-stacking fault reconstruction<sup>12,13</sup> of the Si(111) surface (hereafter 7 × 7 for simplicity). Compared to the Si(100) surface, the 7 × 7 has more complex structure and contains different reactive sites that can interplay in the molecular chemisorption. The ball and stick model of the whole 7 × 7 cell is shown in Figure 1. The 7 × 7 cell consists of two half unit cells (HUC). HUCs are separated by the dimer rows (orange atoms in Figure 1) and the corner holes. A dangling bond of the corner hole atom (violet in Figure 1) is saturated by a charge transfer, thus the atom is negatively charged. It usually does not participate in chemical reactions due to its low accessibility. The most reactive sites of the cell are 12 adatoms (blue in Figure 1) and six restatoms (gray in Figure 1).<sup>14</sup> The restatom dangling bonds are fully saturated via charge transfer from adatoms, therefore restatoms are negatively charged. The charge transfer also results in partially positively charged adatoms with each dangling bond containing only ~5/12 of electron.<sup>15</sup> The charge of adatoms, restatoms, and the corner hole atom is indicated by "+" and "-" symbols in Figure 1. The unsaturated dangling bond results in general in higher reactivity of the adatoms. However, some atomic adsorbates, like hydrogen, prefer restatoms over adatoms.<sup>16</sup> The other Si atoms of the

Received: January 15, 2016

Revised: April 6, 2016

Published: April 7, 2016

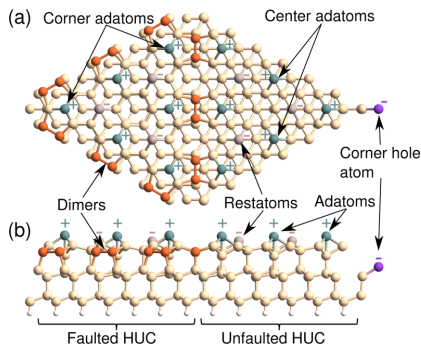


**Figure 1.** Si(111)-7 × 7 DAS surface reconstruction<sup>12,13</sup> as used in the DFT calculations. (a) Top view, (b) side view. The 7 × 7 slab is passivated by a hydrogen (white ball) layer from the bottom. Symbols “+” and “−” indicate charge of the atoms with dangling bonds.

reconstruction have four  $\sigma$ -bonds, thus their bonding capacity is fully saturated. Therefore, these atoms are much less reactive and they do not play an important role in adsorption.

There are two common reaction patterns of small carbonyl molecules on the 7 × 7. First, molecular decomposition, reported in the case of saturated carbonyl molecules: acetone loses the hydrogen at 250 K<sup>10</sup> and acetaldehyde dissociates at 350 K.<sup>1</sup> Second, addition to the adatom and restatom, which was identified for unsaturated ethyl-vinyl-ketone<sup>6</sup> that undergoes 1,4-addition (in ref 6 denoted as [4 + 2]-like cycloaddition).

In this paper, we show that the adsorption of AP on the Si(111)-7 × 7 qualitatively differs from the adsorption on Si(100)-2 × 1 surface and also from the adsorption of the smaller carbonyl molecules on the 7 × 7. Our detailed STM analysis shows that the most frequent AP structure on the 7 × 7 (in our discussion referred to as object B) is neither dissociated nor bound to the adatom–restatom pair. This structure, observed by STM in a temperature range from room temperature (RT) to 150 °C, was explained with help of extensive DFT simulations and scanning tunneling spectroscopy (STS) measurements as a 1,6-adduct bound to two adatoms in neighboring HUCs. We put it in contrast to a similarly sized but nonpolar styrene molecule,<sup>3,4</sup> which has been reported to be added to the adatom and restatom via 2,8-addition (in refs 3 and 4 denoted as [4 + 2]-like cycloaddition). We suggest that the presence of carbonyl group in the AP molecule and its polarity plays an important role in the studied chemisorption.

## PROCEDURES

**Experimental Procedures.** Experiments were carried out in an ultrahigh vacuum chamber (a base pressure below  $8 \times 10^{-9}$  Pa) equipped with a noncommercial STM. Silicon substrates were prepared from Sb doped wafers (resistivity 0.005–0.01 Ω cm). The 7 × 7 reconstruction was obtained by a standard flashing procedure. Pressure during the substrate preparation was sustained within the order of  $10^{-8}$  Pa. AP was deposited via a leak valve from the liquid phase, which was purified by several freeze–pump–thaw cycles prior to the experiment. During the exposition, the pressure of AP was held in the order of  $10^{-6}$  Pa. The purity of the AP was confirmed by deposition onto the Si(100) surface with recognition of the

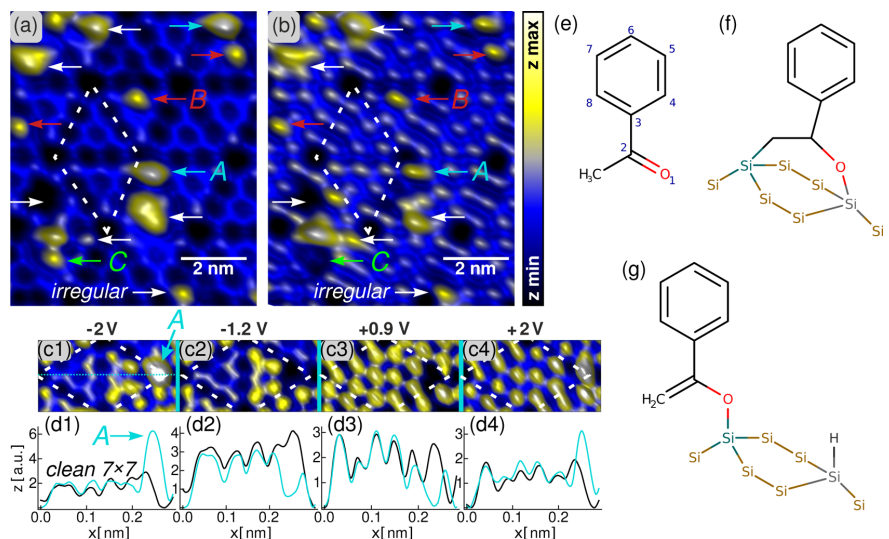


**Figure 2.** AP/Si(111)-7 × 7 surface after annealing to 75 °C. (a,b) STM images of the surface taken at the sample bias: −1.75 V and +1.75 V, respectively (tunneling current 0.5 nA). Blue, red, and green arrows mark positions of objects found after AP exposition. We name them as A, B, and C, respectively. White arrows indicate irregular objects. Series of detailed STM images of the object A taken at different biases is shown in (c). The 7 × 7 cell is indicated by a dashed line. The series of line profiles taken over diagonal of the 7 × 7 cell with the A object (dotted blue line in c1) and of the clean 7 × 7 cell, respectively. (e–g) Schematic chemical formulas: (e) acetophenone molecule (with atom numbering), (f) 1,2-adduct with consecutive interconversion and hydrogen migration, and (g) adatom-bound silyl enoether. The adatoms are depicted in blue, while restatoms are depicted in gray.

same structures as published by Schofield et al.<sup>7</sup> The data for the STM images were processed by a floating average filter and are shown in the pseudo-3D view mode.<sup>17</sup> The  $dI/dV$  scanning tunneling spectra were measured using a lock-in technique, the presented data were averaged over several equivalent spectra normalized by  $I/V$ .

**Theoretical Procedures.** The geometry optimizations were performed with DFT using the Fireball<sup>18</sup> code, which is based on the formalism of the local combination of atomic orbitals,<sup>19</sup> norm-conserving pseudopotentials,<sup>20</sup> and the McWEDA functional.<sup>21</sup> The exchange-correlation energy was calculated using the local density approximation<sup>22</sup> with the Perdew-Zunger parametrization<sup>23</sup> of the correlation energy of a homogeneous electron gas calculated by Ceperley-Alder.<sup>24</sup>

The Fireball DFT calculations were done with a full  $7 \times 7$  slab that contained a total of six layers of Si and a vacuum gap of 9.0 nm. A layer of hydrogen was attached underneath the slab to passivate the surface. The two bottom layers of Si and the layer of H were fixed during the geometry optimizations. For the Brillouine zone sampling, we used the  $2 \times 2$  Monkhorst-Pack grid.<sup>25</sup> The slab calculations enable a much better description of the  $7 \times 7$  states in comparison with small cluster calculations.

In order to confirm the densities of states obtained from the Fireball, we performed a single point calculations with VASP DFT package<sup>26</sup> using more precise generalized gradient approximation-PW91 functional.<sup>27</sup> For these calculations, we used a slab containing four Si layers, a passivating hydrogen layer, and 1 nm of vacuum above.

The used basis sets and energy cut-offs are stated in the Supporting Information.

## RESULTS AND DISCUSSION

We carried out RT STM measurements of the adsorbed AP on the  $7 \times 7$  surface ( $AP/7 \times 7$ ) after three different postdeposition thermal treatments: without annealing and with annealing to 75 and 150 °C in order to distinguish metastable and stable adsorption geometries on the surface. Observation of the AP-exposed samples without annealing revealed, as we expected, that AP chemisorbs already at RT (Figure S2 in the Supporting Information). Multiple objects can be found on the surface after AP exposure and most of them are stable up to 75 °C. A representative STM image of the  $AP/7 \times 7$  surface after annealing to 75 °C is shown in Figure 2a,b. A majority of objects found on the surface can be classified as irregular (white arrows in Figure 2a,b). They usually appear as protrusions at sample biases  $U_S < -1$  V and as protrusions or depressions at  $U_S > 1$  V. At  $|U_S| < 1$  V, the irregular objects are imaged as a depression in the position of a single adatom or couple of adatoms. The irregular objects are often spread over several neighboring adatoms and we consider them as composed of multiple adsorbed AP molecules or as rare adsorption configurations of a single AP molecule. We note that these structures are only metastable and disappear after annealing to 150 °C.

Besides the irregular structures, three frequently observed types of objects can be distinguished on the surface after annealing to 75 °C, denominated A, B, and C (blue, red, and green arrows in Figure 2a,b, respectively). Results of the statistical analysis of the observed objects are shown in table S1 in the Supporting Information. The B object is the most frequent regular object on the surface and together with the object C is stable even after annealing to 150 °C. The

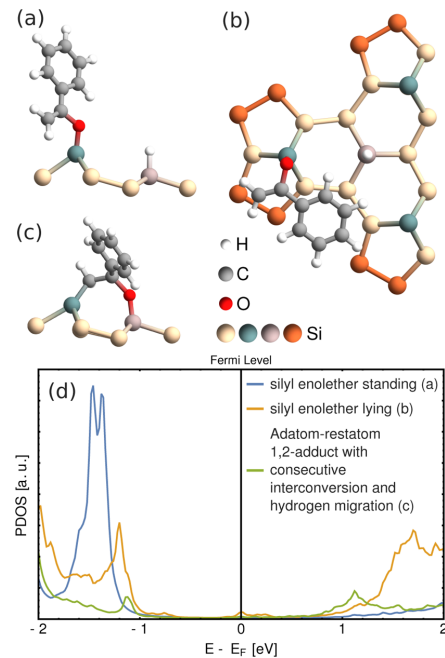


**Figure 3.** Relaxed candidate adsorption geometries of the A object: (a) adatom-bound standing silyl enoether, (b) adatom-bound lying silyl enoether, and (c) 1,2-adduct with consecutive interconversion and hydrogen metathesis. (a,c) Side views, (b) top view. Color scheme of the silicon atoms is the same as in the Figure 1. (d) The molecule projected densities of states (PDOS) for the adsorption geometries (a–c).

properties and atomic structure of B and C objects will be discussed in detail later. Unlike the B and C objects, the A object is only metastable since it is not observed after annealing to 150 °C.

Bias-dependent details of imaging the A object are presented as STM maps in Figure 2c. In addition, line profiles taken at corresponding tip voltages over a  $7 \times 7$  cell containing an object A and over a clean  $7 \times 7$  cell are shown in Figure 2d. The object appears as the brightest feature in the STM images taken at negative biases  $U_S < -1.3$  V (e.g., Figure 2c1,d1). For  $U_S$  between  $-1.2$  and  $+0.9$  V it completely disappears (e.g., Figure 2c2,c3,d2,d3), thus it looks like missing adatom. After increasing the bias above  $+0.9$  V, it appears as a slightly more enhanced and laterally shifted adatom (shown in the Figure 2c4). The shift is even more pronounced in the line profile in Figure 2d4. The closest restatom is missing on the images taken at  $U_S < -0.9$  V (e.g., Figure 2c1,c2), which indicates that the AP molecule or its part are bound to the restatom.<sup>2,16</sup>

By means of DFT calculations, we searched for AP surface configurations consistent with STM imaging of the object A, i.e. 1) saturating dangling bonds of the adatom and the restatom and 2) with a low density of states in the range from  $-1.2$  eV to  $+0.9$  eV. We found three geometries of the chemisorbed AP molecule meeting the criteria: A silyl enoether (a schematic formula in Figure 2g), which has two stable geometries, “standing” or “lying”, and a 1,2-adduct with consecutive interconversion and hydrogen migration (schematic formula

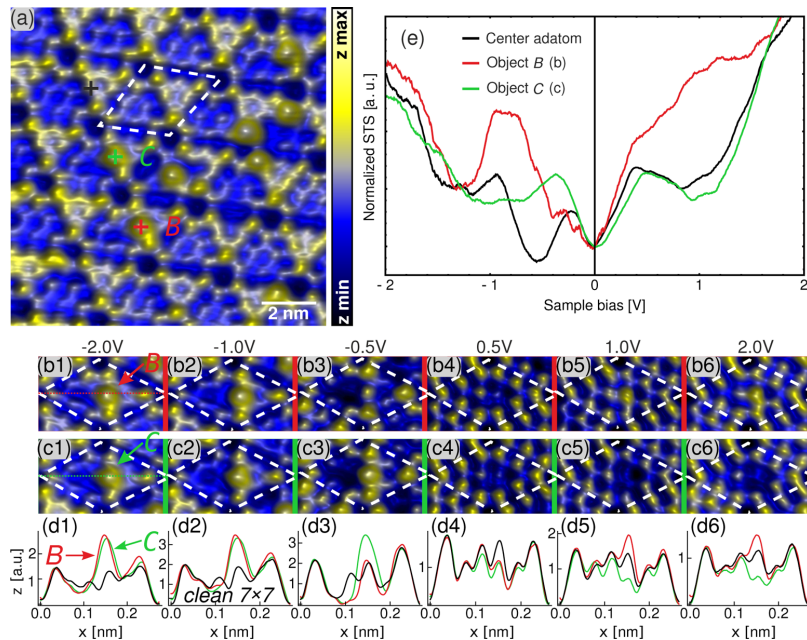


**Figure 4.** AP/Si(111)-7 × 7 surface after annealing to 150 °C. (a) An STM image of the surface at the sample bias: −1.0 V (tunneling current 0.085 nA). Red and green crosses indicate positions of the objects B and C, whose detailed STM images taken at different biases are shown in (b) and (c), respectively. The black cross marks position of a center adatom. The 7 × 7 cell is indicated by a dashed line. The series of the line profiles taken above the longest diagonal of the 7 × 7 cell containing the B object (red line), the C object (green line), and above the clean 7 × 7 cell (black line) is shown in (d). The actual location of the line profile taken above objects B and C is marked out by red and green dotted lines in (b1) and (c1), respectively. (e) STS curves measured above center adatom (black line) marked by black cross in (a) and objects B (red line) and C (green line).

in Figure 2f). The corresponding relaxed geometries are shown in Figure 3a–c and molecule projected densities of states (PDOS, for more information see the Supporting Information) are shown in Figure 3d.

The silyl enoether lying geometry is the most stable one, according to the Fireball calculations, however we suppose that the stability of this geometry can be overstated in our calculations due to the BSSE error.<sup>28</sup> Another support for the silyl enoether geometry can be obtained from STM images: The protrusion in the STM images of the object A (shown in Figure 2c1,c4) is positioned always above the adatom, slightly shifted in the direction to the neighboring HUCs. If the A object were the 1,2-adduct, which is situated above the adatom and the restatom, the corresponding protrusion in STM image would be shifted to the restatom. Therefore, we consider the silyl enoether as the more probable adsorption model for the A object. We note that switching between both chemically identical silyl enoether geometries can be also possible at RT. However, due to the similar PDOS of both geometries the switching cannot be observed by means of simple STM imaging. This type of adsorption was observed previously in the case of acetone on the 7 × 7.<sup>10</sup> The dissociated hydrogen is bound to the restatom which is the preferred position for the hydrogen on the 7 × 7 and it causes disappearance of the restatom at  $U_S < -0.9$  V.<sup>16</sup>

A representative STM image of the AP exposed surface after annealing to 150 °C is shown in Figure 4. The metastable irregular objects as well as the objects A are no more observed on the sample. For the latter one, we do not expect desorption

via Si–O bond scission but rather transformation into some other undistinguished structure. Bias-dependent STM details of the objects B and C are shown in Figure 4b,c, respectively. The direct comparison of the line profiles taken at corresponding voltages above the clean 7 × 7 cell and the cells containing B or C object is shown in Figure 4d. Both objects appear very similar in the STM images at negative sample biases  $U_S \leq -1$  V, that is, as bright protrusions at the adatom positions (as shown for example in Figure 4b1,b2 and c1,c2). At negative sample biases  $U_S > -1$  V (e.g., Figure 4b3,c3,d3), the objects have at least the same brightness as unreacted adatoms. The main difference between B and C objects arises at  $U_S \geq 1$  V (see Figure 4b5,b6 and c5,c6, respectively). At these biases, the B and C objects appear as a protrusion and a depression, respectively. That can be also seen from the line profiles in Figure 4d5,d6. We note that the protrusions corresponding to B and C objects are usually shifted in direction toward the neighboring HUC, which is the most prominent at  $U_S \leq -1$  V. At positive biases, the contrast of the closest adatom in the neighboring HUC is almost unaffected in the case of the B object, while in the case of the C object the adjacent adatom is considerably darker.

We performed STS measurements above the stable B and C objects in order to specify differences in the electronic structure (see Figure 4e). While the contrast of STM images reflects geometry and also all electronic states between applied bias and zero bias (= the energy of the Fermi Level), the normalized tunneling spectra are roughly proportional to the local density of states.<sup>29</sup> The spectrum of the B object (red line in Figure 4e) indicates a high density of states at −0.7 and +1.0 eV. In the

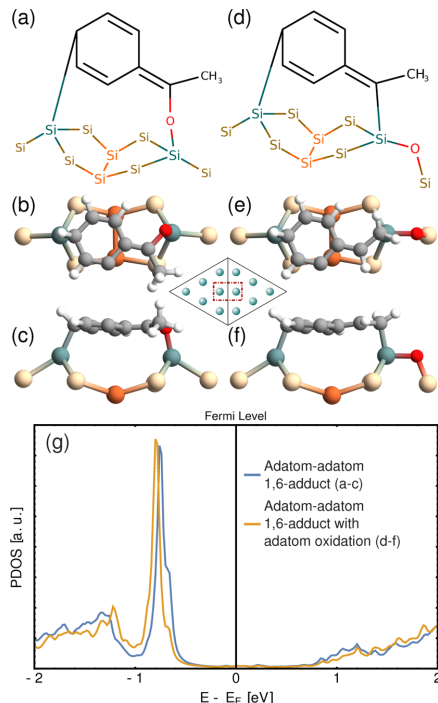


**Figure 5.** Candidate adsorption geometries of the *B* object: (a–c) 1,6-adduct of the AP, (d–f) 1,6-adduct with adatom oxidation. (a,d) Schematic formulas, (b,e) top views, and (c,f) side views. The atoms are colored as in Figure 1 and 3. The inset in the middle: Schematic drawing of the  $7 \times 7$  reconstruction with adatoms shown only. The red dashed-dotted rectangle marks out the area shown in the panels a–f. (g) The molecule projected densities of states (PDOS) of the adatom–adatom adducts. Blue line is the density of the 1,6-adduct, whereas yellow line represents the density of the 1,6-adduct with adatom oxidation.

case of the object *C* (green line in Figure 4e), the spectrum shows an increased density at  $-0.5$  eV, compared to an unreacted adatom (black line in Figure 4e), and a lower density of states above the Fermi Level up to  $2$  eV. The lower density of unoccupied states explains disappearance of the object in the STM empty-state images (Figure 4c4–c6).

Extensive DFT calculations were used to select adsorbate–surface configurations corresponding to the experimentally obtained properties of the object *B*. A stable configuration with high bonding energy and PDOS consistent with the tunneling spectra<sup>29</sup> in Figure 4b were required. In addition, the configuration should have a low formation barrier because it is commonly observed already on samples exposed to AP at RT. Geometries with a datively bound AP molecule to a single Si adatom or restatom (figure S1 top left in the Supporting Information) could be ruled out as energetically unfavorable, thus we limit our discussion to geometries with AP bound to two Si atoms, to adatom and restatom, or to two adatoms.<sup>30</sup> The former can be also excluded because in the case of the *B* object we did not observe any restatom interaction, disappearance of the restatom and highlighting of the neighboring adatoms, in filled-state STM images.<sup>31</sup> Therefore, the only feasible geometries would comprise the AP molecule

bound to two adatoms. The neighboring adatoms in the same HUC do not seem to be affected according to STM images, but the opposite is true in the case of the adjacent adatoms in the neighboring HUCs.

Our DFT simulations provided two object *B* candidate geometries with high bonding energies and the required PDOS. The first one is a 1,6-adduct bound to the adatoms via oxygen and para carbon of the benzene ring, shown in the Figure 5a. Undergoing 1,6-addition leads to the loss of benzene aromaticity and the creation of methylenecyclohexadiene-like structure. The second geometry, shown in the Figure 5d, originates from the first one via dissociation of oxygen that forms a stable adatom–O-backbone atom binding. Simultaneously the rest of the molecule is rebound to the same adatom. We call this model a 1,6-adduct with adatom oxidation. The tendency of the  $7 \times 7$  to dissociate a stable molecule and undergo adatom oxidation was already reported (for water molecule)<sup>32</sup> but only on samples annealed to  $\sim 300$  °C. Thus, we expect a high barrier for the oxygen dissociation and we suppose that the *B* object is the simple 1,6-adduct, even though the second model is more stable by  $\sim 2$  eV.

Next we discuss possible origins of the object *C*. Because of its similarity with the object *B* in the STM images and its stability after annealing, we expect that the object *C* is composed of the molecule or its parts bound to the two adatoms as in the case of the *B* object. However, the *C* object is less frequent, especially on the samples exposed to AP at RT or after annealing to 75 °C. Therefore, we expect a higher formation barrier in comparison with the object *B*. There are many possible two-adatoms-bound products of potential dissociations, hydrogen migrations or more complicated surface incorporations. Analyzing all of them is beyond the possibilities and the scope of this study. We have tested several selected geometries using DFT calculations (Figure S1 in the Supporting Information), however, none of them showed PDOS consistent with the STS curve measured above the object *C*.

Addition reaction of small organic molecules to two adatoms of the  $7 \times 7$  surface, which we propose for the 1,6-adduct (object *B*), is rare. A molecule of comparable size as acetophenone and featuring double bonds, styrene, chemisorbs preferentially via addition to adatom and restatom.<sup>34</sup> Of similar size but strongly polar p-benzoquinone is the only small molecule reported to undergo addition to two adatoms.<sup>11</sup> In this case, the bonding to two adatoms is predictable because the molecule has two highly reactive and negatively charged oxygen atoms. These atoms are supposed to be attracted by the positively charged Si adatoms.<sup>15</sup> Moreover, such addition to two adatoms results in aromaticity of the benzene ring in the case of the p-benzoquinone, therefore it is also energetically favorable.

The comparison of nonpolar styrene and polar p-benzoquinone shows how strongly polarity of the molecule influences mechanisms of adsorption on the  $7 \times 7$ . A detailed description of a chemisorption pathway leading to the bonding to two adatoms is beyond the possibilities of the used methodology. However, it is natural to expect that the adsorption mechanism of AP is affected by its polarity as well. It is probable that the reaction proceeds stepwise. First, the oxygen atom forms a dative bond selectively with an electron-deficient adatom.<sup>11,15</sup> Second, the molecule is further stabilized by forming an Si–C bond. From all available Si and C combinations, the energetically favored 1,6-adduct to two

adatoms in neighboring HUCs (object *B*) is found preferable, especially when the relaxation is allowed at elevated temperatures.

## ■ SUMMARY

In this work, we have used bias-dependent STM imaging and STS to distinguish different objects formed by the adsorbed acetophenone molecule on the Si(111)-7 × 7 surface. The DFT calculations were carried out in order to find atomic geometries that would be in compliance with the experimental observations. At room temperature and after annealing to 75 °C, various configurations of the adsorbed acetophenone can be found on the surface. The most prominent and repeatedly observed metastable structure (referred to as object *A*) is consistent with the silyl enoether bonding after dissociation of one H atom. After annealing to 150 °C, only two of the most stable configurations remain. The first one (object *B*) was identified by means of DFT calculations as a 1,6-adduct to the two adjacent adatoms of neighboring half unit cells. The second less numerous stable structure (object *C*), which appears dark in the empty-state STM images, is proposed to be bound to the two adjacent adatoms as well. We suggest that polarity of the carbonyl group affects the initial stage of chemisorption and thus indirectly favors bonding to the two adatoms over other bonding configurations.

## ■ ASSOCIATED CONTENT

### § Supporting Information

The Supporting Information is available free of charge on the ACS Publications website at DOI: [10.1021/acs.jpcc.6b00486](https://doi.org/10.1021/acs.jpcc.6b00486).

Details of the theoretical calculations, schematic formulas of all calculated structures, statistics on the experimentally observed objects, STM images of larger area after RT exposition to AP, STM images of larger area after annealing to 150 °C. ([PDF](#))

## ■ AUTHOR INFORMATION

### Corresponding Author

\*E-mail: [pavel.kocan@mff.cuni.cz](mailto:pavel.kocan@mff.cuni.cz).

### Notes

The authors declare no competing financial interest.

## ■ ACKNOWLEDGMENTS

Authors would like to thank Dr. Aleš Machara for helping with chemical notation. We acknowledge financial support from GAUK under the Grant 667012. Access to computing and storage facilities owned by parties and projects contributing to the National Grid Infrastructure MetaCentrum, provided under the programme “Projects of Large Infrastructure for Research, Development, and Innovations” (LM2010005), is greatly appreciated.

## ■ REFERENCES

- (1) Bu, Y.; Breslin, J.; Lin, M. C. Adsorption and Thermal Decomposition of Acetaldehyde on Si(111)-7 × 7. *J. Phys. Chem. B* **1997**, *101*, 1872–1877.
- (2) Carbone, M.; Comtet, G.; Dujardin, G.; Hellner, L.; Mayne, A. J. Different Role of Filled and Empty Surface States in a Polyfunctional Molecule Adsorption: Geranyl Acetone on Si(111)-7 × 7. *J. Chem. Phys.* **2002**, *117*, 5012–5017.
- (3) Tao, F.; Wang, Z. H.; Lai, Y. H.; Xu, G. Q. Attachment of Styrene and Phenylacetylene on Si(111)-7 × 7: The Influence of Substitution Groups on the Reaction Mechanism and Formation of π-Conjugated Skeletons. *J. Am. Chem. Soc.* **2003**, *125*, 6687–6696.
- (4) Weiland, C. R.; Yang, L.; Doren, D. J.; Menning, C. A.; Skliar, D.; Willis, B. G.; Chen, J. G.; Opila, R. L. Binding of Styrene on Silicon (111)-7 × 7 Surfaces as a Model Molecular Electronics System. *J. Vac. Sci. Technol., A* **2012**, *30*, 031401.
- (5) Schofield, S. R.; Saraireh, S. A.; Smith, P. V.; Radny, M. W.; King, B. V. Organic Bonding to Silicon via a Carbonyl Group: New Insights from Atomic-Scale Images. *J. Am. Chem. Soc.* **2007**, *129*, 11402–11407.
- (6) Tang, H. H.; Cai, Y. H.; Ning, Y. S.; Lai, Y. H.; Xu, G. Q. A Selective [4 + 2]-like Cycloaddition of α, β-Unsaturated Ketone on Si(111)-7 × 7. *Surf. Sci.* **2007**, *601*, 3293–3302.
- (7) Schofield, S. R.; Warschkow, O.; Belcher, D. R.; Rahnejat, K. A.; Radny, M. W.; Smith, P. V. Phenyl Attachment to Si (001) via STM Manipulation of Acetophenone. *J. Phys. Chem. C* **2013**, *117*, 5736–5741.
- (8) Mehdiour, H. Single-Hydrogen Dissociation Paths for Upright and Flat Acetophenone Adsorbates on the Si(001) Surface. *J. Phys. Chem. C* **2014**, *118*, 23682–23689.
- (9) O'Donnell, K. M.; Warschkow, O.; Suleiman, A.; Fahy, A.; Thomsen, L.; Schofield, S. R. Manipulating the Orientation of an Organic Adsorbate on Silicon: a NEXAFS Study of Acetophenone on Si (001). *J. Phys.: Condens. Matter* **2015**, *27*, 054002.
- (10) Ning, Y. S. Adsorption of Some Carbonyl and Related Compounds on Si(111)-7 × 7 Surface. Ph.D. Thesis, National University of Singapore, 2008.
- (11) Ning, Y. S.; Shao, Y. X.; Xu, G. Q. p-Benzoquinone on Si(111)-7 × 7: [6 + 2]-like Cycloaddition. *J. Phys. Chem. C* **2010**, *114*, 10455–10462.
- (12) Takayanagi, K.; Tanishiro, Y.; Takahashi, M.; Takahashi, S. Structural Analysis of Si(111)-7 × 7 by UHV-Transmission Electron Diffraction and Microscopy. *J. Vac. Sci. Technol., A* **1985**, *3*, 1502–1506.
- (13) Vanderbilt, D. Model for the Energetics of Si and Ge (111) Surfaces. *Phys. Rev. B: Condens. Matter Mater. Phys.* **1987**, *36*, 6209–6212.
- (14) Tao, F.; Xu, G. Q. Attachment Chemistry of Organic Molecules on Si(111)-7 × 7. *Acc. Chem. Res.* **2004**, *37*, 882–893.
- (15) Northrup, J. E. Origin of Surface States on Si(111)-(7 × 7). *Phys. Rev. Lett.* **1986**, *57*, 154–157.
- (16) Lo, R.-L.; Hwang, I.-S.; Ho, M.-S.; Tsong, T. T. Diffusion of Single Hydrogen Atoms on Si (111)-(7 × 7) Surfaces. *Phys. Rev. Lett.* **1998**, *80*, 5584.
- (17) Nečas, D.; Klapetek, P. Gwyddion: an Open-Source Software for SPM Data Analysis. *Cent. Eur. J. Phys.* **2012**, *10*, 181–188.
- (18) Lewis, J. P.; Jelínek, P.; Ortega, J.; Demkov, A. A.; Trabada, D. G.; Haycock, B.; Wang, H.; Adams, G.; Tomfohr, J. K.; Abad, E.; et al. Advances and Applications in the FIREBALL Ab Initio Tight-Binding Molecular-Dynamics Formalism. *Phys. Status Solidi B* **2011**, *248*, 1989–2007.
- (19) Mulliken, R. S. Electronic Structures of Polyatomic Molecules and Valence VI. On the Method of Molecular Orbitals. *J. Chem. Phys.* **1935**, *3*, 375–378.
- (20) Hamann, D. R.; Schlüter, M.; Chiang, C. Norm-Conserving Pseudopotentials. *Phys. Rev. Lett.* **1979**, *43*, 1494–1497.
- (21) Jelínek, P.; Wang, H.; Lewis, J. P.; Sankey, O. F.; Ortega, J. Multicenter Approach to the Exchange-Correlation Interactions in *Ab Initio* Tight-Binding Methods. *Phys. Rev. B: Condens. Matter Mater. Phys.* **2005**, *71*, 235101.
- (22) Kohn, W.; Sham, L. J. Self-Consistent Equations Including Exchange and Correlation Effects. *Phys. Rev.* **1965**, *140*, A1133–A1138.
- (23) Perdew, J. P.; Zunger, A. Self-Interaction Correction to Density-Functional Approximations for Many-Electron Systems. *Phys. Rev. B: Condens. Matter Mater. Phys.* **1981**, *23*, 5048–5079.
- (24) Ceperley, D. M.; Alder, B. J. Ground State of the Electron Gas by a Stochastic Method. *Phys. Rev. Lett.* **1980**, *45*, 566–569.

- (25) Monkhorst, H. J.; Pack, J. D. Special Points for Brillouin-Zone Integrations. *Phys. Rev. B: Condens. Matter Mater. Phys.* **1976**, *13*, 5188–5192.
- (26) Kresse, G.; Furthmüller, J. Efficient Iterative Schemes for Ab Initio Total-Energy Calculations Using a Plane-Wave Basis Set. *Phys. Rev. B: Condens. Matter Mater. Phys.* **1996**, *54*, 11169.
- (27) Perdew, J. P.; Chevary, J. A.; Vosko, S. H.; Jackson, K. A.; Pederson, M. R.; Singh, D. J.; Fiolhais, C. Atoms, Molecules, Solids, and Surfaces: Applications of the Generalized Gradient Approximation for Exchange and Correlation. *Phys. Rev. B: Condens. Matter Mater. Phys.* **1992**, *46*, 6671–6687.
- (28) Boys, S.; Bernardi, F. The Calculation of Small Molecular Interactions by the Differences of Separate Total Energies. Some Procedures with Reduced Errors. *Mol. Phys.* **1970**, *19*, 553–566.
- (29) Tersoff, J.; Hamann, D. R. Theory of the Scanning Tunneling Microscope. *Phys. Rev. B: Condens. Matter Mater. Phys.* **1985**, *31*, 805–813.
- (30) In discussion, we excluded bonding with other atoms of the 1st layer, which is not likely for following reasons. Bonding to Si dimer-row atoms was not reported for any molecule, because the dimer atoms are already four-coordinated. Another possibility is bonding to the adatom–backbone atom pair. However this would need an extra energy to overcome a barrier for the backbone atom–adatom bond scission. According to our DFT calculations (shown in the [Supporting Information](#)), such geometries are indeed energetically unfavorable.
- (31) Horn, S. A.; Patitsas, S. N. STM Study of Charge Transfer and the Role of Rest-Atoms in the Binding of Benzene to Si(111)7 × 7. *Surf. Sci.* **2008**, *602*, 630–637.
- (32) Lo, R.-L.; Chang, C.-M.; Hwang, I.-S.; Tsong, T. T. Observation of Single Oxygen Atoms Decomposed from Water Molecules on a Si(111)-7 × 7 Surface. *Phys. Rev. B: Condens. Matter Mater. Phys.* **2006**, *73*, 075427.

# **Supporting Information**

## **Chemisorption of Acetophenone on Si(111)-7×7**

### **– Polar Aromatic Molecule on Electronically Complex Surface**

O. Krejčí, P. Matvija, P. Zimmermann, P. Sobotík, Ivan Ošt'ádal, and P. Kocán\*

E-mail: pavel.kocan@mff.cuni.cz

## **Contents**

<b>Details of theoretical calculations</b>	<b>S2</b>
Fireball calculations . . . . .	S2
VASP calculations . . . . .	S3
Densities of states . . . . .	S3
<b>All calculated configurations</b>	<b>S3</b>
<b>Additional experimental results</b>	<b>S5</b>
<b>References</b>	<b>S7</b>

---

\*To whom correspondence should be addressed

## Details of theoretical calculations

### Fireball calculations

The basis set for the valence electrons consists of numerical *Fireball* pseudo-atomic orbitals with radial cuts.<sup>1</sup> The used radial cuts are shown in the table S1.

Table S1: The used radial cuts for the basis set used in the Fireball calculations.  $a_b$  stands for the Bohr radius.

atom	orbital	radial cut [ $a_b$ ]
H	$s$	4.0
	$s^*$	4.0
C	$s$	4.5
	$p$	4.5
	$d$	5.4
O	$s$	3.5
	$p$	4.0
	$d$	5.0
Si	$s$	4.8
	$p$	5.4
	$d$	5.2

In order to confirm that the sufficient amount of layers was used, we performed calculations with a total of eight layers of Si in the slab, for the most favorable geometries. These calculations provided the same results as the one done with the six layered slab.

The adsorption energy  $E_{ad}$  (as shown in Figure S1) for any calculated structure is defined as:  $E_{ad} = -(E_{TOT}^{structure} - E_{TOT}^{7 \times 7} - E_{TOT}^{AP})$ , where  $E_{TOT}^{structure}$  is the total energy of the calculated adsorption geometry of the acetophenone (AP) molecule,  $E_{TOT}^{7 \times 7}$  is the total energy of the clean  $7 \times 7$  slab and  $E_{TOT}^{AP}$  stands for the total energy of the AP molecule in vacuum. For the most stable geometries, we performed calculations with the AP molecule adsorbed at different types (there are two inequivalent HUC types, faulted and unfaulted with respect to the bulk<sup>2,3</sup>) or different positions within a HUC – close to a corner or a center adatom. The differences in the adsorption energies were lower than 0.1 eV.

## VASP calculations

The VASP code<sup>4</sup> is based on a plane waves basis set. In our calculations we used an energy cut-off for the plane waves 396 eV and ultrasoft pseudopotentials.<sup>5</sup>

## Densities of states

The atomic projected densities of states were obtained by projecting the density of states of the whole system onto each atom of the system. The molecule projected densities of states (PDOS) were gained via summing atomic densities corresponding to all atoms of the molecule.

## All calculated configurations

Here we show all the configurations of the adsorbed AP molecule (Figure S1), which were optimized and calculated in order to find potential candidates for the observed *A*, *B* and *C* objects. The silyl enolethers and the adducts bound to the adatom and the restatom were calculated as candidates to the object *A*. Dissociated adatom-adatom configurations and adducts to two adatoms with hydrogen migrations were our attempts to find a candidate for the object *C*. The dissociated structure with adatom oxidation and some of the structures concerning adducts with hydrogen migration are energetically even more stable than the simple 1,6-adduct; however, any of these structures do not have PDOS in agreement with the measured STS data. The backbone-bound and dimer-bound structures were calculated just in order to exclude the possibility of these bindings from thermodynamical point of view – such structures are less stable than the 1,6-adduct.

Some of the 1,4-adducts have higher or comparable adsorption energy with respect to the simple 1,6-adduct; however, we expect that the BSSE error<sup>6</sup> affects the total energy calculations. Even though we cannot evaluate the exact value of the BSSE error within our calculations, the error is supposed to be enhanced when the atoms of the molecule are close to the neighboring Si surface atoms, as in this case.

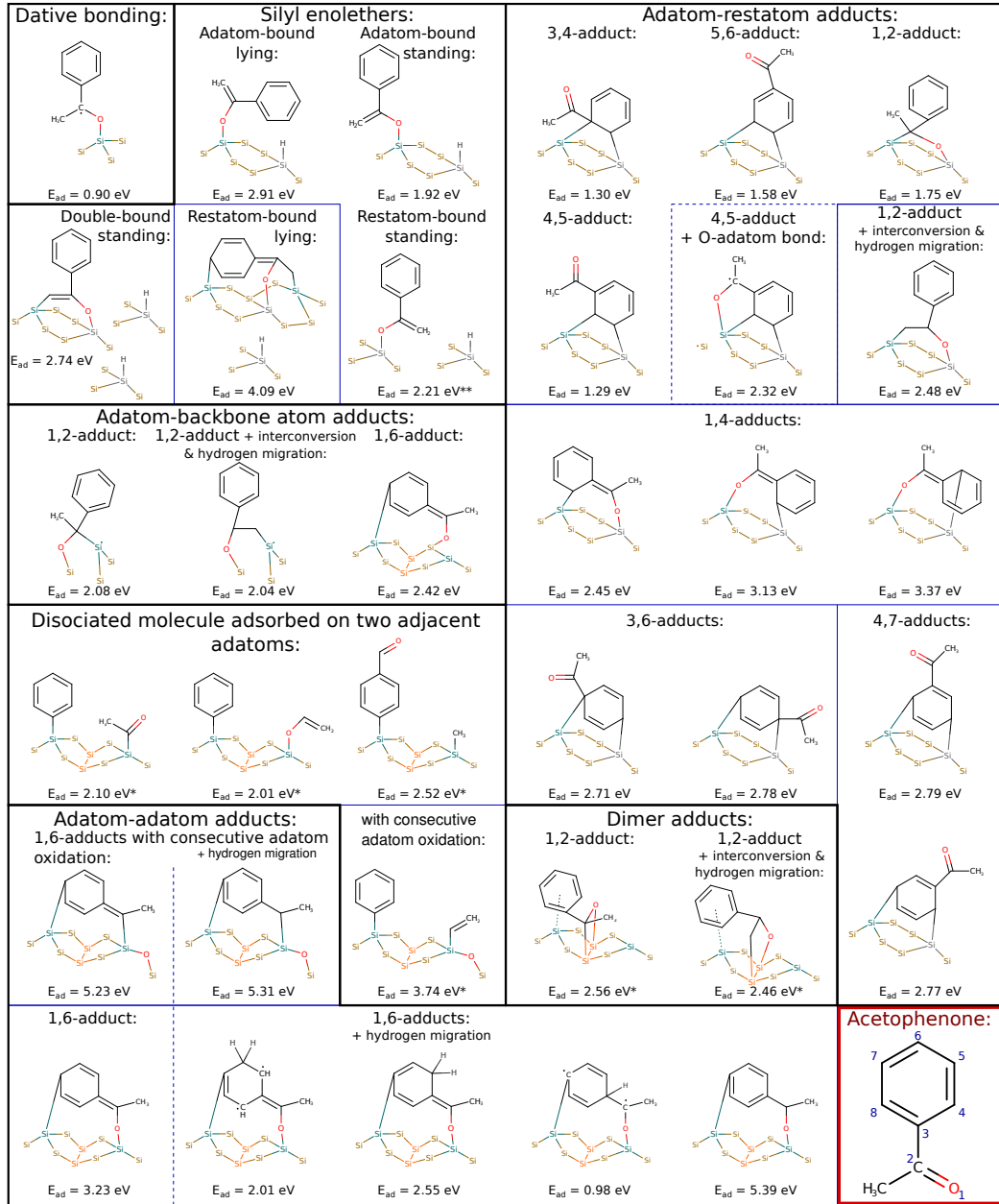


Figure S1: Formulas for all the adsorption geometries, that were studied and optimized by means of the DFT calculations. The adatoms are depicted in blue, restatoms in gray and dimer atoms are depicted in orange. The  $E_{AD}$  – adsorption energies are taken from Fireball and they correspond to the acetophenone adsorbed at the faulted corner adatom, unless specified otherwise by stars: \*-bound to or nearby center adatoms; \*\* - bound only to the restatoms. The adsorption energies may differ, depending on the HUC or side (corner or edge) in the HUC, by less than 0.1 eV. The acetophenone molecule with numbering of atoms is shown in the right bottom corner.

## Additional experimental results

In this section, we show statistical analysis of the objects resolved on STM images, together with STM images of larger areas, in order to supply the figures and statements in the main text.

The statistical data obtained from all the three post-deposition annealing treatments are shown in Table S2. The data of the resolved objects after room temperature deposition and after annealing the sample to 75 °C were taken from single set of STM images. In the first case the data were collected from the surface area of approximately 30 × 30 nm, while in the second one the surface area was ∼ 20 × 20 nm; however, the coverage was much larger due to higher exposition to AP. These data therefore provide only rough estimates. The statistical data of the stable objects after annealing the sample to 150 °C, which were the main subjects of this study, were gathered from multiple sets of measurements containing much larger area of the sample.

Figure S2 shows STM images obtained after room temperature deposition of the acetophenone molecules. Figure S3 reveals large area STM images after annealing the sample to 150 °C. Only a floating average filter was used to process the STM data.<sup>7</sup>

Table S2: The statistics on the resolved objects from the experimental STM images. Irr. objects, No. obj. and RT stands for irregular objects, total number of statistically analyzed objects and room temperature, respectively.

Temperature	Irr. objects [%]	Objects A [%]	Objects B [%]	Objects C [%]	No. obj.
RT	44.0	4.0	36.0	16.0	25
75 °C	55.8	9.6	30.8	3.8	52
150 °C	—	—	68.9	31.1	201

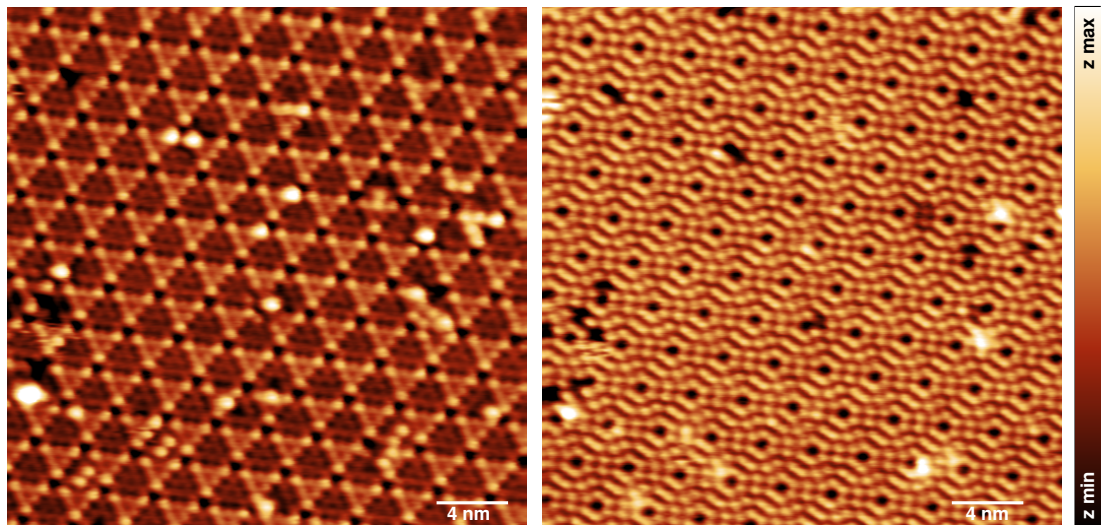


Figure S2: The Si(111)-(7 × 7) surface after room temperature exposition to the acetophenone molecules. Left and right parts show the same area with opposite sample biases, left:  $U_s = -1.6$  V, right:  $U_s = 1.6$  V (tunneling current 0.28 nA).

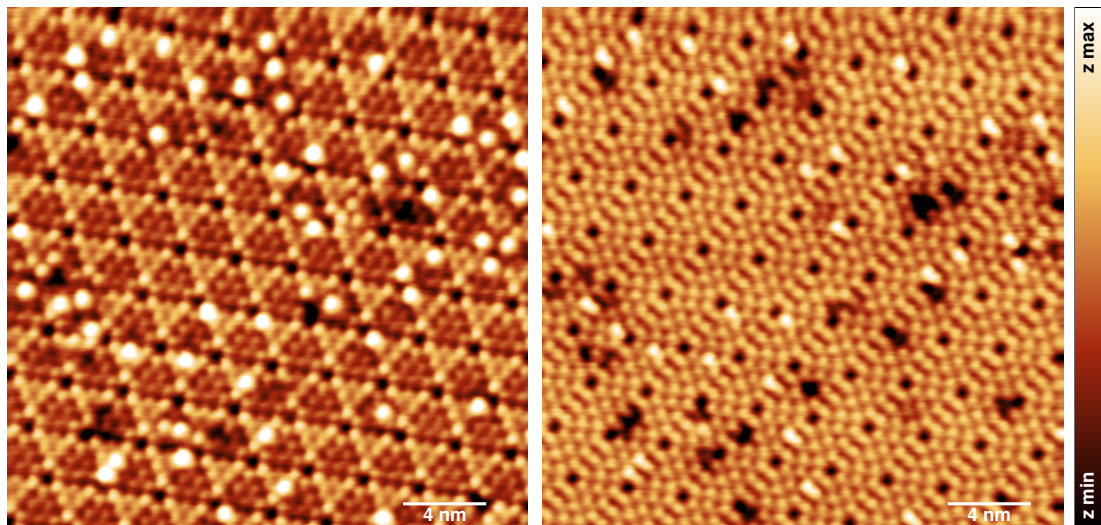


Figure S3: The AP/Si(111)-(7 × 7) surface after annealing to 150 °C. Left and right parts show the same area with opposite sample biases, left:  $U_s = -1.75$  V, right:  $U_s = 1.75$  V (tunneling current 0.12 nA).

## References

- (1) Lewis, J. P.; Jelínek, P.; Ortega, J.; Demkov, A. A.; Trabada, D. G.; Haycock, B.; Wang, H.; Adams, G.; Tomfohr, J. K.; Abad, E. et al. Advances and Applications in the FIREBALL Ab Initio Tight-Binding Molecular-Dynamics Formalism. *Phys. Status Solidi B* **2011**, *248*, 1989–2007.
- (2) Takayanagi, K.; Tanishiro, Y.; Takahashi, M.; Takahashi, S. Structural Analysis of Si(111) $7\times7$  by UHV-Transmission Electron Diffraction and Microscopy. *J. Vac. Sci. Technol. A* **1985**, *3*, 1502–1506.
- (3) Vanderbilt, D. Model for the Energetics of Si and Ge (111) Surfaces. *Phys. Rev. B* **1987**, *36*, 6209–6212.
- (4) Kresse, G.; Furthmüller, J. Efficient Iterative Schemes for Ab Initio Total-Energy Calculations Using a Plane-Wave Basis Set. *Phys. Rev. B* **1996**, *54*, 11169.
- (5) Vanderbilt, D. Soft Self-Consistent Pseudopotentials in a Generalized Eigenvalue Formalism. *Phys. Rev. B* **1990**, *41*, 7892.
- (6) Boys, S.; Bernardi, F. The Calculation of Small Molecular Interactions by the Differences of Separate Total Energies. Some Procedures with Reduced Errors. *Mol. Phys.* **1970**, *19*, 553–566.
- (7) Nečas, D.; Klapetek, P. Gwyddion: an Open-Source Software for SPM Data Analysis. *Cent. Eur. J. Phys.* **2012**, *10*, 181–188.

# 4. Thallium passivation of the Si(111) surface

## 4.1 Surface passivation

In the process of passivation, a surface is covered by a suitable medium that saturates all or a part of dangling bonds. The process is often used to decrease the reactivity of highly reactive, e.g. silicon, surfaces. Besides the reactivity, passivation has a substantial effect on the roughness of the adsorption energy relief (see Fig. 4.1). On reactive surfaces, the relief is highly corrugated due to the presence of dangling bonds. Diffusion of deposited molecules is either halted by chemisorption to the dangling bonds (see the previous chapter) or confined to small areas [74]. Reducing the number of dangling bonds flattens the adsorption energy relief and lowers the energy barriers for diffusion.

The most common passivation method of silicon surfaces is the passivation by hydrogen. In the case of the Si(111) surface, individual hydrogen atoms saturate all surface dangling bonds and stabilize the  $(1 \times 1)$  termination of the surface. As a result, diffusion barriers for adsorbed atoms are significantly lowered (e.g. in the case of Ag, from 0.85 eV to 0.12 eV, see Fig. 4.1)

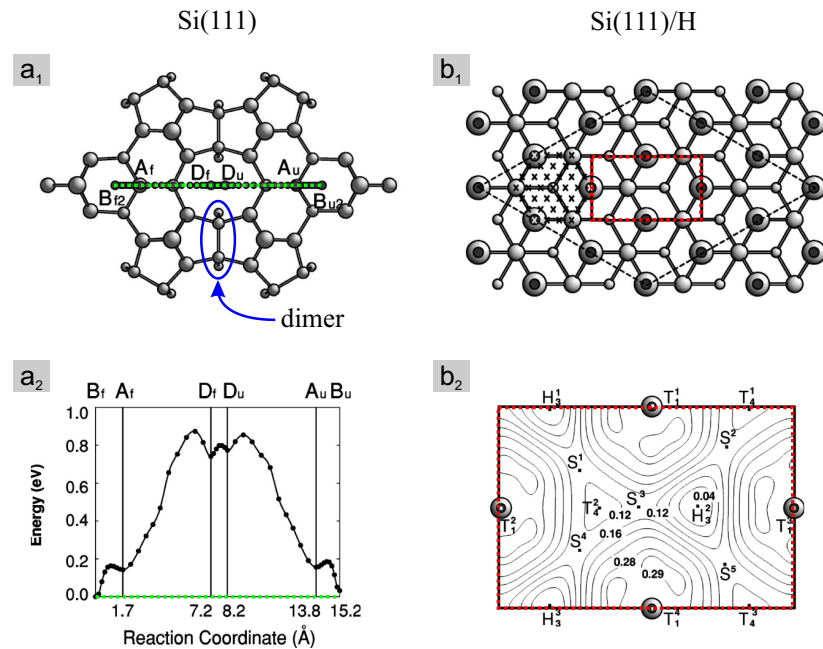


Fig. 4.1: Ag diffusion on the clean and H-terminated Si(111) surface. **a:** Diffusion barrier of the reaction coordinate over a dimer row on the  $(7 \times 7)$  surface. **b:** Adsorption energy relief of the H-terminated Si(111) surface. Reprinted from [75].

## 4.2 The Si(111)/Tl-(1 × 1) surface

In 1980's and 1990's, the group III elements on Si surfaces have been extensively studied as model systems for the adsorbate-induced surface and interface phenomena [55–60]. In 1999, Vitali et al. continued with the effort by the study of thallium overayers on the Si(111) surface [16]. At that time, Tl was studied because of its inert-pair property of the  $6s^2$  electrons, that is the reluctance of the electrons to participate in chemical bonding. The reluctance makes Tl chemically similar to alkali metals. The first experiments showed that at the room-temperature Tl atoms form small clusters in the  $(7 \times 7)$  HUC, first occupying faulted, then unfaulted cells. At the temperature above 260 °C and coverage 1 ML, the  $(1 \times 1)$  reconstruction emerges on the surface. Between 1 ML and 2 ML coverage, an incommensurate  $(6 \times 6)$  structure forms on top of the first layer. In 2002, Lee et al. determined that Tl atoms occupy  $T_4$  sites over the Si lattice and, contrary to previous observations, discovered that Tl can form a  $(\sqrt{3} \times \sqrt{3})$  reconstruction, similarly to other group III elements [19, 76]. The observation of both  $(1 \times 1)$  and  $(\sqrt{3} \times \sqrt{3})$  structures led to the question of Tl valency in the reconstructions. The question was answered in 2006 by photoemission experiments of Sakamoto et al. [77, 78] which showed that the nature of Tl binding is same in  $(1 \times 1)$  and  $(\sqrt{3} \times \sqrt{3})$  reconstructions, i.e. the valence state of Tl on the surface is 1+.

From the electronic side, Lee et al. showed that Tl binding to the Si surface has the mainly ionic character given by the charge transfer from Tl atoms to Si dangling bonds [19]. Theoretical calculations suggested that the transfer makes the Tl –  $(1 \times 1)$  surface semiconducting with a band gap of 0.34 eV. Later STM experiments of Kocán et al. (2011) showed that unlike the ideal surface, the real surface contains point defects with electronic states close to Fermi level [79]. These states make the surface metallic-like. On top of that, angle-resolved and spin-resolved photoemission studies of Sakamoto et al. revealed that the Si(111)/Tl –  $(1 \times 1)$  surface possesses peculiar electronic properties: (i) giant spin split of surface states close to the Fermi level and (ii) abrupt rotation of the Rashba spin to the direction perpendicular to the surface [17, 18, 80]. Both these properties are of a potential use in the future spintronic devices.

The Si(111)/Tl –  $(1 \times 1)$  surface is usually prepared by deposition of 1 ML of Tl on the Si(111) –  $(7 \times 7)$  surface and annealing at  $\approx 300$  °C [19]. The annealing cancels the  $(7 \times 7)$  DAS structure and rearranges Si atoms into the  $(1 \times 1)$  termination. The rearrangement also changes surface concentration of the atoms in the topmost Si bi-layer, from 2.08 ML in the case of the  $(7 \times 7)$  termination to 2 ML in the case of the  $(1 \times 1)$  termination. In the paper IV (page 45), we show that the extra 0.08 ML of Si atoms form Si bi-layer islands that are covered by the Tl –  $(1 \times 1)$  layer. Edges of the islands behave same as the step edges of the terraces. Density of the islands can be affected by the length and the exact temperature of annealing during the preparation of the Tl –  $(1 \times 1)$  surface.

## 4.3 Desorption-induced thallium structures

Length and the exact temperature of annealing are two sensitive parameters mostly affecting preparation of the  $(1 \times 1)$  reconstruction. The sensitivity is caused by a very low desorption temperature of Tl from the Si(111) surface ( $\approx 330$  °C), which is only

$\approx 30^\circ\text{C}$  above the temperature necessary for the preparation of the  $(1 \times 1)$  layer. Slightly higher temperature or slightly longer annealing cause desorption of a part of Tl atoms and formation of the incomplete  $(1 \times 1)$  layer.

At the temperature above  $\approx 300^\circ\text{C}$ , Si dangling bonds are gradually exposed as Tl atoms desorb from the surface. Exposed dangling bonds immediately react, first with remaining Tl atoms, then with Si atoms. In this process, the surface reconstruction changes from the original Tl –  $(1 \times 1)$  through the TlSi- $(\sqrt{3} \times \sqrt{3})$  mosaic reconstruction to a wide variety of metastable Si reconstructions (see Fig. 4.2 and Fig. 2 of the paper IV). We successfully fitted the temperature dependence of the amount of residual Tl atoms on the surface by a model using the first order desorption. The same desorption energy of  $(2.1 \pm 0.3)\text{ eV}$  and frequency prefactor  $5 \times 10^{14 \pm 2}\text{s}^{-1}$  during all stages of the desorption are sufficient for the fitting. This led us to the conclusion that bonding of Tl in both  $(1 \times 1)$  and  $(\sqrt{3} \times \sqrt{3})$  configurations is of the same nature. The conclusion agrees well with the previous photoemission studies of Sakamoto et al. [77, 78].

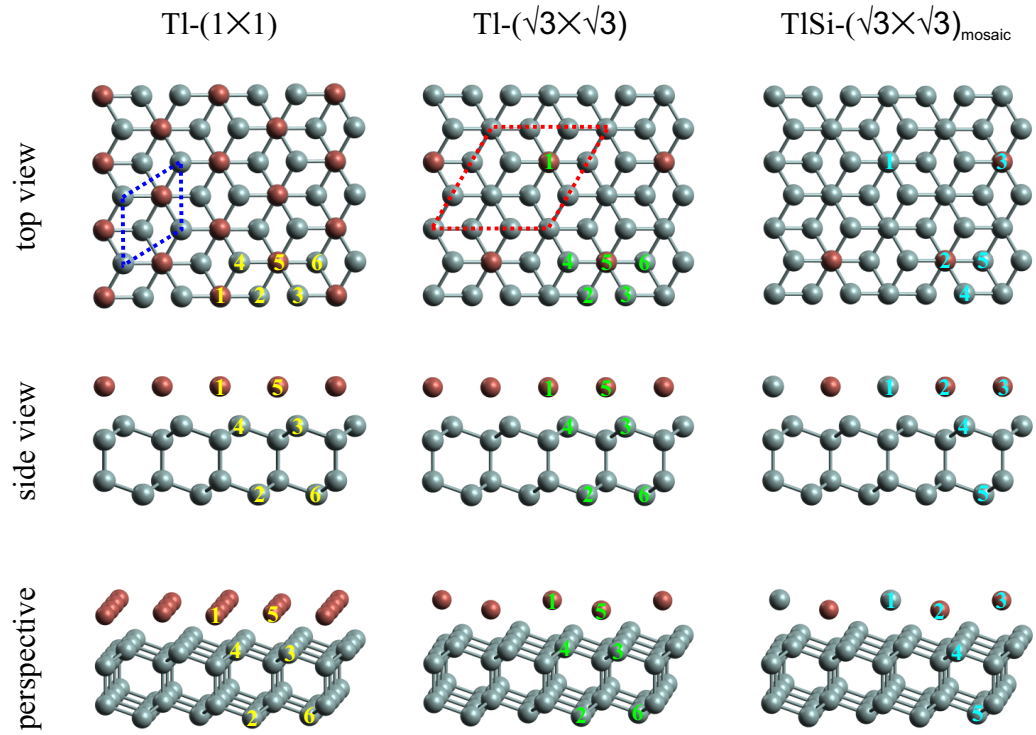


Fig. 4.2: Structural models of the Tl –  $(1 \times 1)$  , Tl –  $(\sqrt{3} \times \sqrt{3})$  and TlSi mosaic reconstructions. Blue and red dotted lines mark unit cells of the reconstructions.

My contribution to the paper IV consists in the participation in the STM measurements of the desorption-induced structures (Fig. 2 in the paper IV). I analyzed the obtained data and determined the coverage of the surface by Tl atoms. Results of the analysis were used to determine the dependence of the Tl coverage on the annealing temperature (Fig. 3 in the paper IV).



## An STM study of desorption-induced thallium structures on the Si(111) surface

Pavel Kocán\*, Pavel Sobotík, Peter Matvija, Martin Setvík, Ivan Ošt'ádal

*Charles University in Prague, Faculty of Mathematics and Physics, Department of Surface and Plasma Science, V Holešovičkách 2, 180 00 Praha 8, Czech Republic*

### ARTICLE INFO

#### Article history:

Received 11 October 2011

Accepted 26 December 2011

Available online 1 March 2012

#### Keywords:

Scanning tunneling microscopy  
Si(111)  
Thallium  
Desorption

### ABSTRACT

The scanning tunneling microscopy is used to study morphology of a Tl adlayer in various stages of Tl desorption from the Si(111) surface. Transition from the Si(111)/(1×1)-Tl structure through the  $(\sqrt{3} \times \sqrt{3})R30^\circ$  mosaic phase to domains of metastable Si reconstructions is observed. Silicon substitutional atoms are found to be intrinsic to the  $(\sqrt{3} \times \sqrt{3})R30^\circ$  structure. The temperature dependence of the amount of residual Tl atoms on the surface is successfully fitted by a model using the first order desorption. The same desorption energy of  $(2.1 \pm 0.3)$  eV and frequency prefactor  $5 \times 10^{14 \pm 2} \text{ s}^{-1}$  during all stages of the desorption are sufficient for the fitting. It is concluded that bonding of Tl in both  $(1 \times 1)$  and  $(\sqrt{3} \times \sqrt{3})$  configurations is of the same nature.

© 2012 Elsevier B.V. All rights reserved.

### 1. Introduction

Recently, the Si(111) surface with one deposited monolayer of thallium has attracted a significant attention due to the observation of an unusual Rashba spin splitting [1]. The spin splitting, lifted by a spin-orbit interaction in combination with a broken symmetry [2], represents a promising mechanism for generation of spin-polarized electrons for spintronic applications [3].

Deposition of Tl on the Si(111) surface and annealing to 250–300 °C results in formation of the Si(111)/(1×1)-Tl reconstruction [4]. Upon annealing to a higher temperature (~350 °C) a Si(111)/ $(\sqrt{3} \times \sqrt{3})R30^\circ$ -Tl reconstruction [hereafter called  $(\sqrt{3} \times \sqrt{3})$  for simplicity] is formed via desorption of Tl [4,5]. Structure of the  $(1 \times 1)$  reconstruction was determined as a monolayer of Tl atoms in T<sub>4</sub> site positions (see Fig. 1a) using low energy electron diffraction [6], synchrotron X-ray scattering [7], and ab-initio calculations [4]. On the other hand, structure of the  $(\sqrt{3} \times \sqrt{3})$  reconstruction is not settled yet. Ab-initio calculations [8] denoted 1/3 of monolayer of Tl atoms at T<sub>4</sub> sites (Fig. 1b) as the stable structure. Such structure is similar to the  $(\sqrt{3} \times \sqrt{3})$  reconstruction formed by other group III metals with trivalent metal atoms. However, photo-emission results show a different bonding nature [9] and a monovalent state [10] of the Tl atoms in the  $(\sqrt{3} \times \sqrt{3})$  structure. By means of the scanning tunneling microscopy (STM), only a mosaic  $(\sqrt{3} \times \sqrt{3})$  structure with some Tl adatoms replaced by Si adatoms (Fig. 1c) was observed [5].

We use STM to study the desorption-mediated transitions  $(1 \times 1) \rightarrow (\sqrt{3} \times \sqrt{3}) \rightarrow$  Si metastable structures. Morphology of Tl ad-layer in different stages of desorption is observed as a function of annealing temperature  $T$ . The atomic resolution allows us to analyze the amount  $\theta$  of residual Tl on the surface. By fitting the dependence  $\theta(T)$  we obtain the desorption energy, which reflects character of bonding of Tl atoms to the substrate.

### 2. Experimental

One ML (monolayer,  $7.83 \times 10^{14} \text{ atoms cm}^{-2}$ ) of thallium (purity 99.99%) was evaporated from a resistively heated Ta tube onto the Si(111)/(7×7) substrate (Sb doped with resistivity of 0.005–0.01 Ω cm) cleaned by flashing to ~1200 °C. Deposited amount was controlled by a quartz thickness monitor and calibrated by STM. The  $(1 \times 1)$ -Tl surface was prepared as the initial point of each experiment by annealing the surface to 280 °C. The samples were annealed by passing DC current for 2 min, absolute (relative) temperature accuracy was  $\pm 30$  °C ( $\pm 10$  °C). The STM measurements were performed by means of a non-commercial STM in an ultra-high vacuum chamber with the base pressure better than  $3 \times 10^{-9}$  Pa. Pressure during Tl deposition was within the  $10^{-8}$  Pa order. Electrochemically etched tungsten tips cleaned in-situ by electron bombardment were used for measurements.

### 3. Results and discussion

Fig. 2a shows an STM image of the surface prepared by annealing of the Si(111) surface with one Tl monolayer at 280 °C for 2 min. The surface is almost uniformly covered by the  $(1 \times 1)$ -Tl layer. On the main flat area, several hexagonally shaped 2D islands are observed. We propose that these islands contain an extra bi-layer of Si atoms

\* Corresponding author. Tel.: +420 2191 2349.  
E-mail address: [pavel.kocan@mff.cuni.cz](mailto:pavel.kocan@mff.cuni.cz) (P. Kocán).

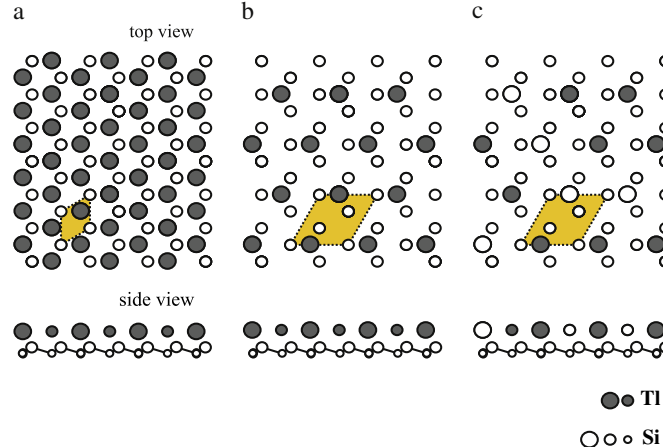


**Fig. 1.** Schematic structural models of the Si(111) surface with (a)  $(1 \times 1)$ -Tl [4], (b)  $(\sqrt{3} \times \sqrt{3})$ -Tl [8] and (c) mosaic  $(\sqrt{3} \times \sqrt{3})$ -Tl [5] reconstructions. Filled and empty circles represent Tl and Si atoms. Unit cells of  $(1 \times 1)$  and  $(\sqrt{3} \times \sqrt{3})$  are outlined by the rhombuses.

covered by the  $(1 \times 1)$  monolayer of Tl. The surface concentration of Si atoms in the  $(7 \times 7)$  reconstruction [prior to  $(1 \times 1)$ -Tl formation] is 0.08 ML higher than that of the bulk-terminated surface. These extra Si atoms would form bilayers with total area of 4%, which well agrees with 5% obtained from our STM data. The surface of these islands (not shown) appears on STM images the same as the surface of the main area, shown in the inset of Fig. 2a. Their apparent height corresponds to one Si bi-layer high step on the Si(111) surface – see the line

profile along the dashed line crossing three bright islands in Fig. 2a. The inset in Fig. 2a shows a detail of the  $(1 \times 1)$ -Tl surface with resolved  $1 \times 1$  periodicity and several regularly shaped defects, interpreted as Tl multi-vacancies [11].

The structures observed after annealing of the  $(1 \times 1)$  surface at different temperatures are shown in Fig. 2b–f. After annealing at 300 °C (Fig. 2b) the  $(1 \times 1)$  ad-layer, appearing as a bright surface without corrugation, became broken by areas with desorbed Tl. In

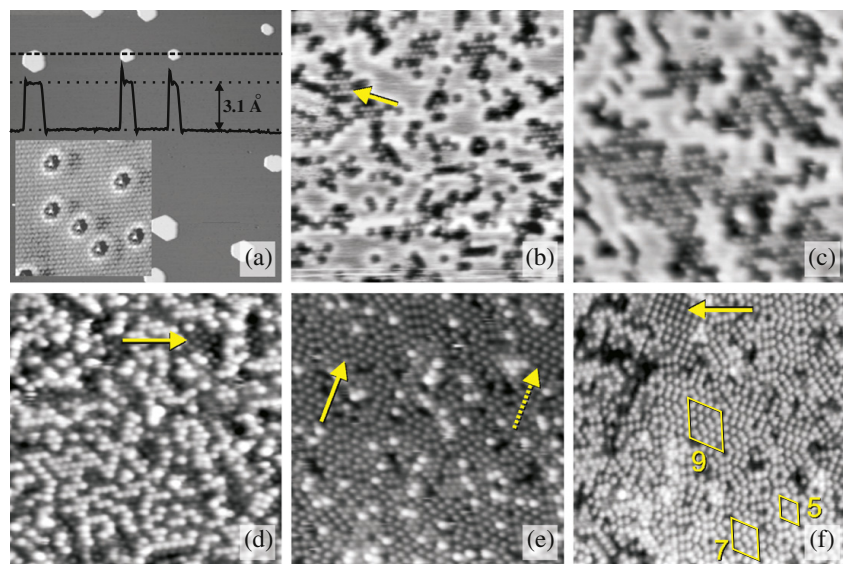


**Fig. 2.** STM images of the Si(111) surface with one monolayer of Tl after annealing at different temperatures. (a)  $T = 280$  °C: surface covered entirely by the  $(1 \times 1)$ -Tl structure. The inset shows detail of the  $(1 \times 1)$  surface. The plot shows a line profile along the dashed line crossing 2D islands. (b)  $T = 300$  °C and (c)  $T = 330$  °C: coexisting  $(1 \times 1)$  and  $(\sqrt{3} \times \sqrt{3})$  structures. (d) Surface covered mostly by  $(\sqrt{3} \times \sqrt{3})$  mosaic after two cycles of annealing at 300 °C and 330 °C. (e)  $T = 360$  °C: the surface, from which Tl almost completely desorbed. (f)  $T = 450$  °C: surface covered mostly by  $(2n+1)(2n+1)$  reconstructions. Dimensions of images: (a)  $200 \times 200$  nm $^2$ , inset  $7 \times 7$  nm $^2$ , (b–f)  $20 \times 20$  nm $^2$ . Sample voltage: (a) –3.0 V, inset: 9 mV, (b) 1.1 V, (c) 0.3 V, (d) 0.5 V, (e) 1.0 V, (f) 1.6 V. Other details are in text.

these areas (see e.g. the area marked by the arrow in Fig. 2b) the  $(\sqrt{3} \times \sqrt{3})$  reconstruction forms up locally. If the annealing temperature is increased to 330 °C, the total area of the  $(\sqrt{3} \times \sqrt{3})$  reconstruction is larger, as shown in Fig. 2c. In both Fig. 2b and c the  $(\sqrt{3} \times \sqrt{3})$  reconstruction is not perfect, some spots in the lattice are darker than the others. The darker spots on empty states STM images were previously interpreted as Si substitutional atoms in the  $(\sqrt{3} \times \sqrt{3})$  domain (see Fig. 1c) [5]. Fig. 2d shows the surface prepared by annealing at 300 °C followed by annealing at 330 °C. The  $(1 \times 1)$  areas are completely replaced by a mosaic of Ti and Si adatoms with the  $(\sqrt{3} \times \sqrt{3})$  periodicity depicted in Fig. 1c. A small fraction of the surface appears darker (see e.g. the area marked by the arrow in Fig. 2d) and a local structure is different in these areas. The darker regions can be assigned to Si metastable local structures [12] with Ti completely desorbed.

The area of the Si metastable structures increases rapidly after annealing at 360 °C, as shown in Fig. 2e. On the surface, only few mostly isolated Ti atoms remain, appearing as bright protrusions. The rest of the surface is covered with a mixture of locally ordered Si adatom structures. Specifically, origins of  $c(2 \times 8)/c(2 \times 4)$  reconstruction can be found (see the dotted arrow in Fig. 2e pointing to a  $c(2 \times 8)$  region) as well as origins of dimer-adatom-stacking fault (DAS) structures  $(2n+1)(2n+1)$  (see the solid arrow in Fig. 2e). After annealing at higher temperatures Ti atoms desorb completely. An example after annealing at 450 °C is shown in Fig. 2f. Compared to Fig. 2e, domains containing several unit cells of DAS reconstructions can be recognized, see selected unit cells of  $(9 \times 9)$ ,  $(7 \times 7)$  and  $(5 \times 5)$  reconstructions outlined by the rhombuses labeled by 9, 7 and 5, respectively. The arrow in Fig. 2f points to an area of the  $c(2 \times 8)$  local structure coexisting with  $(2n+1)(2n+1)$  areas.

An amount of non-desorbed Ti atoms  $\Theta$  (hereafter called coverage) was extracted from STM images using different contrast of Si and Ti atoms. The amount of Ti atoms in the  $(1 \times 1)$  structure was obtained by measuring its area with known concentration of Ti atoms, while the amount of Ti atoms in the  $(\sqrt{3} \times \sqrt{3})$  structure was counted 'atom-by-atom'. In order to estimate the accuracy of measuring the Ti coverage from STM images, test experiments were performed as follows. The surface with 0.7 ML of deposited Ti was

annealed at 280 °C, which is a condition for the  $(1 \times 1)$ -Ti formation with negligible desorption (see the  $(1 \times 1)$  surface with no indication of desorption in Fig. 2a). The Ti coverage measured from STM images was in good agreement with the deposited amount within the range of thickness monitoring error ( $\pm 5\%$ ).

The experimentally obtained dependence of coverage  $\Theta$  on annealing temperature  $T$  is plotted in Fig. 3 by squares. The fitting solid line in Fig. 3 was obtained as follows. First, we assume that the observed structural changes (Fig. 2) are induced by a thermally activated desorption of the first order. Second, we assume that the desorption energy  $E_{des}$  does not depend on  $\Theta$ , i.e.  $E_{des}$  is the same for Ti atoms in all structures formed during the desorption process. Then the decrease of coverage with time  $t$  can be expressed as

$$\Theta = \Theta_0 \exp(-Rt), \quad (1)$$

where  $\Theta_0$  is the initial Ti coverage and  $R$  is the desorption rate, depending on temperature  $T$ :

$$R = \nu \exp(-E_{des}/k_B T), \quad (2)$$

where  $\nu$  is the frequency prefactor and  $k_B$  is the Boltzmann constant. The initial coverage  $\Theta_0$  and time  $t$  were set  $\Theta_0 = 0.97$  ML (the initial Ti coverage is lower than unity due to the presence of intrinsic defects, see Fig. 2a) and  $t = 120$  s (from the experiment). The frequency prefactor  $\nu$  and the desorption energy  $E_{des}$  were found from the linear fit of Arrhenius dependence of  $\ln(R)$  vs.  $1/T$ , shown in Fig. 4. The values of  $R$  were calculated from the experimentally obtained values of  $\Theta$  using Eq. (1). The parameters obtained by the fitting are  $E_{des} = (2.1 \pm 0.3)$  eV and  $\nu = 5 \times 10^{14 \pm 2} \text{ s}^{-1}$ .

The total Ti coverage  $\Theta$  can be divided into two components  $\Theta_1$  and  $\Theta_{\sqrt{3}}$ , corresponding to fractions of atoms in the  $(1 \times 1)$  and the  $(\sqrt{3} \times \sqrt{3})$  structures, respectively. For simplicity we assume that the  $(\sqrt{3} \times \sqrt{3})$  structure is formed only by desorption from the  $(1 \times 1)$ . Then, taking into account desorption from both structures, rate equations can be written:

$$\frac{d\Theta_1}{dt} = -1.5 \times \Theta_1 R_1 \quad (3)$$

$$\frac{d\Theta_{\sqrt{3}}}{dt} = 0.5 \times \Theta_1 R_1 - \Theta_{\sqrt{3}} R_{\sqrt{3}}, \quad (4)$$

where  $R_1$  and  $R_{\sqrt{3}}$  are the desorption rates from the  $(1 \times 1)$  and the  $(\sqrt{3} \times \sqrt{3})$  structures, respectively. Factors 1.5 in the first and 0.5 in

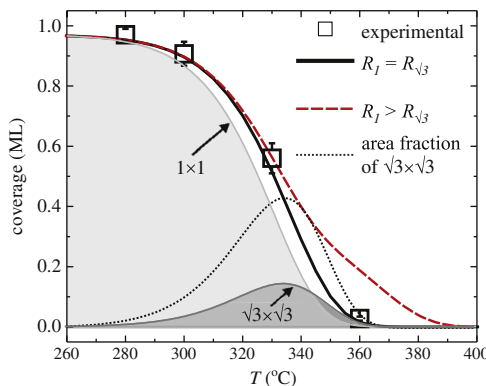


**Fig. 3.** Experimental dependence of Ti coverage (squares) on annealing temperature, fitted by first order desorption model with single desorption rate  $R_1 = R_{\sqrt{3}}$  (solid line) and with two desorption rates  $R_1 > R_{\sqrt{3}}$  (dashed line). The curves distinguished by light gray-shaded and dark gray-shaded areas underneath are  $(1 \times 1)$  and  $(\sqrt{3} \times \sqrt{3})$  components of Ti coverage with the same desorption energy. The dotted line corresponds to the area fraction of the  $(\sqrt{3} \times \sqrt{3})$  structure.

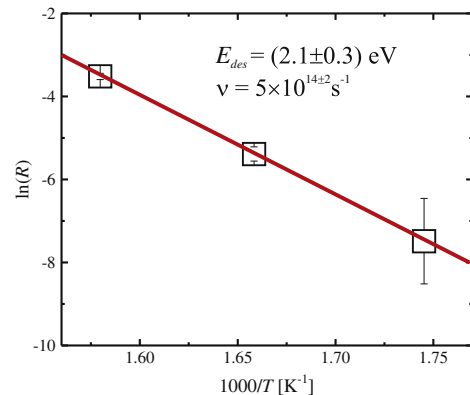


**Fig. 4.** Arrhenius plot of desorption rate  $R$  (squares) obtained from Ti coverage  $\Theta$  using Eq. (1). The solid line is a linear fit.

the second equation ensure that desorption of two atoms from the  $(1 \times 1)$  structure effectively removes three atoms from the  $(1 \times 1)$  and adds one atom to the  $(\sqrt{3} \times \sqrt{3})$  structure. If  $R_1 = R_{\sqrt{3}}$ , the sum of  $\theta_1$  and  $\theta_{\sqrt{3}}$  represents a one-component first-order desorption (FOD), which gives the same result as plotted in Fig. 3 by the solid line. To test how would a higher desorption energy of atoms in the  $(\sqrt{3} \times \sqrt{3})$  structure influence the total coverage, a result of the kinetic equations with energies of desorption set to 2.2 eV and 2.1 eV for the  $(\sqrt{3} \times \sqrt{3})$  and the  $(1 \times 1)$  structures, respectively, is plotted in Fig. 3 by the dashed line. The frequency prefactor is set to  $5 \times 10^{14} \text{ s}^{-1}$  for both structures. For coverages  $> 0.6 \text{ ML}$ , both models give the same results, because the fraction of the  $(\sqrt{3} \times \sqrt{3})$  structure is small. However, as desorption continues, a significant difference between the curves is observed. The declination from the original dependence (solid line) is evident and does not fit to the experiment. The successful fitting of the experimental dependence  $\theta(T)$  using a single parameter  $E_{\text{des}}$  for the desorption from both  $(1 \times 1)$  and  $(\sqrt{3} \times \sqrt{3})$  suggests that a bonding mechanism in both structures is similar.

With respect to the good agreement of the experimental data and their fitting described above we propose a model of structural transformations on the Tl/Si(111) surface. Starting from the  $(1 \times 1)$  structure, the  $(\sqrt{3} \times \sqrt{3})$  is locally formed by decreasing Tl coverage by desorption. Because the activation energy of Tl desorption in both structures is similar, Tl desorbs from both structures with a similar probability. The Tl atoms desorbed from the  $(\sqrt{3} \times \sqrt{3})$  are replaced by Si adatoms in order to lower the total energy, as discussed below. As a result, the mosaic phase is formed. By further desorption, Si adatoms dominate and Si metastable adatom structures are observed.

We continue by discussion of a stabilizing mechanism of the mosaic  $(\sqrt{3} \times \sqrt{3})$ -Tl structure. In the proposed scenario, the substitutional Si adatoms in the  $(\sqrt{3} \times \sqrt{3})$  structure are intrinsic, in agreement with proposals in Ref. [13]. In the  $(1 \times 1)$ -Tl structure, which covers the surface almost perfectly after heating to  $\sim 280^\circ\text{C}$ , a character of bonding is strongly ionic. It is due to a charge transfer from the monovalent [10] Tl atoms to Si dangling bonds of the bulk-terminated Si(111) surface. Ratio of the Si dangling bonds and Tl atoms is 1:1. If the same mechanism of bonding is applied to the ideal  $(\sqrt{3} \times \sqrt{3})$  structure (Fig. 1b), where the ratio is 3:1, the charge provided by monovalent Tl atoms is not sufficient to saturate Si dangling bonds completely. On the other hand, each Si adatom can provide four electrons to the structure. The Si adatoms are available on the surface from the Si-rich  $(7 \times 7)$  reconstruction and from step edges. Furthermore, the Si adatoms are highly mobile at elevated temperatures, otherwise the well shaped 2D islands of Si bilayers would not be formed (see Fig. 2a). Hence the  $(\sqrt{3} \times \sqrt{3})$ -Tl structure is likely stabilized by the Si substitutional atoms, resulting in the mosaic structure (the model is shown in Fig. 1c).

Here we note that the  $(\sqrt{3} \times \sqrt{3})$ -Tl is formed only as a result of desorption of Tl from the  $(1 \times 1)$ . If  $\sim 0.3 \text{ ML}$  of Tl is deposited to the  $(7 \times 7)$  reconstruction of Si(111) and heated to  $\sim 300^\circ\text{C}$  (or deposited on the hot surface), the  $(\sqrt{3} \times \sqrt{3})$  structure is not observed by STM. Instead, the  $(7 \times 7)$  structure remains on majority of the surface with Tl clusters inside half unit cells of the reconstruction. Minor parts of the surface, preferentially at step edges or domain boundaries, are covered by the  $(1 \times 1)$ -Tl structure [5]. This observation, confirmed by our experiments (not shown), suggests that a low concentration

of Tl is not sufficient to destroy the  $(7 \times 7)$  reconstruction and that  $(1 \times 1)$  is preferred in comparison to the  $(\sqrt{3} \times \sqrt{3})$  structure, which is formed only as a product of the desorption. When the surface with  $\sim 0.3 \text{ ML}$  of Tl is annealed to Tl desorption temperature, the original  $(1 \times 1)$  areas follow the same evolution as in the case of the surface completely covered by the  $(1 \times 1)$ . Tl is desorbed from the  $(7 \times 7)$  areas leaving clean  $(7 \times 7)$  reconstruction.

In previous LEED studies of the Si(111)/ $(\sqrt{3} \times \sqrt{3})$ -Tl surface, high intensity LEED spots were observed [4,10,9,14]. By the intuitive interpretation, the maximum intensity LEED pattern was supposed to correspond to the maximum  $(\sqrt{3} \times \sqrt{3})$  area fraction and to Tl coverage of  $1/3 \text{ ML}$ . Using our simple model, the Tl coverage  $\theta$  from Eqs. (1) and (2) can be divided into components  $\theta_1$  and  $\theta_{\sqrt{3}}$  (the corresponding fractions are shaded by light gray and dark gray in Fig. 3, respectively). The fractions are obtained from Eqs. (3) and (4) using values  $R_1 = R_{\sqrt{3}} = R$ . The area fraction of the  $(\sqrt{3} \times \sqrt{3})$  is three times higher than  $\theta_{\sqrt{3}}$ , because Tl adatom concentration in this structure is ideally  $1/3 \text{ ML}$ . This area fraction is plotted by a dotted line in Fig. 3. Maximum of the  $(\sqrt{3} \times \sqrt{3})$  fraction is 43% at  $T = 335^\circ\text{C}$ , which corresponds to STM observation – the surface is never entirely covered by the  $(\sqrt{3} \times \sqrt{3})$  during desorption. We propose, that the sharp LEED pattern [4,10,9,14] corresponds to the mosaic  $(\sqrt{3} \times \sqrt{3})$  structure (Fig. 2d) with about  $0.15 \text{ ML}$  Tl coverage. We note that in case of the  $(\sqrt{3} \times \sqrt{3})$  mosaic phase of Pb on the Si(111) surface a sharp LEED pattern was observed as well [15].

Finally we compare our results obtained for Tl with desorption of other group III metals from the Si(111) surface. In general, different techniques used in experiments discussed below gave not only different combinations of frequency prefactors and desorption energies, but also different order of desorption. To allow comparison across the results we introduce a critical temperature  $T_c$  defined as a temperature, at which one half of the initial coverage desorbs from the surface after fixed time, which we choose 120 s.

Among the group III elements, Al desorbs from the Si(111) surface at the highest temperatures. In Ref. [16], desorption from the  $(\sqrt{3} \times \sqrt{3})$ -Al structure is studied by the Auger electron spectroscopy, the obtained values of the FOD energy and prefactor were  $E_{\text{des}} = (3.8 \pm 0.1) \text{ eV}$  and  $\nu = 5.3 \times 10^{15} \text{ s}^{-1}$ , with resultant  $T_c = 790^\circ\text{C}$ . For submonolayer coverages of Ga, the FOD was observed by the Rutherford backscattering technique [17] with the activation energy of desorption  $E_{\text{des}} = (2.0 \pm 0.3) \text{ eV}$  and prefactor  $\nu = 10^{(10 \pm 3)} \text{ s}^{-1}$ . Resultant  $T_c$  is  $550^\circ\text{C}$ . In the case of In desorption in a submonolayer regime, values of  $E_{\text{des}}$  between 2.5 and  $2.9 \text{ eV}$  were reported by several techniques (see [18] and references therein) with  $\nu$  between  $10^{12}$  and  $10^{16} \text{ s}^{-1}$ , considering the FOD and  $T_c$  is in the range from 510 to  $620^\circ\text{C}$ . Interestingly, the zeroth order desorption (ZOD) was reported in contrast to the earlier works. Minami et al. used the fluorescent X-ray spectroscopy and the reflection high energy electron diffraction (RHEED) to study isothermal desorption of In from the Si(111) surface, reporting ZOD with rate of desorption dependent on superstructures formed during the desorption [19].  $E_{\text{des}}$  for the  $(\sqrt{3} \times \sqrt{3})$  superstructure was reported to be  $1.9 \text{ eV}$  and prefactor  $4.6 \times 10^8 \text{ ML/s}$ , the resultant  $T_c$  is  $605^\circ\text{C}$ . The ZOD usually indicates an existence of a 2D gas phase in equilibrium with a solid phase, which represents a reservoir of atoms for the 2D gas [20]. However, the existence of the 2D gas phase was not confirmed by RHEED, which shows sharp patterns during desorption, corresponding to the solid phase [20]. In the case of

Ga, ZOD was also reported by King et al. using temperature programmed desorption [18]. With initial coverage of 1.5 ML, a single desorption peak was fitted by the zeroth order kinetics with  $E_{des} = (2.0 \pm 0.1)$  eV and a ZOD prefactor of  $1.0 \times 10^{12 \pm 0.5}$  ML/s, giving  $T_C$  of 435 °C.

Our results show that desorption of Tl can be described by the kinetics with a simple bond-breaking mechanism. The value  $E_{des} = (2.1 \pm 0.3)$  eV is close to the activation energy of Ga desorption and smaller than  $E_{des}$  of In, when considering the first order desorption. The rather high value of prefactor  $\nu = 5 \times 10^{14 \pm 2}$  s<sup>-1</sup> results in desorption at significantly lower temperatures, compared to both Ga and In. The value of  $T_C = 350$  °C is the lowest among the compared group III elements. This can be explained by a qualitatively different bonding mechanism, in which only single valence electron per adatom is active.

#### 4. Conclusion

Particular stages of thallium desorption from the Si(111) surface were observed by STM, i.e. formation of the  $(\sqrt{3} \times \sqrt{3})$  structure by desorption of Tl from the  $(1 \times 1)$  surface and formation of Tl-free Si metastable structures by desorption of Tl from the  $(\sqrt{3} \times \sqrt{3})$  structure. Once the  $(1 \times 1)$  structure is canceled, the  $(\sqrt{3} \times \sqrt{3})$  mosaic phase is formed, while ideal Tl- $(\sqrt{3} \times \sqrt{3})$  without Si substitutional atoms has been never observed. It is concluded that a significant amount of the substitutional Si atoms is necessary to stabilize the  $(\sqrt{3} \times \sqrt{3})$  structure, resulting in the mosaic phase. By fitting the observed temperature dependence of the amount of residual Tl on the surface by means of a first order desorption, we obtained the desorption energy  $(2.1 \pm 0.3)$  eV for Tl in both  $(1 \times 1)$  and  $(\sqrt{3} \times \sqrt{3})$  structures. From successful fitting by the single desorption energy we

derive that a nature of Tl bonding in both  $(1 \times 1)$  and  $(\sqrt{3} \times \sqrt{3})$  structures is similar.

#### Acknowledgment

This work was supported by The Grant Agency of the Czech Republic, Project No. 202/09/P033 of GACR.

#### References

- [1] K. Sakamoto, T. Oda, A. Kimura, K. Miyamoto, M. Tsujikawa, A. Imai, N. Ueno, H. Namatame, M. Taniguchi, P.E.J. Eriksson, R.I.G. Uhrberg, Phys. Rev. Lett. 102 (2009) 096805.
- [2] Y. Bychkov, E. Rashba, JETP Lett. 39 (1984) 78.
- [3] K. Yaji, Y. Ohtsubo, S. Hatta, H. Okuyama, K. Miyamoto, T. Okuda, A. Kimura, H. Namatame, M. Taniguchi, T. Aruga, Nat. Commun. 1 (2010) 17.
- [4] S.S. Lee, H.J. Song, N.D. Kim, J.W. Chung, K. Kong, D. Ahn, H. Yi, B.D. Yu, H. Tochihara, Phys. Rev. B 66 (2002) 23312.
- [5] V.G. Kotlyar, A.A. Saranin, A.V. Zotov, T.V. Kasyanova, Surf. Sci. 543 (2003) L663.
- [6] T. Noda, S. Mizuno, J.W. Chung, H. Tochihara, Jpn. J. Appl. Phys. 42 (2003) L319.
- [7] N.D. Kim, C.G. Hwang, J.W. Chung, T.C. Kim, H.J. Kim, D.Y. Noh, Phys. Rev. B 69 (2004) 195311.
- [8] S. Özkaya, M. Çakmak, B. Alkan, Surf. Sci. 602 (2008) 1376.
- [9] K. Sakamoto, P.E.J. Eriksson, N. Ueno, R.I.G. Uhrberg, Surf. Sci. 601 (2007) 5258.
- [10] K. Sakamoto, P.E.J. Eriksson, S. Mizuno, N. Ueno, H. Tochihara, R.I.G. Uhrberg, Phys. Rev. B 74 (2006) 075335.
- [11] Prepared for publication.
- [12] M. Koike, Y. Einaga, H. Hirayama, K. Takayanagi, Phys. Rev. B 55 (1997) 15444.
- [13] A. Visikovskiy, Structural investigations of thallium adsorption on Si(100) and Si(111) surfaces, Ph.D. thesis, Kyushu University, Japan (2006).
- [14] A. Visikovskiy, S. Mizuno, H. Tochihara, Surf. Sci. 600 (2006) L189.
- [15] E. Ganz, H. Ing-Shouh, X. Fulin, S.K. Theiss, J. Golovchenko, Surf. Sci. 257 (1991) 259.
- [16] A. Saranin, E. Khramtsova, V. Lifshits, Surf. Sci. 302 (1994) 57.
- [17] M. Zinke-Allmang, L. Feldman, Surf. Sci. Lett. 191 (1987) L749.
- [18] S. King, R. Davis, R. Nemanich, Surf. Sci. 602 (2008) 405.
- [19] N. Minami, Y. Machida, T. Kajikawa, T. Sato, K. Ota, S. Ino, Surf. Sci. 524 (2003) 1995.
- [20] K. Nagai, T. Shibanuma, M. Hashimoto, Surf. Sci. 145 (1984) L459.

# 5. Single-atom adsorbates on the Si(111)/Tl-(1×1) surface

At the beginning of our study, there were no published works focusing on the interaction of adsorbates with the Si(111)/Tl – (1 × 1) surface. The only exception is the study of Vitali et al. showing very weak bonding between the first and the second Tl layer if more than 1 ML of Tl is deposited [20]. In the following chapter we describe our results of the Mn, In and Sn layers on top of the Tl-passivated surface. The atomic adsorbates were primarily used for testing the stability of the Tl layer before the deposition of organic adsorbates. In the second part of the chapter we use the Tl passivation layer as a mediator allowing growth of Si-metal reconstructions at a lower temperature compared to the direct deposition.

## 5.1 Growth of Mn, In and Sn layers on the Tl-passivated Si(111) surface

As written above, Tl and the Tl-passivated Si(111) surface exhibit unique properties which are extraordinary among other chemical elements and surfaces. From the applications point of view, the most interesting property is a large spin splitting of electronic states near the Fermi level [17, 80]. In order to utilize the splitting, the split surface states are required to be metallic [81]. The ideal Si(111)/Tl – (1 × 1) surface has a bandgap of 0.34 eV. Spin-split surface bands do not cross the Fermi level, therefore they cannot be used for generation of spin-polarized electrons. However, metalicity of the surface states can be induced by surface point defects [79, 82] or by creating a dense 2D metal-Tl alloy [83, 84].

In the paper I (page 52) we study the behavior of three different atomic adsorbates: Mn, In and Sn. Mn, known for its reactivity with bare silicon substrates [85, 86], was chosen for testing the stability of the Tl layer. In and Sn were chosen as potential candidates for formation of the dense 2D alloys, which could induce formation of metallic spin split surface bands.

Results of our study can be summarized as follows:

- manganese atoms aggregate to stable 3D dendritic islands nucleated on Si steps
- indium atoms form compact flat islands that are unstable during observation and interact with the electric field of the STM tip
- tin atoms intermix with Tl atoms and arrange into an array of triangular objects
- diffusion barriers for all studied adsorbates are strongly reduced compared to those on the initial (7 × 7)-reconstructed Si(111) surface
- even though the growth modes of Mn, In and Sn are significantly different, all the modes are similar to those found on less reactive metal substrates

The results suggest that Sn and Tl form a dense 2D alloy that is a candidate for spin split metallic bands. Moreover, we show that the Tl – (1 × 1) layer can be used as a passivation agent and a modifier of adsorbate growth on the Si(111) surface. This use of the Tl – (1 × 1) layer is discussed in the rest of this work.

My contribution to the paper I can be summarized as follows. I obtained all experimental data presented in the paper. I analyzed the data and prepared them for the publication. With the help of co-authors I wrote the manuscript.



## Diverse growth of Mn, In and Sn islands on thallium-passivated Si(1 1 1) surface



P. Matvija\*, P. Sobotík, I. Ošt'ádal, P. Kocán

Charles University in Prague, Faculty of Mathematics and Physics, Prague, Czech Republic

### ARTICLE INFO

#### Article history:

Received 4 November 2014

Received in revised form 9 January 2015

Accepted 11 January 2015

Available online 20 January 2015

#### Keywords:

Thallium

Si(1 1 1)

Passivation

Thin film growth

Growth modes

Scanning tunneling microscopy

### ABSTRACT

Controlled growth of thin films on highly reactive silicon surfaces has been a challenge for decades. High density of surface dangling bonds, however, hinders the adsorbate diffusion and its self-organization. In our work, we propose a novel use of the Tl-(1 × 1) layer as a passivating agent, which highly enhances diffusion of adsorbates by saturating all dangling bonds of the Si substrate.

We use room-temperature scanning tunneling microscopy to study structures formed on the Si(1 1 1)/Tl-(1 × 1) surface after deposition of submonolayer amounts of three elemental adsorbates: Mn, In and Sn. As a result, three significantly different surface structures are observed. Manganese atoms aggregate to stable dendritic islands nucleated on Si steps. Indium islands are compact and unstable during observation. Unlike Mn and In, Sn atoms intermix with Tl atoms and arrange into an array of triangular objects.

The growth kinetics of the three deposited metals on the Tl-(1 × 1) layer is discussed and compared with the kinetics observed in previously studied systems. The comparison shows that the growth of the layers adsorbed on the Tl-passivated surface is similar to the growth of the adsorbate layers on less reactive metal surfaces.

© 2015 Elsevier B.V. All rights reserved.

### 1. Introduction

Controlled growth of thin films has been for many years a key driver in the surface science and related technological applications like thin film transistors. In order to obtain defect-free flat films on highly reactive (typically silicon or germanium) surfaces, a transformation method called passivation is often used [1]. Among other passivated surfaces, the Si(1 1 1)/Tl-(1 × 1) [2] has been shown to have outstanding properties [3]. Despite the fact that the surface behaves as ideally passivated one (stable, inert and with completely saturated surface dangling bonds [4,5]), it has never been used as a substrate for further growth of adsorbates. The only exception is the study of interaction of the second Tl layer with the Si(1 1 1)/Tl-(1 × 1) surface showing very weak bonding between Tl layers [5].

Thallium exhibits unique properties, which are extraordinary among other chemical elements. First of all, an inert-pair effect results in an opportunity to act monovalently in various reconstructions [4,6,7]. Above that, thallium, as a heavy element (atomic number 81), exhibits large spin-orbit coupling. The

coupling in the two-dimensional Tl-(1 × 1) surface layer induces unusually large Rashba spin-splitting of surface bands [3], which is of a great value for a potential use in future spintronic devices [8].

The Si(1 1 1)/Tl-(1 × 1) surface can be prepared by deposition of one monolayer (1 ML =  $7.83 \times 10^{14}$  atoms cm<sup>-2</sup>) of Tl on the Si(1 1 1)-(7 × 7) surface and annealing at  $\approx 300^\circ\text{C}$  [4]. The surface is stabilized by electrons that are transferred from Tl 6p orbitals to Si dangling bonds. In the structure, Tl atoms are located in T<sub>4</sub> positions of the bulk-terminated Si surface [4,9–11].

In order to utilize the large spin-splitting in the Tl-(1 × 1) layer, the split surface states are required to be metallic. As it was determined by the scanning tunneling spectroscopy (STS) [5] and photoemission spectroscopy supported by ab-initio calculations [4], the clean Si(1 1 1)/Tl-(1 × 1) surface has a bandgap ( $\approx 0.5$  eV and  $0.34$  eV, respectively). Spin-split surface bands do not cross the Fermi level; therefore they cannot be used for generation of spin-polarized electrons. However, as Gruznev et al. [12,13] recently showed, spin-split metallic bands can be created by using a dense 2D alloy layer containing a metal with strong spin-orbit coupling (e.g. Tl) and another metal which modifies the surface reconstruction. Experimentally, it has been shown that metallicity of the Si(1 1 1)/Tl-(1 × 1) surface can be also naturally induced by the presence of defects in the passivating layer [14,15].

\* Corresponding author. Tel.: +420 221 912 342.  
E-mail address: matvija.peter@gmail.com (P. Matvija).

In our work, we use a room-temperature scanning tunneling microscopy (STM) to observe the growth of three elemental adsorbates (Mn, In and Sn) deposited on the Si(1 1 1)/Tl – (1 × 1) surface in submonolayer amounts. Experiments show that the studied adsorbates behave very diversely. By the intra-comparison of the surface morphologies and the comparison with previously studied systems we determine kinetic models of the growth. The models give insight into the substrate–adsorbate and adsorbate–adsorbate interactions on the Si(1 1 1)/Tl – (1 × 1) surface.

## 2. Experimental

Experiments were carried out in an ultra-high vacuum non-commercial STM apparatus with a base pressure below  $8 \times 10^{-9}$  Pa. Pressure during the experiments was sustained within the order of  $10^{-8}$  Pa. The Si(1 1 1) – (7 × 7) surface was prepared on the Sb-doped Si monocrystal (resistivity 0.005–0.01 Ω cm) by flashing to  $\approx 1200^\circ\text{C}$ .

The Si(1 1 1)/Tl – (1 × 1) surface was prepared by the thermal deposition of 1 ML of thallium (purity 99.999%) on the Si(1 1 1) – (7 × 7) surface and annealing at  $\approx 300^\circ\text{C}$  for 2 min [4]. The samples were resistively heated by passing DC current. Manganese, indium and tin were deposited on the passivated surface after cooling down the sample to room temperature ( $20\text{--}40^\circ\text{C}$ ). Resistively heated tantalum and tungsten evaporators were used for the deposition.

Sample temperature was determined with absolute and relative measurement accuracies of  $\pm 30^\circ\text{C}$  and  $\pm 10^\circ\text{C}$ , respectively. The deposition rates and the deposited amounts were measured by a quartz crystal thickness monitor. Coverages and distances were estimated from the STM images with a relative error of 15%. Presented X and Y dimensions of each STM image already account for calibrated piezo and thermal drifts. Hereafter, only mean values without respective errors are stated in cases they agree with the above stated errors.

## 3. Results and discussion

### 3.1. Si(1 1 1)/Tl-(1 × 1)

**Fig. 1** displays the clean Si(1 1 1)/Tl – (1 × 1) surface before the deposition of metals. **Fig. 1(a)** shows Tl-covered Si islands evenly distributed over the surface (some of the islands are marked by black arrows). The islands are formed during the post-deposition annealing of the Si(1 1 1)/Tl surface, when the (7 × 7)-reconstructed Si surface transforms into the (1 × 1)-reconstructed one [7]. In this process, excess Si atoms are excluded to the surface and create islands, which are covered by Tl (see the schematic drawing of the cross-section of the surface in **Fig. 1(b)**). The step edges of Tl-covered Si islands are essentially of the same nature as the step edges of Tl-covered Si terraces. Hence, in this work Tl-covered Si terraces and Tl-covered Si islands are referred as “terraces” and “Si islands”, respectively. The density and the size of the Si islands vary and depend on exact experimental conditions during the preparation of the Si(1 1 1)/Tl – (1 × 1) surface.

### 3.2. Si(1 1 1)/Tl-(1 × 1)/Mn

In order to use the Si(1 1 1)/Tl – (1 × 1) surface as a substrate for further deposition of adsorbates, it is necessary to examine the stability of the passivating layer. In our study we have tested the stability by deposition of Mn, which is known for its high reactivity with bare silicon surfaces [16,17]. We have performed experiments with two different amounts of deposited Mn:  $(0.18 \pm 0.05)$  ML and  $(0.35 \pm 0.10)$  ML.

The Si(1 1 1)/Tl – (1 × 1) surface after the deposition of the smaller amount of Mn is presented in **Fig. 2(a)**. The figure shows Tl-covered Si islands surrounded by several bright clusters (some of them are marked by white arrows). Since the clusters are not present on the surface before the deposition of Mn (see **Fig. 1**), we conclude that they consist of nucleated Mn atoms.

**Fig. 2(c)** presents the detailed image of the surface. It displays two terraces and one Si island. A few Mn islands are nucleated on the Si island and terrace step edges. For the insight into the vertical topography the figure also includes a height profile which is placed under the image. A contour from which the profile is extracted is marked by a blue dotted line “1”. The line crosses three Mn islands which are assigned to the peaks of the profile by gray dotted arrows. Taking into account the known composition and topography of all objects in the figure, we constructed a simplified explanatory drawing of the cross-section of the surface, which is displayed in the inset of **Fig. 2(a)**.

**Fig. 2(b)** presents the surface with a higher deposited amount of Mn. Two displayed terraces are separated by a step edge which runs from the top right corner to the bottom left corner of the image. The edge is decorated by Mn islands elongated in a direction perpendicular to the step (two of the islands are marked by white dotted arrows). Si islands (one of them is marked by a black solid arrow), surrounded by highly-branched Mn islands (white solid arrows), are evenly distributed over both terraces. In contrast with the low-coverage case, where no preferred growth orientation is visible, at higher coverage Mn islands grown on Si islands form triangularly enveloped dendritic structures (marked by blue-dotted equilateral triangles). All envelopes are congruently oriented: one side is parallel to the  $[1\bar{1}0]$  direction and one apex is pointing in the  $[11\bar{2}]$  direction.

**Fig. 2(d)** displays a detail of a step edge between two terraces. Two height profiles (placed on the right side of the figure) are extracted from the image. Positions of the profiles are marked by the pink and blue dotted lines, which cross Mn islands nucleated next to an Si island and a step edge of a terrace, respectively. As can be seen from **Fig. 2(d)**, Mn islands nucleated on the top of step edges merge with those that are nucleated on the bottom. It is noteworthy that (i) gradually descending profiles of Mn islands are formed at Si steps and (ii) longer parts of the merged Mn islands are located on tops of edges. The latter phenomenon can be explained as follows. The annealing of the Si(1 1 1)/Tl surface at  $300^\circ\text{C}$  causes nucleation of Si islands as well as growth of terraces due to nucleation of Si atoms on step edges. The outer border areas of terraces are newly nucleated, hence much lower concentration of defects and Si islands are observed on them. The shielding effect of Si islands blocks most of the deposited Mn atoms from nucleation on the bottom side of terrace step edges. On the other hand, lower concentration of Si islands in the vicinity of steps on top terraces enables more Mn atoms to diffuse to top sides of step edges and nucleate there.

The average apparent height of Mn islands (measured from the bottom terraces of steps) is determined to be 2.3 times the height of an Si step (i.e. 0.72 nm). However, as it is illustrated by the profile “1” of **Fig. 2(c)**, height of individual Mn islands varies significantly (as much as 25%). These observations of gradually descending profiles and high variance of height of the Mn islands indicate that, although an inner structure of Mn islands has not been resolved, ordering of Mn atoms in the islands is only short-range.

Growth of dendritic islands as those observed in **Fig. 2(b)** can be found in many metal-on-metal surface systems (e.g. Ir(1 1 1)/Au, Pt(1 1 1)/Au [18] or Pt(1 1 1)/Ag [19]). Monte Carlo simulations of such a growth unveiled that two conditions are necessary for the growth of dendritic islands: (i) high mobility of deposited atoms on the surface and either (ii-a) low diffusivity of nucleated atoms along islands edges [18], (ii-b) a high

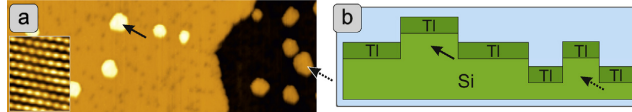


**Fig. 1.** The Si(111)/Tl-(1×1) surface before deposition of adsorbates: (a) typical STM image of the surface ( $50\text{ nm} \times 150\text{ nm}$ ,  $U_{\text{sample}} = -0.3\text{ V}$ ,  $I_{\text{tunnel}} = 0.3\text{ nA}$ ); inset shows a high resolution image of the Tl-(1×1) structure ( $2.5\text{ nm} \times 3.0\text{ nm}$ ,  $U_{\text{sample}} = 0.2\text{ V}$ ,  $I_{\text{tunnel}} = 0.2\text{ nA}$ ); (b) schematic drawing of the cross-section of the surface. Solid and dotted black arrows indicate some of the Tl-covered Si islands on the top and the bottom terrace respectively.

island-corner diffusion barrier [20] or (ii-c) anisotropic corner diffusion [19].

Based on the stated observations a kinetic model of the growth can be formulated as follows. Mn atoms deposited on top of the Tl-(1×1) layer diffuse quickly on the low-corrugated passivated surface until they hit an Si step. After an attachment to the Si step, Mn atoms significantly decrease their mobility and create nucleation centers which are evenly distributed along Si step edges (no coalescence of neighboring Mn islands has been observed in initial stages of the growth). Very low or anisotropic diffusion of Mn along edges of Mn islands and a shielding effect of already nucleated Mn clusters lead to formation of highly-branched Mn clusters with triangular envelopes nucleated on Si islands. The growth of Mn clusters nucleated on Si steps is predominantly governed by the shielding effect, which results in formation of evenly distributed single-branched Mn clusters perpendicular to step edges.

### 3.3. Si(111)/Tl-(1×1)/In

In comparison with Mn, significantly different behavior is observed in the case of In deposited onto the Si(111)/Tl-(1×1) surface. Fig. 3(a) shows a representative area of the surface with four In islands (two of them are marked by dashed pink arrows). In contrast to Mn, we do not observe any preference of In islands to grow in the vicinity of Si islands (two of them are marked by dashed white arrows) and steps. Thus, despite we do observe that In islands are frequently connected with Si islands, Si islands do not serve as centers for the nucleation of In islands. This is a sign of no interaction or only a small attractive interaction between In atoms and Si step edges (the interaction is much smaller than in the case of Mn). A simplified schematic drawing of the cross-section of the surface, which reflects the observed topography, is placed in the joint inset of Fig. 3(b) and (c).

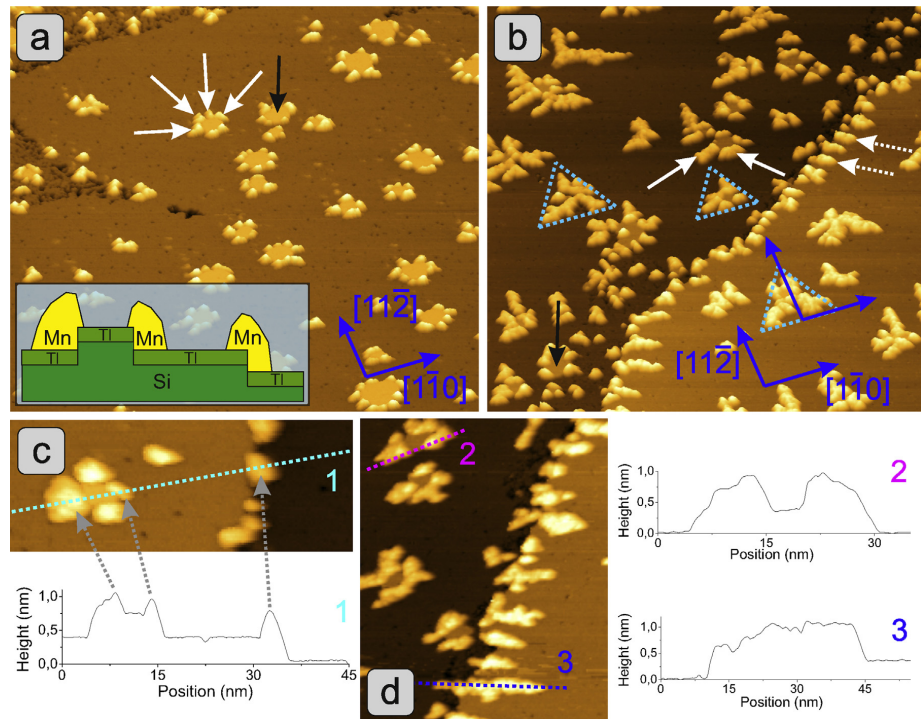


**Fig. 2.** Surfaces prepared by the deposition of two different amounts of Mn on the Si(111)/Tl-(1×1) surface: (a)  $(0.18 \pm 0.05)\text{ ML}$  of Mn (inset: schematic drawing of the cross-section of the surface); (b)  $(0.35 \pm 0.10)\text{ ML}$  of Mn; (c) detailed image of the surface covered by  $(0.18 \pm 0.05)\text{ ML}$  of Mn and a height profile extracted from the image; (d) detailed image of the surface covered by  $(0.35 \pm 0.10)\text{ ML}$  of Mn and two height profiles extracted from the image. White and black arrows indicate Mn and Si islands, respectively. Image conditions (image size, sample bias voltage, tunneling current): (a)  $250\text{ nm} \times 250\text{ nm}$ ,  $-0.5\text{ V}$ ,  $0.25\text{ nA}$ ; (b)  $250\text{ nm} \times 250\text{ nm}$ ,  $+1.9\text{ V}$ ,  $0.3\text{ nA}$ ; (c)  $60\text{ nm} \times 12\text{ nm}$ ,  $-0.5\text{ V}$ ,  $0.25\text{ nA}$ ; (d)  $85\text{ nm} \times 110\text{ nm}$ ,  $+1.9\text{ V}$ ,  $0.3\text{ nA}$ . (For interpretation of the references to color in text, the reader is referred to the web version of this article.)

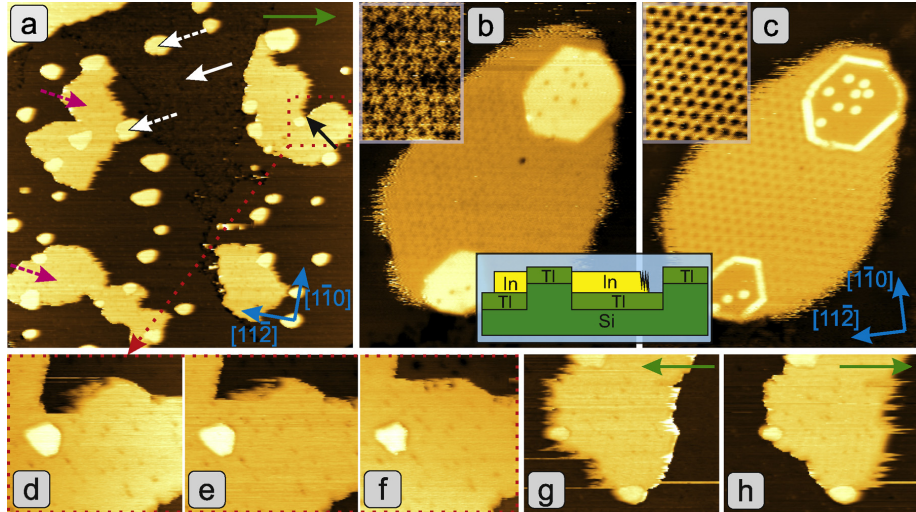


**Fig. 3.** STM image of the Si(111)/Tl-(1×1)/In surface – 0.27 ML of In: (a) representative image of the surface; (b, c) two images of the same island at different biases (a detailed inner structure in insets; a schematic drawing of grown structures in the joint inset); (d–f) evolution of a sub-area from (a) during the scanning (a solid black arrow in (a) indicates an area which is gradually filled by In atoms); (g, h) the same In island scanned in two directions at opposite sample biases. Solid green arrows indicate a direction of tip movement during the scanning. Dashed pink and dashed white arrows indicate indium and silicon islands, respectively. Solid white arrow indicates a defected area of the Tl-(1×1) reconstruction. Image conditions (image size, sample bias voltage, tunneling current, scanning speed): (a) 350 nm × 350 nm, +2 V, 0.3 nA, 2800 nm/s; (b) 40 nm × 60 nm, -2 V, 0.4 nA, 260 nm/s (inset: 11 nm × 18 nm, -2 V, 0.4 nA); (c) 40 nm × 60 nm, +1 V, 0.4 nA, 260 nm/s (inset: 12 nm × 18 nm, +1 V, 0.25 nA); (d) 80 nm × 90 nm, -1.3 V, 0.2 nA, 1900 nm/s; (e) 80 nm × 90 nm, -0.5 V, 0.2 nA, 2800 nm/s; (f) 80 nm × 90 nm, -0.5 V, 0.2 nA, 1500 nm/s; (g) 100 nm × 90 nm, -2 V, 0.3 nA, 1850 nm/s; (h) 100 nm × 90 nm, +2 V, 0.3 nA, 1850 nm/s. (For interpretation of the references to color in this figure legend, the reader is referred to the web version of this article.)

Fig. 3(b) and (c) present STM images reflecting an inner structure of In islands. The figures display the same In island placed between two hexagonal Tl-covered Si islands. The Si islands contain a few dot defects of the Tl-(1×1) layer [7] (they appear as dark circles on Si islands in Fig. 3(b) and as bright circles in Fig. 3(c)). The surface of the In island is imaged at two different sample biases (-2 V and +1 V, respectively). In both cases, the In island exhibits a hexagonally symmetric pattern with a 1.8 nm periodicity, which is approximately 4.6× the periodicity of the (1×1)-reconstructed Tl layer. The similar structure has been observed on the Si(111)/Tl-(1×1)/Tl surface, where Tl in the second layer forms a low-corrugated structure with approximate (6×6) periodicity [5]. The structure can be explained as a Moiré pattern which emerges as a result of an electronic interference of two layers of Tl. Generally, a Moiré surface pattern can be observed on planar systems that consist of two congruent lattices (one lattice lying on top of another one). The pattern can be generated by both rotation and different lattice constants of the two lattices. In the former case, the Moiré pattern rotates together with the rotation of one of the lattices. However, the pattern on the In islands of the Si(111)/Tl-(1×1)/In surface is always aligned with edges of Si islands (see Fig. 3(c)). Thus, the In lattice is oriented in the same direction as the lattice of the Tl-(1×1) reconstruction. On the other hand, In is weakly bound to the passivated substrate (shown below), which enables its lattice to relax laterally. On the basis of the stated observations, we managed to reproduce the periodicity of the Moiré pattern by the In hexagonal surface lattice with the periodicity ≈0.32 nm.

As another contrast to stable Mn islands, edge atoms of In islands remain mobile at room temperature, suggesting weak bonding to the substrate and weak intra-island bonding of In atoms. We observed two experimental indications of this statement. The first one can be seen in Fig. 3(d–f). The figures display an evolution of

an In island during the scanning. A small gap in In island presented in the first scan (see the solid black arrow in Fig. 3(a)) is gradually filled by In atoms and disappears in Fig. 3(f).

Fig. 3(g) and (h) presents the second evidence of the mobility. The displayed In island is scanned in two directions at opposite sample biases (directions of scanning are marked by solid green arrows). In relation to the scanning direction, trailing edges of In islands are always more ragged than leading edges. This observation is reflected in the schematic drawing of the surface in Fig. 3 as raggedness of one side of the In island. On the other hand, edges of neighboring Si islands are smooth (not ragged) independently on the scanning direction. This rules out the possibility that the raggedness of In islands is the scanning artifact of the feedback. We explain the observed raggedness as follows. Based on Fig. 3(d–f), we know that In islands change their shape during the scanning at room temperature. The change is caused by the weakly bonded, mobile In adatoms in vicinity of In islands. During the scanning, the STM tip may cause additional attraction or repulsion to the weakly bonded atoms and temporarily drag an In atom over the weakly corrugated surface. Note that the raggedness of trailing edges of In islands is more pronounced when the scanning speed is higher (Fig. 3(a–d)) since the dragged In atom passes longer distance until the weak tip-adatom bond is broken by thermal fluctuations. The tip-induced mobility of adatoms has been already observed on similar surfaces: Si(100)/Tl [21], Si(100)/In [22], Si(111)/In [23]. As a result of the weak binding of In atoms to the substrate and Si steps, In islands are significantly more compact than Mn islands. In spite of the striking difference, we note that both growth scenarios may be considered as two different cases of the same fractal diffusion-limited growth.

Nucleation of the second In layer on existing In islands was not observed. We suppose that In atoms which were originally

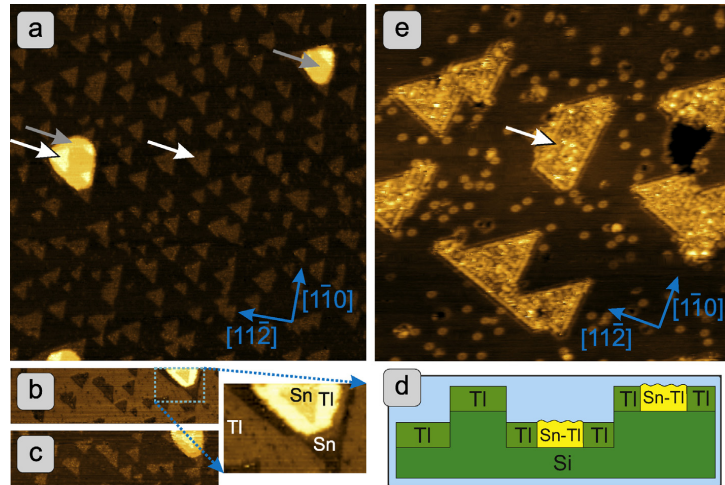


**Fig. 4.** STM image of the Si(111)/Tl-(1×1)/Sn surface – 0.22 ML of Sn: (a) representative image of the surface; (b, c) two images of the same area of the surface obtained at two opposite sample biases ( $\pm 1$  V); (d) explanatory schematic drawing of the cross-section of the surface (e) detailed image of the surface. White and gray arrows indicate Sn-Tl and Si islands, respectively. Image conditions (image size, sample bias voltage, tunneling current): (a) 240 nm × 290 nm, +1.9 V, 0.3 nA; (b) 250 nm × 40 nm, −1 V, 0.3 nA; (c) 250 nm × 40 nm, +1 V, 0.3 nA; (e) 50 nm × 60 nm, +2.3 V, 0.17 nA.

deposited on an In island either diffuse to island edges or directly incorporate into the island at a deposition site.

An analogous type of growth has been observed for other, mostly high-temperature, systems (e.g. Au on Ru(0001) at 500 K [24] or TiN on TiN at  $\approx 1150$  K [25]). A kinetic model of In on the Si(111)/Tl-(1×1) can be formulated as follows: Due to weak bonding of In atoms, diffusion along island edges and detachment from the edges is frequent at room temperature. As a result, compact but unstable 2D islands are formed on the surface.

### 3.4. Si(111)/Tl-(1×1)/Sn

Interaction of tin – the third studied adsorbate – with the Si(111)/Tl-(1×1) surface qualitatively differs from Mn and In. Fig. 4(a) displays a representative image of the Si(111)/Tl-(1×1) surface after deposition of 0.22 ML of Sn. The displayed area contains Si islands (two of them are marked by gray arrows) and evenly distributed triangular objects (two of them are marked by white arrows). The triangular objects cover 22% of the surface. No such structure has been observed on the clean Si(111)/Tl-(1×1) surface before the deposition of Sn; therefore we conclude that the objects contain the deposited Sn in the concentration of 1 ML (i.e. in the same concentration as surface atoms in the (1×1) reconstruction). Hereafter, we refer to the triangular objects as “Sn islands”. All Sn islands are congruently oriented with one apex pointing in the [112] direction. Nucleation of the islands occurs evenly on the surface. Besides these evenly distributed Sn islands, Si islands are often decorated by Sn as well, as shown in the magnified part of Fig. 4(b).

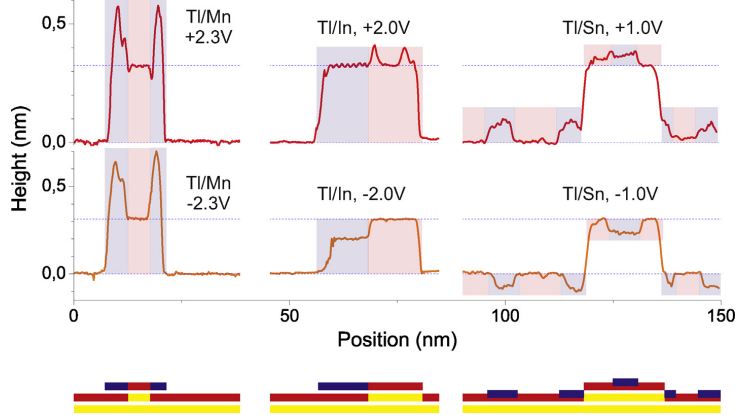
In comparison with Mn and In, Sn islands are considerably smaller. If we take into account similar coverages of all three surfaces and roughly the same deposition rates ( $0.05 \pm 0.03$  ML/min), we can conclude that the diffusivity of Sn atoms on the passivated surface is smaller than the diffusivity of the former two adsorbates.

Fig. 4(b) and (c) shows two images taken simultaneously from the same area of the surface at opposite bias voltages. Apparently, triangular islands in the images are displayed inversely – they

appear darker (brighter) than the Tl-(1×1) layer at  $-1$  V ( $+1$  V) sample bias, respectively. The inverse contrast is obtained due to a different bias between the STM tip and the surface; therefore we can conclude that it has an electronic (not topographical) nature. Comparison of typical island line profiles (Fig. 5) reveals that the apparent height of Sn islands over the thallium layer is significantly smaller than in the case of Mn or In. Observed apparent heights of islands in empty state STM images are: Mn:+0.6 nm, In:+0.32 nm and Sn:+0.09 nm while in occupied states they are: Mn:+0.7 nm, In:+0.2 nm and Sn:−0.07 nm. This suggests that Sn atoms are located much lower on the surface and probably create a reconstruction within the Tl layer, as schematically illustrated in Fig. 4(d). Since no evidence of Tl atoms in the second layer (on a top of the Tl-(1×1) reconstruction) has been observed, we suggest that triangular islands contain Tl atoms in the surface concentration of 1 ML as well.

The exact structure and composition of the islands cannot be concluded from our measurements, but the presented experimental data suggest that Sn and Tl atoms in Sn-Tl islands form a dense reconstruction. Similar model systems with one of the elements (Tl) able to induce a large spin-splitting have been proposed by Gruznev et al. [12] as possible generators of spin-polarized electrons. In order to show whether the Si(111)/Tl-(1×1)/Sn surface can be used for this purpose, a thorough study of its atomic and electronic structure needs to be executed.

Due to the probable creation of mixed Sn-Tl reconstruction, a kinetic model of the growth of Sn-Tl islands cannot be formulated as simply as in the case of Mn and In. Based on the presented data, we suggest two possible scenarios of the creation of Sn-Tl islands. Deposited Sn atoms either diffuse on the passivating layer or directly penetrate deeper into the Si(111)/Tl-(1×1) surface and diffuse there (the possibility of sub-surface diffusion channels on passivated Si surfaces has been previously shown [26]). The Sn-Tl reconstructed islands form at sites with sufficiently high local concentration of Sn atoms. Smooth edges in <1, 1, 0> directions are strongly preferred, which results in triangular shape of the islands (the symmetry is inherited from the symmetry of the substrate).



**Fig. 5.** Typical line profiles of Mn, In and Sn islands on the Si(111)/Tl-(1×1) surface. Blue horizontal lines indicate height of the Tl-covered Si islands. Red and blue transparent rectangles indicate positions of the bare Tl-(1×1)-reconstructed surface and adsorbate islands on the surface respectively. The schematic diagram in the bottom part of the figure indicates position of Si (yellow), Tl (red) and adsorbate (blue) layers on the upper surfaces. (For interpretation of the references to color in this figure legend, the reader is referred to the web version of this article.)

### 3.5. Si(111)/Tl-(1×1) versus metal surfaces

In many aspects, room-temperature growth of metals on the Tl passivated surface is similar to growth of metals on metal surfaces at various temperatures. For instance, on the Ru(0001) substrate, Au forms dendritic and compact islands at room and 500 K temperature, respectively, and Co forms triangular islands at room temperature [24]. Another example is growth of Al on the Pt(111) substrate [27], which at different temperatures exhibits all three types of islanding observed in our study. At room temperature, Al forms dendritic islands (as Mn), which transform into compact ones (as In) after annealing at 500 K. At temperature above 800 K, Al incorporates directly into the top layer and creates Pt-Al alloy (as Sn).

Metals are known to have relatively inert and chemically inactive surfaces. Adatoms on these surfaces are weakly bonded and create a 2D gas of mobile adatoms even at room temperature [28,29]. On the other hand, growth of most elemental adsorbates on the Si(111) surface leads to formation of strong bonds between adsorbates and Si substrate, which hinder further diffusion and organization of adsorbed atoms. Our experiments show that adsorbates on the Tl-passivated Si(111) surface are all weakly bonded to the substrate while diffusing on the Tl-(1×1) layer. As a result, during the growth on the Tl-passivated substrates adsorbates behave similarly to the case of adsorbates on less reactive metal surfaces.

Quantitatively, the similarity between metal surfaces and the Si(111)/Tl-(1×1) surface can be expressed in terms of the height of an energetic barrier for diffusion of adsorbates. On the basis of our experiments, we can roughly estimate the energy barriers of Mn and Sn after strongly simplifying the growth model with following assumptions: (i) the observed density of islands is the saturated one and (ii) the critical size of a nucleus is 1. Then, according to the mean-field nucleation theory, the saturation density of all stable clusters  $n_x$  on the hexagonal lattice depends on deposition flux  $F$  and the adatom diffusion barrier  $E_D$  as follows [29,30]:

$$n_x \approx \eta(\Theta) \left( \frac{3F}{\nu_0} \right)^{1/3} \exp \left( \frac{E_D}{3kT} \right), \quad (1)$$

where  $\eta$  denotes the pre-exponential numerical factor dependent on the coverage  $\Theta$ . The value of  $\eta$  in conditions of our experiments

has been estimated to be  $(0.2 \pm 0.1)$ , see Fig. 6 in [31]. The exponential prefactor  $\nu_0$  is assumed to be  $10^{(12 \pm 1)} \text{ s}^{-1}$  as in the case of other metal-on-metal systems [30,32,33]. In the case of Sn, the observed island density ( $5.5 \times 10^{11} \text{ cm}^{-2}$ ) is assumed to be the saturated value  $n_x$ . Since Mn clusters are nucleated primarily on Si steps and the density of Mn clusters without the presence of the steps would be significantly lower, we use the density of Si islands ( $1.1 \times 10^{11} \text{ cm}^{-2}$ ) as the highest estimate for the density of the Mn clusters on the flat surface. The effect of Si steps on the growth of Sn islands is neglected.

As a result the following diffusion barriers were obtained:  $E_D^{\text{Mn}} \lesssim 0.3 \text{ eV}$ ,  $E_D^{\text{Sn}} \approx 0.4 \text{ eV}$ . The similar estimation of the diffusion barriers of In atoms cannot be derived from our data, since the simplified model is not consistent with observed unstable islands. The application of Tl passivating layer causes significant reduction of the diffusion barriers in comparison with the clean Si(111)-(7×7) surface ( $\approx 0.9 \text{ eV}$  [34,35]), which results in about nine-order increase of the diffusion constant  $D$  ( $D \propto \frac{\nu_0}{3} \exp(-E_D/kT)$ ). The estimated values of diffusion barriers on the Si(111) surface after the passivation fall into the range of the barriers determined for diffusion of metals on metal surfaces (Fe(100)/Fe - 0.45 eV [36], Ni(100)/Cu - 0.36 eV [30], Ag(100)/Ag - 0.40 eV [32], Pt(111)/Ag - 0.16 eV [37] etc.).

### 4. Summary

We investigated growth behavior of three elemental adsorbates: manganese, indium and tin on the thallium-passivated Si(111) surface. At submonolayer coverage (about 0.25 ML) and room temperature, the adsorbates exhibit diverse strength of adsorbate-adsorbate and substrate-adsorbate interactions, resulting in significantly different arrangements. Manganese creates highly-branched stable islands which are primarily nucleated on Si steps. The topography of Mn islands suggests that ordering of Mn atoms in the islands is only short-range. Indium creates more compact flat islands with height of one monolayer and without any apparent nucleation centers. The topography of In islands manifests a Moiré pattern (periodicity 1.76 nm), which indicates that the islands consist of periodically arranged In atoms (lattice constant 0.32 nm). Changes of shapes of In islands indicate relatively strong interaction between the STM tip and In atoms compared to

the bonding of In atoms to other atoms in In islands and the substrate. Tin forms an array of triangular objects, in which Sn and Tl atoms are probably intermixed, both in concentration of 1 ML. Energetic barriers for the diffusion of all studied adsorbates are strongly reduced compared to those on the initial  $(7 \times 7)$ -reconstructed Si(1 1 1) surface. Overall, the growth modes and the diffusion barriers of adsorbates on the Si(1 1 1)/Tl – (1 × 1) surface resemble those found on less reactive metal substrates. This shows that Tl can be used as a suitable passivation agent and a modifier of adsorbate growth on the Si(1 1 1) surface.

## References

- [1] M. Copel, M.C. Reuter, E. Kaxiras, R.M. Tromp, Surfactants in epitaxial growth, Phys. Rev. Lett. 63 (1989) 632–635, <http://dx.doi.org/10.1103/PhysRevLett.63.632>.
- [2] L. Vitali, F.P. Leisenberger, M.G. Ramsey, F.P. Netzer, Thallium overlayers on Si(1 1 1): structures of a “new” group III element, J. Vac. Sci. Technol. A: Vac. Surf. Films 17 (4) (1999) 1676, <http://dx.doi.org/10.1116/1.581871> <http://scitation.aip.org/content/avs/journal/jvsta/17/4/10.1116/1.581871>
- [3] K. Sakamoto, T. Oda, A. Kimura, K. Miyamoto, M. Tsujikawa, A. Imai, N. Ueno, H. Namatame, M. Taniguchi, P.E.J. Eriksson, R.I.G. Uhrberg, Abrupt rotation of the Rashba spin to the direction perpendicular to the surface, Phys. Rev. Lett. 102 (9) (2009) 096805, <http://dx.doi.org/10.1103/PhysRevLett.102.096805>.
- [4] S.S. Lee, H.J. Song, N.D. Kim, J.W. Chung, K. Kong, D. Ahn, H. Yi, B.D. Yu, H. Tochihara, Structural and electronic properties of thallium overlayers on the Si(1 1 1)-7 × 7 surface, Phys. Rev. B 66 (2002) 23312, <http://dx.doi.org/10.1103/PhysRevB.66.23312>.
- [5] L. Vitali, M. Ramsey, F. Netzer, Rotational epitaxy of a ‘soft’ metal overlayer on Si(1 1 1), Surf. Sci. 452 (1–3) (2000) L281–L286, [http://dx.doi.org/10.1016/S0039-6028\(00\)00367-8](http://dx.doi.org/10.1016/S0039-6028(00)00367-8) <http://linkinghub.elsevier.com/retrieve/pii/S0039602800003678>
- [6] K. Sakamoto, P.E.J. Eriksson, S. Mizuno, N. Ueno, H. Tochihara, R.I.G. Uhrberg, Core-level photoemission study of thallium adsorbed on a Si(1 1 1)-7 × 7 surface: valence state of thallium and the charge state of surface Si atoms, Phys. Rev. B 74 (7) (2006) 075335, <http://dx.doi.org/10.1103/PhysRevB.74.075335>.
- [7] P. Kocán, P. Sobotík, P. Matvija, M. Setvík, I. Oštádal, An STM study of desorption-induced thallium structures on the Si(1 1 1) surface, Surf. Sci. 606 (13–14) (2012) 991–995, <http://dx.doi.org/10.1016/j.susc.2011.12.016> <http://linkinghub.elsevier.com/retrieve/pii/S0039602811004973>
- [8] K. Yaji, Y. Ohtsubo, S. Hatta, H. Okuyama, K. Miyamoto, T. Okuda, A. Kimura, H. Namatame, M. Taniguchi, T. Aruga, Large Rashba spin splitting of a metallic surface-state band on a semiconductor surface, Nat. Commun. 1 (2) (2010) 17, <http://dx.doi.org/10.1038/ncomms1016> <http://www.nature.com/ncomms/journal/v1/n2/full/ncomms1016.html>
- [9] T. Noda, S. Mizuno, J. Chung, H. Tochihara, T<sub>4</sub> site adsorption of Tl atoms in a Si(1 1 1)-(1 × 1)-Tl structure, determined by low-energy electron diffraction analysis, Jpn. J. Appl. Phys. 42 (Part 2, No. 3B) (2003) L319–L321, <http://dx.doi.org/10.7567/JJAP.42.L319> <http://jap.jss.jp/link?JJAP/42/L319>
- [10] N. Kim, C. Hwang, J. Chung, J. Kim, H. Kim, D. Noh, Structural properties of a thallium-induced Si(1 1 1)-1 × 1 surface, Phys. Rev. B 69 (19) (2004) 195311, <http://dx.doi.org/10.1103/PhysRevB.69.195311>.
- [11] J. Ibanez Azpiroz, A. Eiguen, A. Bergara, Relativistic effects and fully spin-polarized Fermi surface at the Ti/Si(1 1 1) surface, Phys. Rev. B 84 (12) (2011) 125435, <http://dx.doi.org/10.1103/PhysRevB.84.125435>.
- [12] D.V. Gruznev, L.V. Bondarenko, A.V. Matetskiy, A.A. Yakovlev, A.Y. Tuchaya, S.V. Eremeev, E.V. Chulkov, J.-P. Chou, C.-M. Wei, M.-Y. Lai, Y.-L. Wang, A.V. Zотов, A.A. Saranin, A strategy to create spin-split metallic bands on silicon using a dense alloy layer, Sci. Rep. 4 (2014) 4742, <http://dx.doi.org/10.1038/srep04742> <http://www.nature.com/scientificreports/4/4742.html>
- [13] D. Gruznev, A. Zотов, A.A. Saranin, Tailoring of spin-split metallic surface-state bands on silicon, J. Electron Spectrosc. Relat. Phenom. (2014), <http://dx.doi.org/10.1016/j.elspec.2014.09.006>.
- [14] P. Kocán, P. Sobotík, I. Oštádal, Metallic-like thallium overlayer on a Si(1 1 1) surface, Phys. Rev. B 84 (23) (2011) 233304, <http://dx.doi.org/10.1103/PhysRevB.84.233304>.
- [15] K. Sakamoto, et al., Valley spin polarization by using the extraordinary Rashba effect on silicon, Nat. Commun. 4 (2013) 2073, <http://dx.doi.org/10.1038/ncomms3073> <http://www.nature.com/ncomms/2013/130628/ncomms3073/full/ncomms3073.html>
- [16] A. Kumar, M. Tallarida, M. Hansmann, U. Starke, K. Horn, Thin manganese films on Si(1 1 1)-7 × 7: electronic structure and strain in silicide formation, J. Phys. D: Appl. Phys. 37 (7) (2004) 1083–1090, <http://dx.doi.org/10.1088/0022-3727/37/7/021> <http://stacks.iop.org/0022-3727/37/7/021?key=crossref.02570be977ebc4aae7d4d87acd2a596>
- [17] S. Higashi, P. Kocán, H. Tochihara, Reactive epitaxial growth of MnSi ultra-thin films on Si(1 1 1) by Mn deposition, Phys. Rev. B 79 (2009) 205312, <http://dx.doi.org/10.1103/PhysRevB.79.205312>.
- [18] S. Ogura, K. Fukutani, M. Matsumoto, T. Okano, M. Okada, T. Kawamura, Dendritic to non-dendritic transitions in Au islands investigated by scanning tunneling microscopy and Monte Carlo simulations, Phys. Rev. B 73 (12) (2006) 125442, <http://dx.doi.org/10.1103/PhysRevB.73.125442>.
- [19] H. Brune, H. Röder, K. Bromann, K. Kern, J. Jacobsen, P. Stoltze, K. Jacobsen, J. Norskov, Anisotropic corner diffusion as origin for dendritic growth on hexagonal substrates, Surf. Sci. 349 (1) (1996) L115–L122, [http://dx.doi.org/10.1016/0039-6028\(95\)01347-4](http://dx.doi.org/10.1016/0039-6028(95)01347-4) <http://www.sciencedirect.com/science/article/pii/0039602895013474>
- [20] J. Zhong, T. Zhang, Z. Zhang, M. Lagally, Island-corner barrier effect in two-dimensional pattern formation at surfaces, Phys. Rev. B 63 (11) (2001) 113403, <http://dx.doi.org/10.1103/PhysRevB.63.113403>.
- [21] A.A. Saranin, A.V. Zотов, V.G. Kotlyar, I.A. Kuyanov, T.V. Kasyanova, A. Nishida, M. Kishida, Y. Murata, H. Okada, M. Katayama, K. Oura, Growth of thallium overlayers on a Si(1 0 0) surface, Phys. Rev. B 71 (2005) 035312, <http://dx.doi.org/10.1103/PhysRevB.71.035312>.
- [22] P. Kocán, P. Sobotík, I. Oštádal, J. Javoršký, M. Setvík, Stability of In rows on Si(1 0 0) during STM observation, Surf. Sci. 601 (18) (2007) 4506–4509, <http://dx.doi.org/10.1016/j.susc.2007.04.132> <http://linkinghub.elsevier.com/retrieve/pii/S0039602807004670>
- [23] A.A. Saranin, T. Numata, O. Kubo, H. Tani, M. Katayama, V.G. Lifshits, K. Oura, STM tip-induced diffusion of In atoms on the Si(1 1 1) $\sqrt{3} \times \sqrt{3}$ -In surface, Phys. Rev. B 56 (1997) 7449–7454, <http://dx.doi.org/10.1103/PhysRevB.56.7449>.
- [24] R.Q. Hwang, Nucleation and growth of thin metal films on clean and modified metal substrates studied by scanning tunneling microscopy, J. Vac. Sci. Technol. A: Vac. Surf. Films 10 (4) (1992) 1970, <http://dx.doi.org/10.1116/1.578012> <http://scitation.aip.org/content/avs/journal/jvsta/10/4/10.1116/1.578012>
- [25] S. Kodambaka, D.L. Chopp, I. Petrov, J. Greene, Coalescence kinetics of two-dimensional TiN islands on atomically smooth TiN(0 0 1) and TiN(1 1 1) terraces, Surf. Sci. 540 (2–3) (2003) L611–L616, [http://dx.doi.org/10.1016/S0039-6028\(03\)00846-X](http://dx.doi.org/10.1016/S0039-6028(03)00846-X) <http://linkinghub.elsevier.com/retrieve/pii/S003960280300846X>
- [26] A. Rodriguez-Prieto, D.R. Bowler, Ab initio study of subsurface diffusion of Cu on the H-passivated Si(0 0 1) surface, Phys. Rev. B 80 (2009) 155426, <http://dx.doi.org/10.1103/PhysRevB.80.155426>.
- [27] A.F. Lee, K. Wilson, R.M. Lambert, Structure and stability of the platinum/aluminum interface: alloying and substrate vacancy formation on Pt(1 1 1)/Al, Surf. Sci. 446 (1–2) (2000) 145–152, [http://dx.doi.org/10.1016/S0039-6028\(99\)01145-0](http://dx.doi.org/10.1016/S0039-6028(99)01145-0) <http://linkinghub.elsevier.com/retrieve/pii/S0039602899011450>
- [28] C. Gunther, S. Gunther, E. Kopatzki, R. Hwang, J. Schroder, J. Vrijmoeth, R. Behm, Microscopic aspects of thin metal-film epitaxial growth on metallic substrates, Ber. Bunsen-Ges. - Phys. Chem. Phys. 97 (1993) 522–536.
- [29] H. Brune, Microscopic view of epitaxial metal growth: nucleation and aggregation, Surf. Sci. Rep. 31 (3–4) (1998) 125–229, [http://dx.doi.org/10.1016/S0167-5279\(97\)00015-0](http://dx.doi.org/10.1016/S0167-5279(97)00015-0) <http://linkinghub.elsevier.com/retrieve/pii/S0167527997000150>
- [30] B. Müller, L. Nedelmann, B. Fischer, H. Brune, K. Kern, Initial stages of Cu epitaxy on Ni(1 0 0): postnucleation and a well-defined transition in critical island size., Phys. Rev. B Condens. Matter 54 (24) (1996) 17858–17865, URL: <http://journals.aps.org/prb/abstract/10.1103/PhysRevB.54.17858>.
- [31] J.A. Venables, G.D.T. Spiller, M. Hanbucken, Nucleation and growth of thin films, Rep. Prog. Phys. 47 (1984) 399–459, <http://iopscience.iop.org/0034-4885/47/4/002>
- [32] C. Zhang, M.C. Bartelt, J. Wen, C.J. Jenkins, J.W. Evans, P.A. T. The initial stages of Ag(1 0 0) homoepitaxy: scanning tunneling microscopy experiments and Monte Carlo simulations, J. Cryst. Growth 174 (1997) 851–857 <http://www.sciencedirect.com/science/article/pii/S002204897000638>
- [33] M. Bott, M. Hohage, M. Morgenstern, T. Michely, G. Comsa, New approach for determination of diffusion parameters of adatoms, Phys. Rev. Lett. 76 (8) (1996) 1304–1307, URL: <http://journals.aps.org/prl/abstract/10.1103/PhysRevLett.76.1304>.
- [34] P. Sobotík, P. Kocán, I. Oštádal, Direct observation of Ag intercell hopping on the Si(1 1 1)-(7 × 7) surface, Surf. Sci. 537 (1–3) (2003) L442–L446, [http://dx.doi.org/10.1016/S0039-6028\(03\)00608-3](http://dx.doi.org/10.1016/S0039-6028(03)00608-3) <http://www.sciencedirect.com/science/article/pii/S0039602803006083>
- [35] H. Jeong, S. Jeong, Diffusion of Ag adatom on the H-terminated and clean Si(1 1 1) surfaces: a first-principles study, Phys. Rev. B 71 (3) (2005) 035310, <http://dx.doi.org/10.1103/PhysRevB.71.035310>.
- [36] J. Strosio, D. Pierce, R. Dragoset, Homoepitaxial growth of iron and a real space view of reflection-high-energy-electron diffraction., Phys. Rev. Lett. 70 (23) (1993) 3615–3618, URL: <http://journals.aps.org/prl/abstract/10.1103/PhysRevLett.70.3615>.
- [37] H. Brune, H. Röder, C. Boragno, K. Kern, Microscopic view of nucleation on surfaces, Phys. Rev. Lett. 73 (14) (1994) 1955–1958, URL: <http://journals.aps.org/prl/abstract/10.1103/PhysRevLett.73.1955>.

## 5.2 Thallium-mediated growth of Si-metal surface reconstructions

Another unique property of Tl atoms is their extraordinarily low desorption temperature from the Si(111) surface. The Tl – (1 × 1) layer forms at  $\approx 300^\circ\text{C}$  and Tl atoms start to desorb just above this temperature, at  $\approx 330^\circ\text{C}$ . After the desorption, Tl atoms leave the Si-(1 × 1) termination exposed. The termination, containing dangling bonds, is reactive and tends to reconstruct into energetically more favorable structures. When only Tl and Si atoms are present on the surface, this leads to formation of the SiTl- $(\sqrt{3} \times \sqrt{3})$  mosaic reconstruction (paper IV, page 45).

If we deposit an adsorbate onto the Tl – (1 × 1) layer and heat it to  $\approx 330^\circ\text{C}$ , the adsorbate substitutes Tl or Si in the surface reconstructions (Fig. 5.1a-e). After desorption of all Tl atoms (at  $\approx 360^\circ\text{C}$ ), Si-adsorbate reconstructions emerge on the surface (Fig. 5.1f). Hereafter we will refer to this method of preparation of Si-adsorbate reconstructions as the Tl-mediated growth. In this section we compare Si-metal reconstructions prepared by the Tl-mediated growth with Si-metal reconstructions prepared by the direct deposition to the Si(111) – (7 × 7) surface and annealing at the temperature  $\approx 360^\circ\text{C}$  (see Fig. 5.1g-h). We show that the Tl layer can have a catalyzing effect on the formation of thermally induced Si-metal reconstructions.

After a direct deposition, three adsorbates of our interest behave as follows. Below  $\approx 260^\circ\text{C}$  Mn forms clusters on top of the (7 × 7) reconstruction of the Si(111) surface [87]. Above this temperature, Mn atoms react with Si substrate to form manganese-silicide islands of three types: tabular, 3D and elongated [87]. The elongated islands evolve into MnSi nanowires at a temperature above  $\approx 500^\circ\text{C}$  [88]. The other two studied systems, the Si(111)/In and the Si(111)/Sn surfaces, are typical for a wide variety of thermally induced reconstructions on the Si(111) substrate (see phase diagrams in [89] and [90]). Both In and Sn incorporate into the (7 × 7) reconstruction at the temperature below 350 °C and the coverage below 0.25 ML. At a higher temperature and coverage,  $(\sqrt{3} \times \sqrt{3})$ , (1 × 1) and  $(2\sqrt{3} \times 2\sqrt{3})$  phases emerge on the surfaces. High temperature is necessary for canceling the original (7 × 7) reconstruction, which is complex and stable up to  $\approx 900^\circ\text{C}$  without the presence of a metal adsorbate.

Our method of growing Si-metal reconstructions at lower temperature consists of three steps. First, prepare the Si(111)/Tl – (1 × 1) surface and deposit a desired amount of an adsorbate. Then anneal the surface at  $\approx 360^\circ\text{C}$ . The annealing induces desorption of Tl atoms, exposes the underlying Si-(1 × 1) termination of the surface and enables the adsorbate to react directly with Si dangling bonds (see Fig. 5.1).

The first adsorbate, manganese, directly deposited on the Si(111) surface, forms 2D and 3D MnSi islands with average density of  $(7 \pm 2) \times 10^{-3} \text{ nm}^{-2}$  (the left column of Fig. 5.2). Silicon atoms incorporated into the islands at  $\approx 280^\circ\text{C}$  are taken from the vicinity of the islands, leaving holes in the originally flat surface. The holes are evenly distributed on the surface. After the Tl-mediated growth (the right column of Fig. 5.2), density of islands decreases to  $(2.3 \pm 0.5) \times 10^{-4} \text{ nm}^{-2}$ . The surface contains bigger and more compact holes compared to the direct deposition. In addition to 2D and 3D islands, MnSi nanowires are observed on the surface. According to the literature, the nanowires are expected to emerge on the surface at a higher temperature of  $\approx 500^\circ\text{C}$  [88].

In the case of indium, we observe only subtle differences between the results of

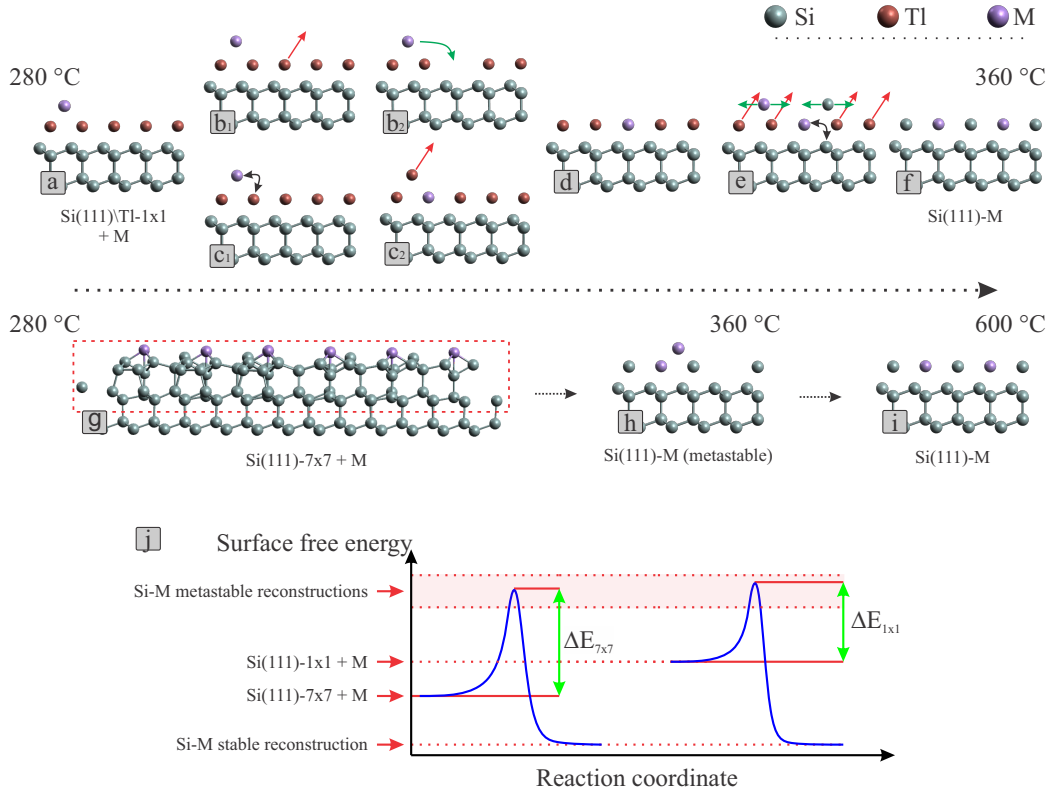


Fig. 5.1: Comparison of the Tl-mediated (a-f) and direct (g-i) growth of Si-metal reconstructions on the Si(111) surface. j: reaction coordinates of the two processes. Letter M denotes a metal adsorbate in all images. Red, green and black arrows denote desorption, diffusion and substitution, respectively.

a direct and Tl-mediated growth. Both preparation methods produce SiIn-( $\sqrt{3} \times \sqrt{3}$ ) mosaic reconstruction with similar number of defects. The similarity is not true in the case of Sn. While a direct deposition of Sn leads to the surface covered partially by the Sn-( $\sqrt{3} \times \sqrt{3}$ ) reconstruction and partially by the Si(111) – ( $7 \times 7$ ) reconstruction with Si adatoms substituted by Sn, the Tl-mediated deposition produces the surface fully covered by the ( $\sqrt{3} \times \sqrt{3}$ ) mosaic reconstruction.

Two main conclusions follow from the observations. First, the Tl-mediated growth can facilitate formation of thermally induced metal-Si reconstructions by canceling the original Si-( $7 \times 7$ ) reconstruction and replacing it by the less stable ( $1 \times 1$ ) termination of the surface (see Fig. 5.1j). Secondly, the Tl passivation layer increases the mobility of metal atoms compared to the bare Si(111) surface. The increased mobility causes growth of larger and more compact island structures on the surface. The catalyzing effect of the Tl – ( $1 \times 1$ ) layer can be used in situations when a metal-Si reconstruction needs to be prepared on a surface that already contains thermally sensitive structures.

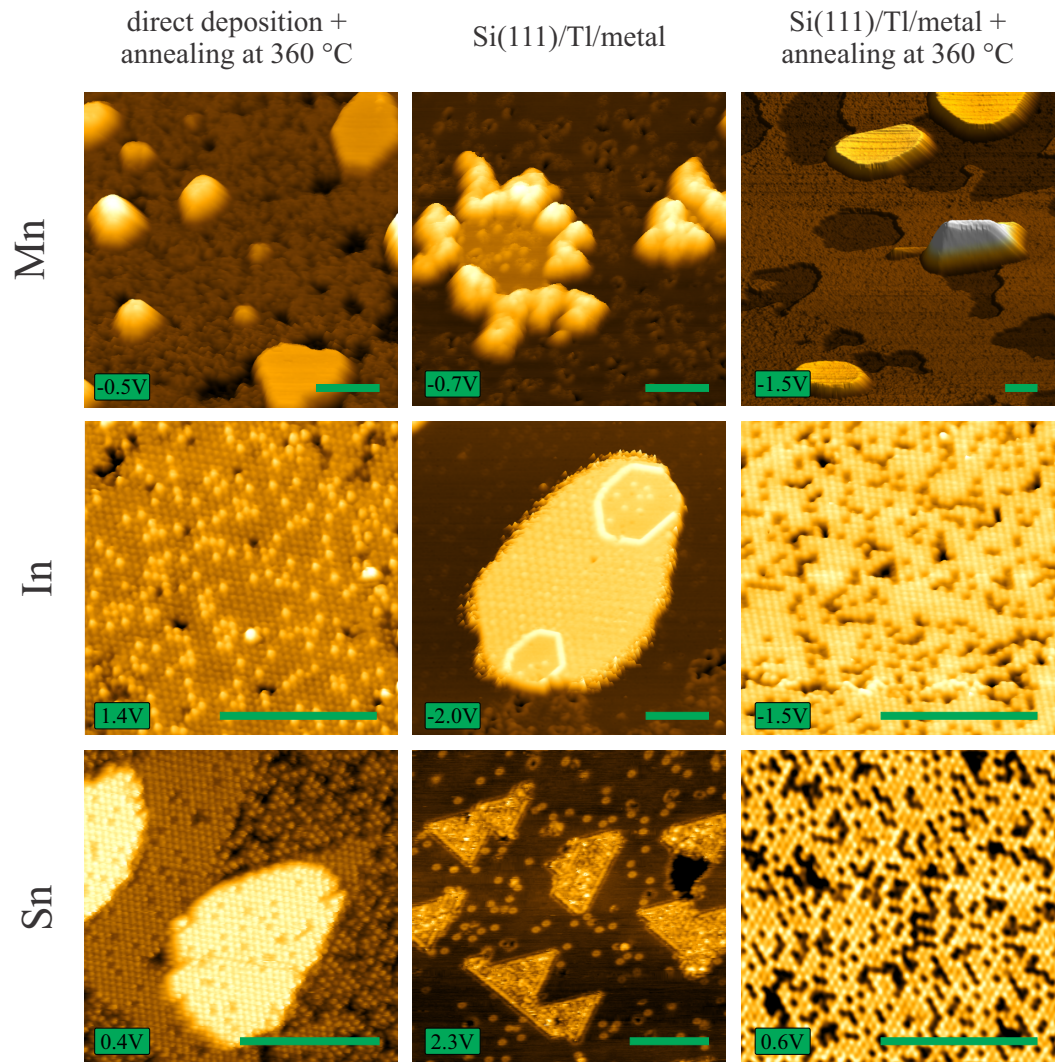


Fig. 5.2: Comparison of the Si(111)/M surfaces ( $M = \text{Mn, In, Sn}$ ) prepared by a direct deposition and annealing at  $\approx 360^\circ\text{C}$  with the surface prepared by a deposition onto the Si(111)/Tl –  $(1 \times 1)$  surface and annealing at the same temperature. Green rectangles denote the length of 10 nm. The scanning sample voltage is indicated in all images.

# 6. Organic molecules on the Si(111)/Tl-(1 × 1)

In previous chapters, we tested that the Si(111)/Tl – (1 × 1) surface is chemically stable enough to sustain adsorption of reactive adsorbates. We showed that single-atom adsorbates are mobile on the surface and tend to form bigger and more compact island structures. These two properties resemble properties of metal surfaces, on which organic molecules are able to diffuse and self-organize. In this chapter we address the question of self-assembly of organic molecules on the Tl-passivated Si(111) surface by studying behavior of two technologically important molecules: copper phthalocyanine (CuPc) and copper hexadecafluoro-phthalocyanine ( $F_{16}CuPc$ ) (see structural models in Fig. 6.1). Our results show that in addition to static self-assembled structures these molecules form dynamic structures that we are able to not only visualize, but also control by the STM.

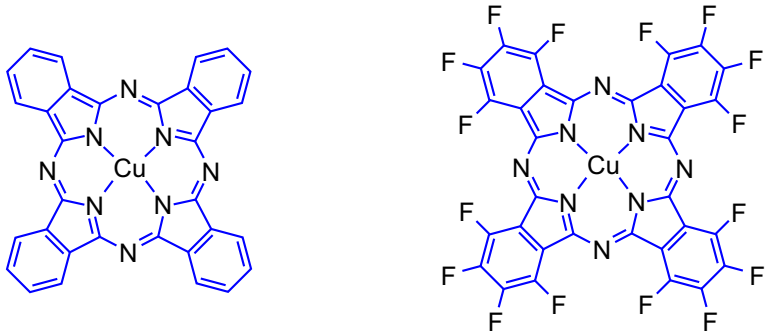


Fig. 6.1: Structural models of CuPc (left) and  $F_{16}CuPc$  (right) molecules.

## 6.1 Phthalocyanines

The phthalocyanines are a group of synthetic compounds that contain four isoindole units linked together in a macrocyclic ring. The first phthalocyanine was synthesized in 1907 [91]. Metal-coordinated phthalocyanines came by chance 20 years later after accidental use of a metal reaction vessels [92, 93]. The obtained metal-phthalocyanines were isolated and identified in 1934 [92]. Since then phthalocyanines have become widely used in dyes and pigments and more recently in molecular-electronic devices such as organic solar cells and organic field-effect transistors [94, 95]. Due to (i) their structural analogy to natural pigments such as the porphyrins, (ii) outstanding chemical stability to light and temperature and (iii) versatile electronic properties that can be tuned by substitution of central metal atom or by substitution of lateral hydrogen atoms, they are often used in academic research as building blocks of self-assembled molecular structures.

On solid/vacuum interfaces, phthalocyanines generally adsorb with the molecular plane parallel to the surface and often form long-range ordered structures at monolayer coverage. In the submonolayer regime, the tendency to form densely-packed structured depends on the balance between attractive and repulsive intermolecular forces. Attractive forces result mostly from van der Waals interactions or hydrogen bonds. The latter ones are important especially in the case of halogenated phthalocyanines such as F<sub>16</sub>CuPc. In general, attractive intermolecular interactions prevail when the adsorbate-substrate interaction is weak [21]. In contrast, strong interactions are usually accompanied by an adsorbate-substrate charge transfer. The transfer results in net dipole moments connected to adsorbed molecules. The dipole moments are parallel to each other and cause repulsion between the molecules.

In the last decades, an extensive effort was dedicated to the studies of phthalocyanines adsorbed on various substrates. Since providing a comprehensive overview of the large amount of phthalocyanine-related information available in the literature is out of scope of this thesis, we focus the readers attention to existing review papers of Gottfried [21], Otsuki [96], Drain et al. [97] and others [98–100].

## 6.2 Direct observation of a 2D molecular gas on the Si(111)/Tl-(1 × 1)

The first molecule we address in this thesis is the F<sub>16</sub>CuPc molecule. Upon deposition on the (1 × 1)-reconstructed Tl layer F<sub>16</sub>CuPc molecules adsorb in a flat-lying position with the main molecular plane parallel to the surface. At the room temperature, molecules have enough thermal energy to overcome shallow diffusion barriers and therefore they move almost freely along a defect-free surface. On the other hand, defected parts of the surface are more reactive and form covalent bonds with F<sub>16</sub>CuPc molecules. In the STM, only the static molecules can be directly visualized. Mobile molecules, which are not covalently bonded to the substrate, form a 2D gas. Direct imaging of individual gas molecules is not possible because their surface diffusion is much faster than the speed of the STM feedback loop.

2D surface gases are often observed on nonreactive surfaces such as Ag(111) [101, 102], Ag(110) [103], Au(111) [104, 105], Cu(111) [106]. In general, methods of observing the 2D gases fall into five categories:

- (a) cooling down a surface in order to slow down the molecular diffusion (individual molecules are imaged by SPM techniques) [103]
- (b) observation of a 2D-gas-solid interaction in the vicinity of step edges or a condensed phase (imaged by SPM techniques) [101, 106]
- (c) imaging a surface with an SPM probe affected by individual gas molecules [103]
- (d) detecting a presence of a 2D gas on a surface by an increase in the noise of the signal that is utilized in an SPM [101, 104, 105]
- (e) determination of the radial distribution function of a 2D gas by diffraction techniques [102]

The SPM techniques either rely on slowing down of the diffusing molecules (a-c), or they detect the presence of a 2D gas without a further characterization of its properties (d). However, slowing down the molecules by cooling down the surface, by interaction with step edges, or by interaction with SPM probe inevitably changes the state of a gas. Diffraction methods do not significantly influence the state, but provide only reciprocal space images of a 2D gas. These images correspond to the space-averaged and time-averaged relative positions of all molecules in a diffraction volume during the image acquisition. Because of the space averaging, the information included in diffraction images does not reflect local changes in the properties of a 2D gas that can occur on real surfaces with defects and step edges. On the other hand, time averaging and rotation of gas molecules results in circularly symmetric diffraction images. Such images do not reflect the effect of a lower molecular symmetry on the distribution of molecules on a surface.

In the paper II (page 65), we propose a novel approach of visualizing 2D surface gases by means of STM. In the approach, we use the fact that even though positions of individual molecules in a gas are random, positions of the gas molecules are correlated to its close neighbors. From a perspective of a mobile reference gas molecule, the correlation means that the probability of finding another molecule in its vicinity varies with the distance  $r$  and the direction  $\phi$ . On an ideal defect-free surface, all molecules would be mobile and all positions on the surface would have the same probability  $p_m(x, y)$  to be occupied by a molecule. In other words, the local time-averaged density of molecules  $n(x, y)$  would be constant on such a surface. On a real surface, defects and static molecules adsorbed on the defects represent surface points that are forbidden for mobile molecules. This disrupts the constancy of  $p_m(x, y)$  and induces corrugations of  $n(x, y)$  in the vicinity of the static objects on a surface. We use STM to image the molecular density corrugations and we use KMC simulations to show that the origin of the corrugations is the correlated motion of the molecules in a 2D gas. Importantly, we also apply the approach to visualize  $n(x, y)$  in the vicinity of fixed molecules bonded to defects. This case is of special significance since  $n(x, y)$  in the vicinity of a fixed reference molecule directly represents a pair correlation function of a 2D gas. A direct measurement of the pair correlation function was not achieved by any other method up to now.

My contribution to the paper II can be summarized as follows. I obtained all experimental data presented in the paper. During the first experiments with the Si(111)/Tl – (1 × 1)/F<sub>16</sub>CuPc system, I discovered that F<sub>16</sub>CuPc molecules form a 2D gas on the surface and that the 2D gas can be visualized by STM. To explain complex structures observed on the surface, I carried out a series of experiments with a different molecular coverage (see Figs. 2, 3 and 4 in the paper II). These experiments led to the identification of different static and dynamic adsorption configurations of F<sub>16</sub>CuPc molecules and to the explanation of the observed surface corrugations as the corrugations of  $n(x, y)$ . I prepared the data for publication. With the help of co-authors, I wrote the manuscript.

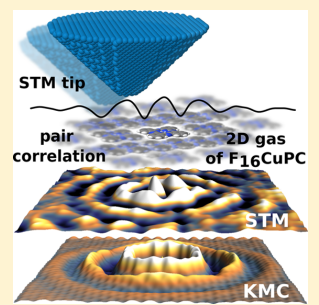
## Pair Correlation Function of a 2D Molecular Gas Directly Visualized by Scanning Tunneling Microscopy

P. Matvija,<sup>①</sup> F. Rozbořil, P. Sobotík, I. Ošťádal, and P. Kocán<sup>\*②</sup>

Faculty of Mathematics and Physics, Department of Surface and Plasma Science, Charles University, V Holešovičkách 2, 180 00 Prague, Czech Republic

 Supporting Information

**ABSTRACT:** The state of matter in fluid phases, determined by the interactions between particles, can be characterized by a pair correlation function (PCF). At the nanoscale, the PCF has been so far obtained experimentally only by means of reciprocal-space techniques. We use scanning tunneling microscopy (STM) at room temperature in combination with lattice-gas kinetic Monte Carlo (KMC) simulations to study a two-dimensional gas of highly mobile molecules of fluorinated copper phthalocyanine on a Si(111)/Tl-(1×1) surface. A relatively slow mechanism of STM image acquisition results in time-averaging of molecular occurrence under the STM tip. We prove by the KMC simulations that in the proximity of fixed molecules STM images represent the PCF. We demonstrate that STM is capable of visualizing directly the pair correlation function in real space.



Atoms or molecules adsorbed on weakly interacting surfaces at noncryogenic temperatures are often observed in the form of a 2D surface gas.<sup>1–6</sup> Within the lattice-gas model, a surface is represented by a periodic lattice of adsorption positions separated by low energy barriers allowing migration of the molecules. The position of a molecule in the lattice-gas is random but correlated in relation to its close neighbors. In a system of many particles, the correlation is usually expressed by a pair correlation function (PCF).<sup>7</sup> It is defined as an ensemble-averaged particle density at a given position relative to a reference molecule. The PCF reflects complex interactions between molecules, and thus, its knowledge is crucial, for example, for controlled growth of organic semiconductor devices. In general, the PCF can be decomposed into the radial part (i.e., the radial distribution function) and the angular part. The radial part can be experimentally determined indirectly by various diffraction methods;<sup>8–11</sup> however, such results are nonlocal and suffer from numerical errors (e.g., Fourier termination errors).<sup>9,10</sup> The angular part of the PCF can be partly reconstructed from diffraction data, but only for simple molecules.<sup>8,12</sup> All of these limitations are principally caused by the fact that the PCF was visualized at the atomic scale so far only by means of reciprocal-space techniques.

The imaging speed of scanning tunneling microscopy (STM) is relatively slow in comparison with molecular motion, and even “video-rate” imaging<sup>13</sup> is not sufficient to record fast surface processes in detail. Lowering the temperature reduces the rate of thermally activated processes but observation of some kinetic aspects may become impossible due to limited surface mobility. Recording of processes much faster than STM data acquisition produces images containing time-averaged traces of the processes, such as in the case of Si dimer flip-flop

motion<sup>14</sup> or fast diffusion of Ag atoms on the Si(111)-(7×7) surface.<sup>15</sup>

In STM, an acquisition time for each pixel of topography or current images is typically in the order of milliseconds. It results in time-averaging of all faster surface processes.<sup>14,15</sup> In the case of a 2D molecular gas, each molecule passing under the tip (with fixed  $z$  position) temporarily increases the tunneling current. Because many molecules are passing under the tip during the acquisition of one data point, the measured tunneling current can be expressed as  $I_t = p_m I_m + (1 - p_m) I_s$ , where  $p_m$  is the probability of finding a molecule under the tip and  $I_t$  and  $I_m$  are tunneling currents corresponding to the bare substrate and the substrate with a molecule, respectively. The probability  $p_m$  can be expressed in terms of the local time-averaged surface density of molecules  $n(x,y)$  as  $p_m = n(x,y)/\theta_S$ , where  $\theta_S$  is the molecular concentration on the surface fully covered by one layer of molecules (hereafter monolayer, ML). Therefore, measured changes of the tunneling current are

$$I_t(x, y) - I_s = \frac{n(x, y)}{\theta_S} (I_m - I_s) \quad (1)$$

In the regime of the constant tunneling current stabilized by adjusting the  $z$  position of the tip, the change of  $z$  is proportional to  $n(x,y)$  as well, within the first-order approximation for small changes of the current. The relations imply that the STM images on an atomically smooth substrate covered by a 2D gas reflect local differences in  $n(x,y)$ . This

**Received:** July 28, 2017

**Accepted:** August 23, 2017

**Published:** August 23, 2017

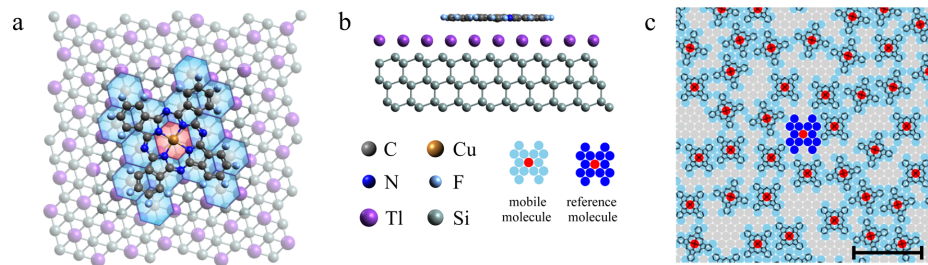


**Figure 1.** (a) Top view of the structural model of the Si(111)/Tl-(1x1) surface and an adsorbed F<sub>16</sub>CuPc molecule. Unit cell areas occupied by the molecule on the nondefected surface are marked by hexagons. The same hexagonal cells are used as a lattice basis in the Monte Carlo simulations (panel c). (b) Side view of the structural model. (c) Snapshot of a KMC simulation,  $\theta = 0.62$  ML. The fixed reference molecule is shown in dark blue, and mobile molecules of the 2D gas are shown in light blue. The scale bar is 3 nm long.

makes STM an excellent method for probing the local time-averaged surface concentration of molecules.

As a model system of a 2D gas, we use fluorinated copper phthalocyanine molecules (F<sub>16</sub>CuPc) deposited on the Si(111)/Tl-(1x1) surface. The Tl-(1x1) surface is atomically smooth,<sup>16–18</sup> unreactive for adsorbates and enables almost free and fast diffusion of F<sub>16</sub>CuPc molecules.<sup>16</sup> Like on other surfaces,<sup>4,19–25</sup> these planar molecules adsorb in a flat-lying configuration (see Figure 1a,b) and interact with the surface mostly by van der Waals forces.<sup>19</sup> The only reactive sites for F<sub>16</sub>CuPc molecules are defects commonly present on the surface (Figure 2a).<sup>26</sup> An STM image of molecules attached to the defects is displayed in Figure 2b. The image shows that the molecules attach to the defects by one lobe, while three lobes lie flat on the Tl-(1x1) substrate. After saturation of all reactive defects, the residual molecules form a 2D gas of highly mobile molecules. STM imaging of the gas is clarified by the height profile in Figure 2b. The profile crosses the Tl-(1x1) molecule adsorbed on a point defect (the highest and the lowest points of the profile). The area corresponding to the second lowest minimum in the profile forms the dark envelope surrounding the unbound lobes. It can be explained as the level of the bare Tl-(1x1) layer with low density of the 2D gas because of the repulsive interaction between F atoms of the static molecule and mobile 2D gas molecules. The remaining level in the profile corresponds to nonzero density of the 2D gas. Its height, between the level of Tl-(1x1) and the level of fixed molecules, agrees well with the value expected from eq 1 for the surface coverage of approximately 0.4 ML.

As can be seen from the profile, the 2D gas level is slightly corrugated, especially near the fixed molecule (see the gray arrows in Figure 2b). A size and a position of the brighter area near the fixed molecule does not correspond to the bright ring surrounding defects (see Figure 2a); therefore, the corrugation cannot be explained by interaction of molecules with electronic states of the substrate. The corrugation arises due to the correlation of molecules in the 2D gas. In defect-free Tl-(1x1) areas, time-averaging results in the constant density of molecules. Surface defects affect the motion of molecules and influence the probability  $p_m$ . As a result, the constancy of the local density of the gas is broken in the vicinity of defects. At low coverage up to  $\sim 0.3$  ML,  $n(x,y)$  is notably corrugated only in the closest vicinity of the defects. Surfaces with molecular coverage close to full monolayer are imaged with a strong corrugation of  $n(x,y)$  on the whole surface (see Figure 2c).

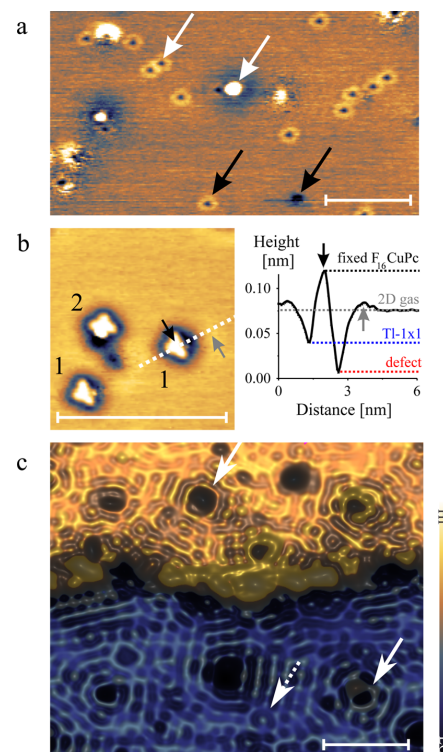


**Figure 2.** Adsorption of F<sub>16</sub>CuPc molecules on the Si(111)/Tl-(1x1) surface. (a) Si(111)/Tl-(1x1) surface before the deposition of molecules. Different kinds of point (black) and more complex (white) surface defects are marked by arrows. (b) Defect-stabilized F<sub>16</sub>CuPc molecules surrounded by the 2D molecular gas and an STM height profile over one of the static molecules. The dotted line marks the position in the image from which the profile was extracted. (c) Pseudo-3D view of the surface topography after deposition of 0.9 ML of F<sub>16</sub>CuPc molecules. Solid and dotted arrows mark different defect sites interacting with F<sub>16</sub>CuPc molecules. Scale bars are 10 nm long in all images.

To explain the complex maps of  $n(x,y)$  and its dependence on the total coverage, we executed the lattice-gas kinetic Monte Carlo (KMC) simulations. In the simulations, each molecule is

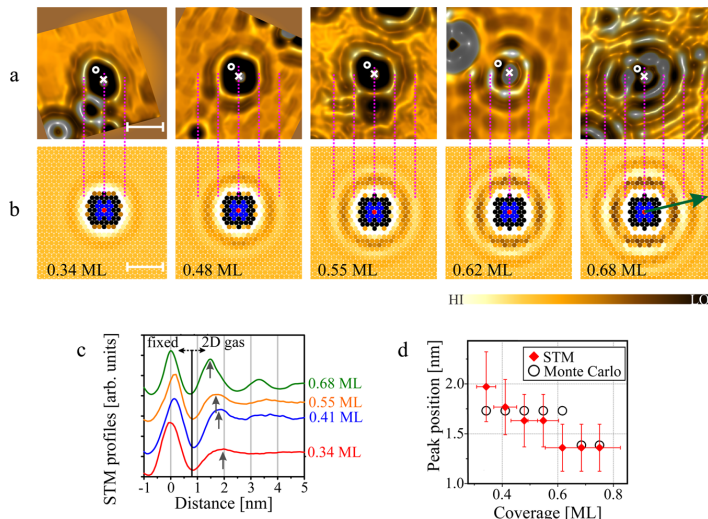


**Figure 3.** Time-averaged density of molecules in the vicinity of a fixed  $\text{F}_{16}\text{CuPc}$  molecule. (a) Pseudo-3D view of the STM topography images of  $n(x,y)$  near immobile molecules adsorbed on a defect. White crosses and circles indicate positions of centers of the molecules and the neighboring point defects, respectively. (b) Corresponding KMC simulated images of  $n(x,y)$  near the fixed molecule (same color coding as that in the STM images). Scale bars are 3 nm long in all images. (c) Profiles of the STM-measured  $n(x,y)$  in the vicinity of immobile  $\text{F}_{16}\text{CuPc}$  molecules. The direction of the profile is marked by an arrow in panel (b). (d) Positions of the first maxima in the  $n(x,y)$  profiles as a function of the coverage (the positions are marked by gray arrows in panel c).

represented by 15 lattice points that correspond to the real shape of  $\text{F}_{16}\text{CuPc}$  molecules, as shown in Figure 1a. Each lattice point is either occupied by a molecule or vacant (see Figure 1c). To simulate the steric repulsion, molecules can shift or rotate on the surface with a probability depending on the overlap of the molecules (double-occupied points). No other interaction is included in the simulation (but there is no limitation to implement any other kind of interaction). Maps of the molecular density  $n(x,y)$  are obtained by time-averaging occupancy of each lattice point. Details about KMC simulations are provided in the Supporting Information.<sup>27</sup>

The comparison of KMC simulations with STM data unveiled that the complex maps of  $n(x,y)$  can be explained as a result of 2D gas interactions with a few types of static  $\text{F}_{16}\text{CuPc}$  adsorption configurations and with surface defects. In the most common configuration (Figure 2b-1), three lobes of an  $\text{F}_{16}\text{CuPc}$  molecule are only weakly affected by the bond between the molecule and the defect. The interaction of the free lobes with molecules of the 2D gas is therefore similar to the  $\text{F}_{16}\text{CuPc}-\text{F}_{16}\text{CuPc}$  interaction in the gas. The particular case of the single fixed molecule is of special importance. The reason follows from the fact that the PCF is defined as an average density of molecules referenced to the position of a selected molecule. In the case of the  $\text{F}_{16}\text{CuPc}$  gas on the  $\text{Ti}(1\times 1)$  surface, the fixed molecules immobilized on defects can be used as the selected one. This means that the molecular density surrounding the fixed molecules corresponds to the PCF of the gas.

In the KMC simulations, we represent the configuration in Figure 2b-1 by fixing the position of a selected molecule while enabling the motion of others. A comparison of the KMC-calculated coverage-dependent  $n(x,y)$  in the proximity of the fixed molecule with the corresponding STM images is presented in Figure 3a,b. At coverage  $\theta \approx 0.34$  ML, the

simulation successfully reproduces the dark  $\text{Ti}(1\times 1)$  region surrounding the fixed molecule, the bright circular shell surrounding the dark region, and the constant character of  $n(x,y)$  further from the molecule. At higher coverage, both simulation and STM data show the evolution of further circular shells with alternating brightness, that is, the regions with an alternating value of local density of molecules. In the radial direction, an increase in coverage induces higher contrast and compression of inner-shell corrugations (see Figure 3c,d). The same evolution has been reported for the radial distribution function of 2D gases examined by diffraction.<sup>4</sup>

In contrast to the diffraction experiments, STM also offers a possibility to measure directly the angular part of the PCF. The angular dependence is the most pronounced in the “circular” shells, especially the inner shells at a high surface coverage (see Figure 3a with  $\theta > 0.5$  ML). KMC simulations revealed that maxima of the shells can be assigned to positions of the molecules in the close-packed domains containing the fixed molecules (for details, see the Supporting Information<sup>27</sup>). Visualization of the angular part of the PCF is clearly demonstrated in Figure 3a, even though an exact match of the simulated maxima within the shells with the experiment is not possible mainly due to asymmetry of the molecule stabilized by the defect, which is not considered in the simulation.

The influence of other defects on  $n(x,y)$  is further shown in Figure 4. Figure 4a depicts a pattern often observed at higher coverage (dotted arrow in Figure 2c). In this case, no fixed lobes are observed and the object has almost perfect circular symmetry. In the KMC simulations (Figure 4b), we successfully reproduced the STM image by substituting the fixed molecule with a rotating molecule bound to the surface by its central part. Another type of surface defect is a step edge, which naturally represents a nonreactive boundary influencing the 2D

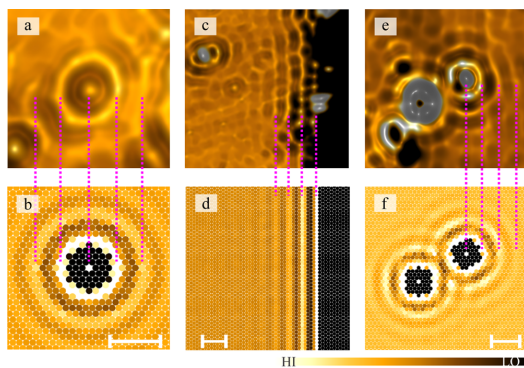


**Figure 4.** Comparison of the STM measurements and Monte Carlo simulations in special cases. Measured (top) and computed (bottom) maps of  $n(x,y)$  in the vicinity of a rotating molecule on a reactive point defect (0.68 ML) (a,b), a step edge (0.68 ML) (c,d), and two close immobile molecules (0.62 ML) (e,f). Scale bars are 3 nm long in all images.

gas. The STM image of the 2D gas on the upper terrace near a step edge and the corresponding simulation is shown in Figure 4c,d. The row of molecules nearest to the step edge is divided into dots due to the irregular shape of the edge in Figure 4c, which is not included in the simulation, but the formation of parallel wave-like corrugation is evident. More complex patterns can be explained by combining the influence of two or more defects. As a result, complex interference-like patterns can be observed (Figure 4e,f). The interference-like patterns can be also rationalized by possible layouts of individual molecules with respect to the surface defects (for details, see the Supporting Information<sup>27</sup>).

The excellent qualitative agreement between the STM-measured and KMC-simulated  $n(x,y)$  has been achieved by taking into account solely the geometry of the substrate and molecules. The only interaction used in the model is the steric short-range repulsion of the molecules. Thanks to the agreement, we can conclude that the long-range interaction is negligible and does not significantly affect the distribution of the molecules on the surface. In addition, quantitative analysis of the PCF can provide further details on the state of 2D gas. Individual properties of the molecules, such as the effective intermolecular potential, can be derived from the measured PCF by iterative Monte Carlo simulations.<sup>28</sup> Integral gas properties like pressure, compressibility, or total potential energy can be then determined directly from the PCF and the intermolecular potential.<sup>7</sup>

The new method allowed observation of the PCF in real space with molecular resolution. STM images of the 2D molecular gas interacting with immobile molecules reflect directly intermolecular interactions. By tuning temperature it is possible to activate kinetic processes reflecting specific interactions. The only fundamental limitation of the method is a sufficient mobility of the molecules within the 2D gas in order to allow time-averaging of their occurrence by STM. The broadly used experimental technique of STM and the relatively straightforward interpretation of the measured data promise wide applicability of the method in a variety of systems including, for example, functionalized organic molecules or complex hetero-organic adsorbates.

## ASSOCIATED CONTENT

### Supporting Information

The Supporting Information is available free of charge on the ACS Publications website at DOI: 10.1021/acs.jpclett.7b01965.

Details of experimental procedures and of KMC simulations and angular dependence of the pair correlation function explained by the simulations (PDF)

## AUTHOR INFORMATION

### Corresponding Author

E-mail: Pavel.Kocan@mff.cuni.cz.

### ORCID

P. Matvija: 0000-0002-1567-6930

P. Kocán: 0000-0002-7677-557X

### Notes

The authors declare no competing financial interest.

## ACKNOWLEDGMENTS

This work was supported by the Czech Science Foundation (Contract No. 16-15802S) and by Charles University (Project GAKU No. 326515).

## REFERENCES

- (1) Tang, K. B. K.; Palmer, R. E.; Teillet-billy, D.; Gauyacq, J. P. Orientational Ordering of a 2D Molecular Gas. *Chem. Phys. Lett.* **1997**, *277*, 321–325.
- (2) Mateo-Martí, E.; Rogero, C.; Gonzalez, C.; Sobrado, J. M.; De Andrés, P. L.; Martin-Gago, J. A. Interplay between Fast Diffusion and Molecular Interaction in the Formation of Self-Assembled Nanostructures of S-Cysteine on Au(111). *Langmuir* **2010**, *26*, 4113–4118.
- (3) Seljamaë-Green, R. T.; Simpson, G. J.; Grillo, F.; Greenwood, J.; Francis, S. M.; Schaub, R.; Lacovic, P.; Baddeley, C. J. Assembly of A Chiral Amino Acid on an Unreactive Surface: (s)-Proline On Au(111). *Langmuir* **2014**, *30*, 3495–3501.
- (4) Kröger, I.; Stadtmüller, B.; Stadler, C.; Ziroff, J.; Kochler, M.; Stahl, A.; Pollinger, F.; Lee, T. L.; Zegenhagen, J.; Reinert, F.; et al. Submonolayer Growth of Copper-phthalocyanine on Ag(111). *New J. Phys.* **2010**, *12*, 083038.
- (5) Matvija, P.; Rozbořil, F.; Sobotik, P.; Ošťádal, I.; Pieczyrak, B.; Jurczyszyn, L.; Kocán, P. Electric-Field-Controlled Phase Transition in a 2D Molecular Layer. *Sci. Rep.* **2017**, *7*, 7357.
- (6) Ghanbari, E.; Wagner, T.; Zeppenfeld, P. Layer-Resolved Evolution of Organic Thin Films Monitored by Photoelectron Emission Microscopy and Optical Reflectance Spectroscopy. *J. Phys. Chem. C* **2015**, *119*, 24174–24181.
- (7) Hansen, J. P.; McDonald, I. R. *Theory of Simple Liquids*; Elsevier: New York, 2007.
- (8) Soper, A. K. Orientational Correlation Function for Molecular Liquids: the Case of Liquid Water. *J. Chem. Phys.* **1994**, *101*, 6888.
- (9) Munro, R. G.; Bureau, N. Radial Distribution Studies under Highly Constrained Conditions. *J. Res. Natl. Bur. Stand.* **1980**, *85*, 99–108.
- (10) Andreani, C.; Dore, J. C.; Ricci, F. P. Structural Characterization of Diatomic Fluids by Diffraction Studies. *Rep. Prog. Phys.* **1991**, *54*, 731–788.
- (11) Siwick, B. J. An Atomic-Level View of Melting Using Femtosecond Electron Diffraction. *Science* **2003**, *302*, 1382–1385.
- (12) Micoulaut, M. Structure of Densified Amorphous Germanium Dioxide. *J. Phys.: Condens. Matter* **2004**, *16*, L131–L138.
- (13) Schitter, G.; Rost, M. J. Scanning Probe Microscopy at Video-Rate. *Mater. Today* **2008**, *11*, 40–48.
- (14) Wolkow, R. A. Direct Observation of an Increase in Buckled Dimers on Si(001) at Low Temperature. *Phys. Rev. Lett.* **1992**, *68*, 2636–2639.

- (15) Jarolímek, T.; Mysliveček, J.; Sobotík, P.; Ošťádal, I. Adsorption and diffusion of Ag atoms on Si(111)-(7×7) Surface. *Surf. Sci.* **2001**, *482*-485, 386–390.
- (16) Matvija, P.; Sobotík, P.; Ošťádal, I.; Kocán, P. Diverse Growth of Mn, In and Sn Islands on Thallium-Passivated Si(111) Surface. *Appl. Surf. Sci.* **2015**, *331*, 339–345.
- (17) Sakamoto, K.; Eriksson, P. E. J.; Mizuno, S.; Ueno, N.; Tochihara, H.; Uhrberg, R. I. G. Core-Level Photoemission Study of Thallium Adsorbed on a Si(111)-(7×7) Surface: Valence State of Thallium and the Charge State of Surface Si Atoms. *Phys. Rev. B: Condens. Matter Mater. Phys.* **2006**, *74*, 075335.
- (18) Lee, S. S.; Song, H. J.; Kim, N. D.; Chung, J. W.; et al. Structural and Electronic Properties of Thallium Overlayers on the Si(111)-7×7 Surface. *Phys. Rev. B: Condens. Matter Mater. Phys.* **2002**, *66*, 23312.
- (19) Gottfried, J. M. Surface Chemistry of Porphyrins and Phthalocyanines. *Surf. Sci. Rep.* **2015**, *70*, 259–379.
- (20) Upward, M. D.; Beton, P. H.; Moriarty, P. Adsorption of Cobalt Phthalocyanine on Ag Terminated Si(111). *Surf. Sci.* **1999**, *441*, 21–25.
- (21) Menzli, S.; BenHamada, B.; Arbi, I.; Souissi, A.; Laribi, A.; Akremi, A.; Chefli, C. Adsorption Study of Copper Phthalocyanine on Si(111)( $\sqrt{3} \times \sqrt{3}$ )r30°Ag Surface. *Appl. Surf. Sci.* **2016**, *369*, 43–49.
- (22) Stadtmüller, B.; Kröger, I.; Reinert, F.; Kumpf, C. Submonolayer Growth of CuPc on Noble Metal Surfaces. *Phys. Rev. B: Condens. Matter Mater. Phys.* **2011**, *83*, 085416.
- (23) Rochford, L. a.; Hancox, I.; Jones, T. S. Understanding Domain Symmetry in Vanadium Oxide Phthalocyanine Monolayers on Au (111). *Surf. Sci.* **2014**, *628*, 62–65.
- (24) Bobaru, S. C.; Salomon, E.; Layet, J. M.; Angot, T. Structural Properties of Iron Phthalocyanines on Ag(111): from the Submonolayer to Monolayer Range. *J. Phys. Chem. C* **2011**, *115*, 5875–5879.
- (25) Stadler, C.; Hansen, S.; Kröger, I.; Kumpf, C.; Umbach, E. Tuning Intermolecular Interaction in Long-range-ordered Submonolayer Organic Films. *Nat. Phys.* **2009**, *5*, 153–158.
- (26) Kocán, P.; Sobotík, P.; Ošťádal, I. Metallic-like Thallium Overlayer on a Si(111) Surface. *Phys. Rev. B: Condens. Matter Mater. Phys.* **2011**, *84*, 233304.
- (27) See the [Supporting Information](#) for details of the experimental setup and Monte Carlo simulations.
- (28) Reith, D.; Putz, M.; Muller-Plathe, F. Deriving Effective Mesoscale Potentials from Atomistic Simulations. *J. Comput. Chem.* **2003**, *24*, 1624–1636.

# **Supplemental Material: The Pair Correlation Function of a 2D Molecular Gas Directly Visualized by Scanning Tunneling Microscope**

P. Matvija, F. Rozbořil, P. Sobotík, I. Ošt'ádal, and P. Kocán\*

*Charles University, Faculty of Mathematics and Physics, Department of Surface and Plasma Science, V Holešovičkách 2, 180 00, Prague, Czech Republic*

E-mail: pavel.kocan@mff.cuni.cz

## Experimental details

Experiments were carried out in an ultra-high vacuum non-commercial STM apparatus with a base pressure below  $5 \times 10^{-9}$  Pa. All experiments were done at room temperature. Pressure during the experiments was sustained within the order of  $10^{-8}$  Pa. The Si(111)/Tl-(1×1) surface was prepared by the thermal deposition of 1 ML<sub>1×1</sub> of thallium (purity 99.999 %, 1 ML<sub>1×1</sub> =  $7.83 \times 10^{14}$  atoms cm<sup>-2</sup>) on the Si(111)-(7×7) surface and annealing at 300 °C for 2 minutes.<sup>1</sup> The Si(111)-(7×7) surface was prepared on the Sb-doped Si monocrystal (resistivity 0.005 - 0.01 Ω.cm) by flashing to 1200 °C. F<sub>16</sub>CuPc molecules (from TCI, purified by sublimation, purity > 98%) were deposited on the passivated surface after cooling down the sample to the room temperature. The amount of deposited molecules was measured by a quartz thickness monitor. One monolayer of molecules (1 ML =  $5.2 \times 10^{13}$  molecules/cm<sup>2</sup>) was calibrated by depositing a saturated layer of molecules.

All presented STM images were measured with the sample voltage within the range (-2V, -3V) and the tunneling current below 40 pA. In our previous work<sup>2</sup> we studied near-monolayer coverages of non-fluorinated CuPC molecules and found a strong influence of STM tip-induced electric field on a local density of molecules. From the dependence of averaged molecular density on deposited amount (Fig. 3(a) of the Letter) and from the agreement with KMC simulations (Fig. 3(b) of the Letter) we can assume that the effect is not so strong in case of the fluorinated CuPC molecules, probably due to a stronger repulsion between the molecules. However we cannot exclude that the actual local coverage of molecules under the STM tip might be somewhat higher than the nominal values.

During the image acquisition the scanning speed ranged from 0.1 ms to 1 ms per pixel. Fast processes were averaged on the level of the feedback loop (bandwidth ≈ 600 Hz). Smooth STM data in the pseudo-3D view<sup>3</sup> were obtained by scanning the surface in high resolution and by averaging over up to 25 neighboring points. No other post-processing was used. Peak positions in Fig. 3(c) in the Letter were obtained as distances of the first maxima in the  $n(x, y)$  profiles from the centers of immobile F<sub>16</sub>CuPc molecules. The profiles were taken

in a direction from the center of the immobile molecule to the center of the closest molecule in the close-packed ordering [marked by an arrow in Fig. 3(b) of the Letter]. The position of the center of the immobile  $F_{16}CuPc$  molecule in the profiles was estimated as the middle between the two minima surrounding the peak corresponding to the immobile molecule.

## KMC simulations

In the kinetic Monte Carlo lattice-gas simulation, the  $F_{16}CuPc$  molecule was modeled with a real shape reflecting geometry where each molecule occupies 15 lattice points as shown in Fig. 1(a) of the Letter. The energy of an adsorption configuration is increased by each lattice point in which two neighboring molecules overlap. No interaction was considered between non-overlapping molecules.

The standard rejection-free algorithm as described by Bortz, Kalos and Lebowitz<sup>4</sup> was used to determine the time evolution of the system during simulation. All simulations were performed at a temperature of 300 K. Only two processes were considered: migration of a molecule to an adjacent lattice point and rotation by 60°. Activation energies for both processes were chosen arbitrarily as 0.3 eV. Since we use the same activation energies for rotation and jump of the molecules and we integrate over simulation steps, the pair correlation function is invariant of the activation energies and temperature in the studied case. The exact values of the barriers only determine the average time step of the simulation. The overlap energy penalty was set low enough to enable the formation of a close-packed structure at high coverage with the average overlap incidence lower than  $2.5 \times 10^{-4}$  per adsorption site. Activation energies involving overlapping molecules were dynamically calculated as an intersection point of neighboring parabolic potentials.<sup>5</sup>

The simulation was split into two parts: a relaxation phase and an integration phase.

At the beginning of the relaxation phase, the required number of molecules was placed randomly on the surface and the simulation was run for a fixed number of steps to allow the

overlap incidence to drop and the molecules to reach an equilibrium state.

During the following integration phase, the lattice occupancy by the central point of a molecule was accumulated. Only the central points of the molecules were considered as they correspond to dominant features of the static molecules in STM images. The integration phase was run for a fixed number of simulation steps (at least  $1.5 \times 10^6$  steps per molecule).

Finally, the molecular density  $n(x, y)$  was obtained by dividing the integrated count in each lattice-point by the number of simulation steps. This determines the average lattice-point occupancy over the course of the simulation.

## Angular dependence of the correlation function

The  $F_{16}CuPc$  molecule is not radially symmetric causing the value of the pair correlation function to depend on the angle with respect to the fixed molecule. Some local maxima of the time-averaged surface concentration of molecules are explained in Fig. S1. The highest value of  $n(x, y)$  is located at the two closest points where a molecule can be located in any orientation without overlap with the central fixed molecule [Fig. S1(a)]. The second highest local maxima are located at the four points above and below the lobes of the fixed molecule [Fig. S1(b)]. The third highest maxima are located to the left and right of the lobes of the fixed molecule [Fig. S1(c)]. These positions have a lower occupation than those in Fig. S1(b) due to the proximity of points shown in Fig. S1(a). Points shown in panels (b) and (c) correspond to close-packed structures of  $F_{16}CuPc$  molecules with the lowest center-to-center distance.

As shown in Fig. S1(d), the interference-like patterns can be also rationalized by possible layouts of individual molecules. The local maximum between the two fixed molecules can be explained by 3 molecules forming a bridge without overlapping.

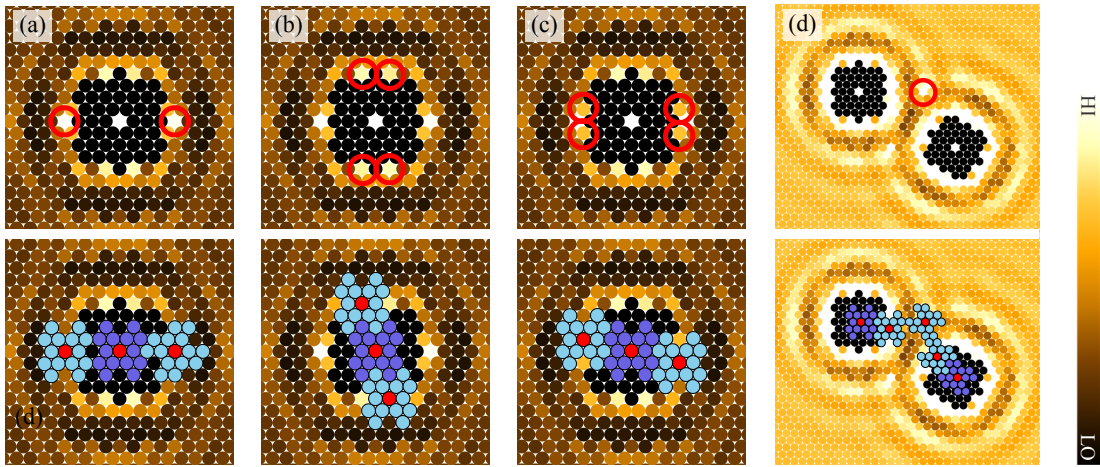


Figure S1: Local maxima of  $n(x, y)$  near the fixed molecule (dark blue). Circles in upper panels mark the local maxima, corresponding configurations are depicted in bottom panels. (a) The highest value of  $n(x, y)$ . (b) The second highest local maxima. (c) Third highest maxima. (d) The local maximum between two fixed molecules. Image (d) uses a different color scale compared to (a)-(c) to enhance the visibility of the second and third circular shells around the fixed molecules.

## References

- (1) Lee, S. S.; Song, H. J.; Kim, N. D.; Chung, J. W. Structural and Electronic Properties of Thallium Overlayers on the Si(111)-7×7 Surface. *Phys. Rev. B* **2002**, *66*, 23312.
- (2) Matvija, P.; Rozbořil, F.; Sobotík, P.; Ošt'ádal, I.; Pieczyrak, B.; Jurczyszyn, L.; Kocán, P. Electric-Field-Controlled Phase Transition in a 2D Molecular Layer. *Sci. Rep.* **2017**, *7*, 7357.
- (3) Nečas, D.; Klapetek, P. Gwyddion: an Open-Source Software for SPM Data Analysis. *Cent. Eur. J. Phys.* **2012**, *10*, 181–188.
- (4) Bortz, A. B.; Kalos, M. H.; Lebowitz, J. L. New Algorithm for Monte-Carlo Simulation of Ising Spin Systems. *J. Comput. Phys.* **1975**, *17*, 10–18.
- (5) Hood, E. S.; Toby, B. H.; Weinberg, W. H. Precursor-mediated Molecular Chemisorp-

tion and Thermal Desorption: the Interrelationships among Energetics, Kinetics, and Adsorbate Lattice Structure. *Phys. Rev. Lett.* **1985**, *55*, 2437–2440.

### 6.3 Electric-field-induced self-assembly of organic molecules on the Si(111)/Tl-(1×1) surface

In the previous section, we showed that  $F_{16}CuPc$  molecules form a 2D surface gas up to a full monolayer coverage. The same holds true for CuPc molecules up to a coverage of  $\approx 0.6$  ML. Interestingly, at the coverage between  $\approx 0.6$  ML and  $\approx 0.95$  ML, CuPc molecules can be observed by STM in a 2D-gas phase, condensed phase or mixed 2D-gas/condensed phase, depending on the scanning voltage and the local layout of surface defects. At the full monolayer coverage, only the condensed phase is observed.

We focus our attention on the extraordinary voltage-dependent behavior of CuPc molecules in the paper III (page 77). During the STM experiments, we discovered that the behavior of CuPc molecules changes abruptly at a certain negative value of  $V_{ts}$ . Hereafter we will refer to this value as  $V_T$ . We found out that CuPc molecules (i) self-assemble below  $V_T$ , (ii) disassemble once they are exposed to a voltage above  $V_T$  and that (iii) the disassembled CuPc molecules tend to interact with the tip at the voltage above  $V_T$ . The interaction is often destructive for the tip resolution. To resolve the nature of the abrupt behavior, while preserving the tip resolution, we opted for direct imaging of the condensed non-interacting phase interrupted by a short voltage pulses to the region above  $V_T$ . Such pulses are nondestructive for the tip, while still induce abrupt rearrangements of CuPc self-assembled structures.

As a result of repetitive voltage pulses with different shapes and amplitudes we concluded that the measured probabilities of switching agree well with random reordering of the self-assembled structures after they are exposed to a voltage above  $V_T$ . Based on ab-initio and KMC simulations, we proposed a simple model in which ordering and disordering is induced by the electrostatic interaction between dipoles connected to CuPc molecules and the strong non-uniform electric field between the STM tip and the sample. In the model, molecular dipoles are pulled into or pushed out of the area under the tip, according to the orientation of the electric field. The interaction changes the local density of molecules under the tip and forces the molecules to assemble.

The ability to control molecular density by means of external stimuli would allow programmable molecular patterning at scales accessible by recent lithography techniques [107]. So far, only a small number of switchable ordered molecular structures have been reported. These structures are limited to liquid-solid interfaces [108–113], where it is hard to determine the exact mechanism of switching, or to small inorganic molecules [114], which are not suitable for further functionalization. In an atomically clean environment under UHV, synchronized rotations of molecular rotors have been realized recently [115]. However, to allow molecular patterning, switching of an assembly of mobile molecules mediated by surface diffusion would be necessary (see Fig. S7 in the Supplementary materials of the paper III). Up to now, no such study in the well defined UHV environment has been reported.

My contribution to the paper III can be summarized as follows. I obtained all experimental data presented in the paper. I discovered that stability of self-assembled CuPc structures on the surface depends strongly on the electric-field between the STM tip and sample. I proposed and carried out switching experiments presented in Fig. 1 of the paper III. I analyzed the experimental data and prepared it for the publication. With the help of co-authors, I wrote the manuscript.

# SCIENTIFIC REPORTS



OPEN

## Electric-field-controlled phase transition in a 2D molecular layer

Peter Matvija<sup>1</sup>, Filip Rozbořil<sup>1</sup>, Pavel Sobotík<sup>1</sup>, Ivan Ošádal<sup>1</sup>, Barbara Pieczyrak<sup>2</sup>, Leszek Jurczyszyn<sup>2</sup> & Pavel Kocán<sup>1</sup>

Received: 6 April 2017

Accepted: 23 June 2017

Published online: 04 August 2017

**Self-assembly of organic molecules is a mechanism crucial for design of molecular nanodevices. We demonstrate unprecedented control over the self-assembly, which could allow switching and patterning at scales accessible by lithography techniques. We use the scanning tunneling microscope (STM) to induce a reversible 2D-gas-solid phase transition of copper phthalocyanine molecules on technologically important silicon surface functionalized by a metal monolayer. By means of ab-initio calculations we show that the charge transfer in the system results in a dipole moment carried by the molecules. The dipole moment interacts with a non-uniform electric field of the STM tip and the interaction changes the local density of molecules. To model the transition, we perform kinetic Monte Carlo simulations which reveal that the ordered molecular structures can form even without any attractive intermolecular interaction.**

The process of molecular self-assembly, using organic molecules as building blocks of spontaneously grown molecular structures, became one of the leading topics important for development of molecular devices<sup>1,2</sup>. In recent applications, such as organic field-effect transistors<sup>3</sup>, tunnel diodes<sup>4</sup>, solar cells<sup>5</sup>, light-emitting diodes<sup>6</sup> etc., static ordered layers are utilized. A possibility to control molecular density—and thus ordering of whole molecular assemblies—by means of external stimuli would allow programmable molecular patterning<sup>7</sup> at scales accessible by recent lithography techniques. Controlled switching has been well demonstrated on the level of isolated molecules<sup>8–15</sup>, but connecting the single-molecular switches to the rest of a functional device remains an obstacle<sup>15,16</sup>. A small number of switchable ordered molecular structures reported up to date is limited to liquid-solid interfaces<sup>17–22</sup> or small inorganic molecules<sup>23</sup>. In atomically clean environment under ultra-high vacuum (UHV), synchronized rotations of molecular rotors have been realized very recently<sup>24</sup>. However, to allow molecular patterning, switching of an assembly of mobile molecules mediated by surface diffusion would be necessary. So far, no such study in well defined UHV environment has been reported.

In our previous studies, we have shown that the Si(111)/Tl substrate is weakly interacting and suitable for growth of ordered ad-layers of metal atoms<sup>25–27</sup>. Compared to bare silicon surfaces, where adsorbed molecules are immobilized by strong chemical bonding to silicon surface atoms<sup>28–31</sup>, the self-assembly of phthalocyanines on weakly interacting surfaces depends on a delicate balance between adsorbate-substrate and inter-molecular interactions, and on external parameters such as temperature and surface coverage<sup>32</sup>. For growth of organic ordered layers composed of metallo-phthalocyanines (MPc), the weakly interacting metal surfaces are typically used as substrates<sup>32</sup>. A dominant factor governing the adsorption of different MPc molecules is a van der Waals interaction between the molecules and substrate, often resulting in a net static dipole moment perpendicular to the surface. Intermolecular interactions are weak attractive or even repulsive due to an interaction of the static dipoles, depending on the average inter-molecular distance<sup>32–34</sup>. The stable self-assembled layers are therefore often observed only at close-to-monolayer coverage, when the thermal motion of the molecules is limited by its neighbors<sup>32,35,36</sup>.

Here, we demonstrate the electric-field-controlled room-temperature switching of the copper phthalocyanine (CuPc) self-assembled arrays on the Si(111)/Tl-(1 × 1) surface, evidenced experimentally by the scanning tunneling microscopy (STM) and explained with help of ab-initio calculations. Stability of the ordered CuPc arrays during the scanning depends strongly on the polarity and amplitude of the applied tip-surface voltage. Negative sample bias stabilizes the ordered CuPc arrays, while application of positive sample biases causes the fast disintegration. By means of a strong electric field under the STM tip, we repeatedly change the orientation and position of all molecules within the domain. Measured probabilities of the domain changes demonstrate an existence

<sup>1</sup>Faculty of Mathematics and Physics, Charles University, Prague, 121 16, Czech Republic. <sup>2</sup>Instytut Fizyki Doswiadczennej, Uniwersytet Wroclawski, Wroclaw, 50-001, Poland. Correspondence and requests for materials should be addressed to P.M. (email: matvija.peter@gmail.com)

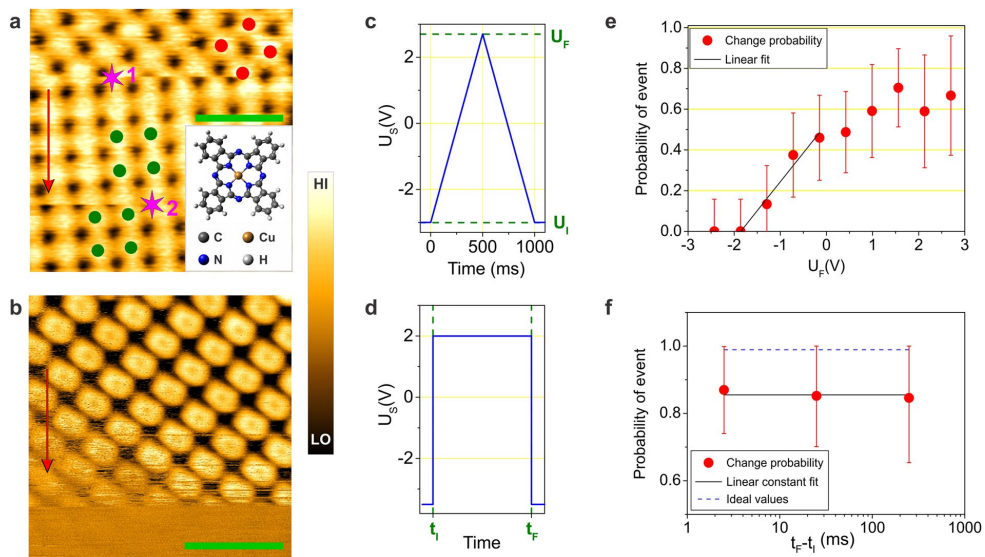


**Figure 1.** Field-induced switching of the CuPc self-assembled molecular array. (a) Change of a domain orientation (1) and position (2) as a response to voltage pulses. Purple stars mark positions above which the pulses were applied. The image was taken at the sample bias  $U_s = -2.3$  V. The inset depicts the structural model of a CuPc molecule. Red and green dots mark positions of molecules in the molecular structures with different orientations. (b) STM image of the CuPc molecular array taken at the sample bias of  $-1.7$  V, which is close to the threshold of imaging the stable arrays. Red arrows indicate the scanning direction. Green bars denote the length of  $3$  nm. (c,e) Shape of the triangular voltage pulse and corresponding dependence of the domain change probability on the peak voltage of the pulse  $U_F$ . The values of probability were acquired from the  $320$  voltage pulses applied over the same domain. (d,f) Shape of the rectangular voltage pulse and corresponding dependence of the domain change probability on the pulse duration. The results were acquired from  $100$  voltage pulses applied over the same domain. Dashed line denotes ideal probability of random switching in a system of  $45$  domains (see Supplementary). The error bars represent a range of two standard deviations. Note that absolute values of the voltages and probabilities can vary for different STM tips and different surface coverages, but the character of the measured probability dependence remains the same.

of a voltage threshold above which the changes occur. Based on the results of ab-initio calculations and kinetic Monte Carlo (KMC) simulations, we provide a simple electrostatic model of the field-molecule interaction. The model explains the probabilistic nature of the process by disordering and the following random re-assembly of the molecular array at the measured threshold voltage. We expect that a similar electric-field control over surface assembly can be achieved for a wide range of systems containing a weakly interacting mobile adsorbate carrying sufficiently strong permanent dipoles.

## Results

**Switching of the self-assembled arrays.** The CuPc molecule belongs to the family of planar macrocycles, phtalocyanines. These molecules tend to self-organize on nonreactive surfaces, as previously demonstrated using various substrates<sup>13, 14, 32, 37–42</sup>. STM images of approximately  $0.8$  monolayer (ML) of the CuPc molecules deposited on the Si(111)/Ti-( $1 \times 1$ ) surface reveal the similar long-range ordering (Figs 1a,b and 2a,b). However, in addition to the self-assembly, we observe that the stability of the CuPc arrays at sub-monolayer coverage depends strongly on the scanning conditions. The ordered arrays are observable only at negative sample voltage  $U_s < -1.8$  V, while scanning at sample voltage  $U_s > -1.8$  V leads to noisy STM images without the presence of any ordered molecular structure. We note that the absolute value of the threshold can vary for different experimental conditions such as surface concentration of CuPc molecules, temperature etc. The presence of the threshold indicates that the electric field of the STM tip influences the molecular ordering. Figure 1b shows an STM image scanned at a sample voltage of  $-1.7$  V, which is near the threshold of imaging the stable molecular arrays. During the scanning, the image of the initially stable CuPc structure is repeatedly perturbed by abrupt spikes until the ordered pattern completely disappears.

To reveal the mechanism of the tip influence we investigated the effect of tip-sample voltage pulses on the ordering of the molecules. During the image acquisition the scanning is stopped for a moment required by the pulse and then continues immediately. A result of such procedure is shown in Fig. 1a, where the purple stars mark positions where the pulses were applied. Abrupt changes in molecular layouts are visible immediately after the

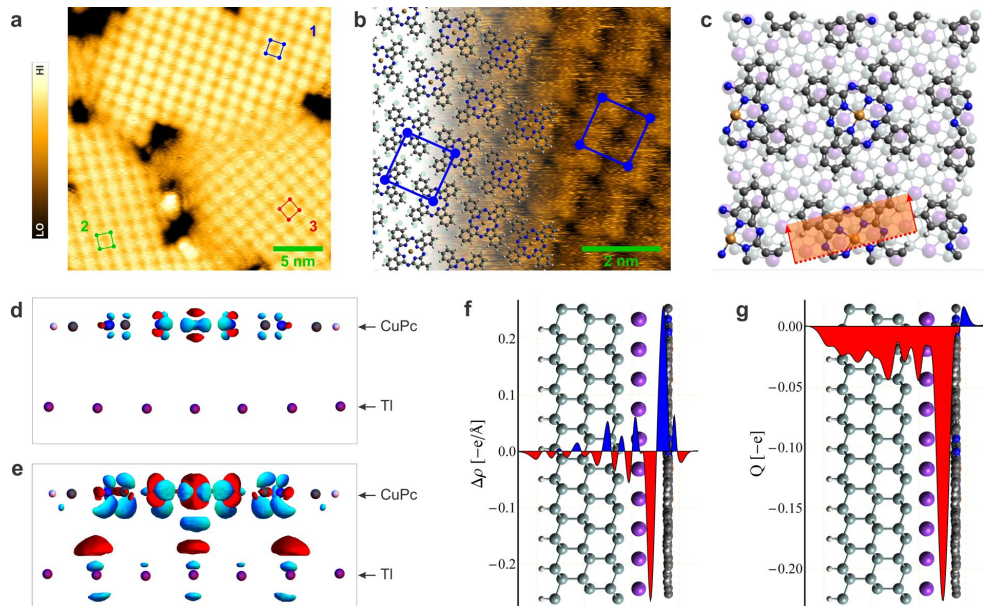


**Figure 2.** Self-assembly of CuPc molecules on the thallium-passivated Si(111) surface. (a) The Tl-passivated surface covered by almost 1 ML of CuPc molecules. Three domain orientations of the ordered CuPc array are shown.  $U_s = -3$  V. (b) STM image of the CuPc array superimposed by the structural model.  $U_s = -2$  V. Red, green and blue squares mark unit cells of the CuPc molecular arrays. (c) Top view of the relaxed structural model. Purple and gray spheres denote positions of Tl and Si atoms, respectively. (d,e) Isosurfaces of the constant difference of the charge density. The cross-section plane, the direction of the view and the volume imaged is marked in the panel c. The isovalue are set to  $0.012 \text{ e}\text{\AA}^{-3}$  (panel d) and  $0.005 \text{ e}\text{\AA}^{-3}$  (panel e). Red and blue colors represent electron density depletion and accumulation, respectively. (f,g) Side view of the relaxed structure superimposed by the plane-integrated charge transfer  $\Delta\rho$  (panel f) and the cumulative charge transfer  $Q$  (panel g).

application of a pulse. More STM images of CuPc ordered arrays and their response to voltage pulses can be seen in Supplementary materials.

As we will show later in this work, the changes in the molecular layouts can be assigned to domain changes of the same CuPc ordering on the Tl-(1 × 1) surface. By repetitive applying different voltage pulses, we obtained statistics of the successful collective switching, which are present in Fig. 1e and f. We opted for two pulse shapes with various duration and amplitude. First, we applied triangular pulses (see Fig. 1c) with the initial voltage of  $-3$  V (the stable ordered structure) to study dependence of the switching probability on the peak voltage  $U_p$ . Though pulses with  $U_p$  in the range of  $(-3\text{ V}, -1.8\text{ V})$  do not induce any change of the molecular arrays, from  $U_p \approx -1.8\text{ V}$  the probability of the domain change increases approximately linearly with  $U_p$ . The maximal switching probability ( $0.65 \pm 0.10$ ) is reached for sample biases  $U_p \gtrsim 1.0$  V. In the case of the rectangular pulse (see Fig. 1d), the sample voltage is changed from the scanning value of  $-3.5$  V directly to  $+2.0$  V and is held constant for various time intervals. The average probability of a pulse-induced domain change saturates at the level of  $(0.9 \pm 0.1)$ . In the switching experiment, we were able to distinguish two types of the domain change. In the first case (Fig. 1a-1) the orientation of the molecular superlattice is changed, while in the second case (Fig. 1a-2) the orientation is preserved and the superlattice is shifted with respect to the original layout. For simplicity, the changes will be referred to as domain rotations and domain shifts, respectively. Taking into account the two categories, we analyzed the rectangular-pulse-induced changes and we determined that the average probability of the domain rotation is  $(0.6 \pm 0.1)$  and the average probability of the domain shift is  $(0.3 \pm 0.1)$ . In the studied range from milliseconds to seconds, no dependence on the pulse duration was observed, implying that the time necessary for the switching is less than 1 ms.

Besides the external electric field, concentration of CuPc molecules and of surface defects have a significant impact on ordering of the molecules as well. The domain switching was observed only at near-monolayer surface coverage in the range of  $0.6\text{--}0.95$  ML. At saturated coverage, we observe stable molecular arrays at all scanning conditions. Here, CuPc molecules cover tightly the whole surface with exception of defects in the Tl-(1 × 1) layer and their surrounding (see Fig. 2a). At lower coverage, we observe only individual adsorption of CuPc molecules at step edges. Independently on STM conditions, no stable ordering of the molecules was observed on terraces up to  $\approx 0.6$  ML, indicating the presence of the 2D gas-like phase of highly mobile molecules on the surface. At all

coverages, defects represent positions of the surface that are forbidden for CuPc molecules (see Supplementary materials for more STM images). Ordering of the molecules is substantially affected by defects especially if the local concentration of defects is high.

Existence of the voltage threshold of domain switching and absence of ordered molecular arrays at voltages above the threshold suggest that stability of the arrays depends on the external electric field. Changes of the tip-sample electric field during the pulse can explain switching of CuPc domains as follows. Molecular arrays are stabilized by the electric field at sample voltage  $U_s \lesssim -1.8$  V. During the voltage pulse, at sample voltages corresponding to the saturated switching probability ( $U_s \gtrsim 1.0$  V), a whole domain of the CuPc array disintegrates faster than recordable by the STM. At the end of the pulse, when the voltage is restored to the original value, CuPc molecules reorganize randomly into one of the possible configurations (in total 90 different configurations exist; among them 45 configurations with 3 possible orientations are distinguishable in our experiment; see Supplementary for details). The expected probability of a domain change, rotation and shift in such a system would be  $\frac{44}{45}, \frac{2}{3}$  and  $\frac{14}{45}$ , respectively. In the experiment, we obtained the average values of  $(0.9 \pm 0.1)$ ,  $(0.6 \pm 0.1)$  and  $(0.3 \pm 0.1)$ , respectively. All expected values fall within the standard deviation range of the measured values. Slightly lower mean experimental values are caused by surface defects which can locally “pin” or “block” some domains. Another reason is the limited room-temperature STM resolution, which could be insufficient to distinguish small domain shifts.

**Geometric and electronic structure of the ordered array.** To clarify the details associated with the molecule-substrate and molecule-molecule interactions, the relativistic DFT calculations have been performed. In our models, we took into account the experimentally obtained Cu-Cu distance of the nearest molecules of  $\approx 1.4$  nm and the orientation of the molecules in the surface reconstruction shown in Fig. 2b. The remaining free parameter, the position of CuPc molecules with respect to the Ti-(1 × 1) surface, was determined by evaluating the adsorption energy of molecules in the most symmetric sites (on top, hollow and bridge) after relaxation of the testing configurations. The highest adsorption energy per molecule was obtained for central Cu atoms of CuPc molecules located above bridge positions of the Ti-(1 × 1) lattice (2.92 eV), followed by the hollow (2.83 eV) and on top sites (2.68 eV). In the relaxed bridge configuration (see Fig. 2c), molecules lie 0.33 nm above the Ti-(1 × 1) layer. Due to symmetries of the CuPc molecules and the bridge positions of the substrate, there are 90 equivalent CuPc configurations in total (see Supplementary for details).

On the Ti-(1 × 1) surface, the CuPc molecules are stabilized by van der Waals forces, which is also the case of phthalocyanine molecules on metal surfaces<sup>32,34</sup>. Figure 2d and e show the charge transfer  $\Delta\rho$  induced by an interaction of the CuPc molecule with the substrate. The transfer is calculated from the DFT calculations by subtracting charge densities of the isolated systems of the substrate and the adsorbate from that of the combined system. A dominant charge transfer is associated with Cu, N and C atoms in the central ring of the CuPc molecule (see Fig. 2d with isovalue  $\pm 0.012$  eÅ<sup>-3</sup>). The transfer has a mirror symmetry plane, which is identical with the plane of the CuPc molecule and is parallel to the surface. Therefore, the transfer within the molecule contributes only to quadrupole or higher moments of the molecule.

Contributions to the dipole moment can be found mainly in the region between CuPc molecules and the Ti layer (see Fig. 2e with isovalue  $\pm 0.005$  eÅ<sup>-3</sup>). The plane-integrated charge transfer  $\Delta\rho$  (see Fig. 2f) shows that the charge is shifted from proximity of the surface towards molecules. In Fig. 2g, the cumulative charge transfer, obtained as  $Q(z) = \int_{-\infty}^z \Delta\rho(z')dz'$  is shown, indicating that  $\approx 0.23$  e is transferred in maximum, which results in a static dipole moment of  $\approx 0.35$  eÅ. Similar formation of a dipole pointing from the substrate to adsorbed molecules was calculated for other phthalocyanine-on-metal systems<sup>32,43</sup>. In the following discussion, we neglect the complex charge transfer within the system and take into account only the dipole moments perpendicular to the surface plane.

**Mechanism of the phase switching.** Under the studied conditions, the molecules are highly mobile on the surface. Two electrostatic forces acting on the molecules carrying dipoles can influence their dynamics: a dipole-dipole repulsive force and an interaction between the molecular dipole and the tip-sample electric field. The former can be neglected, because at the distance corresponding to the most close-packed configuration the interaction energy is  $\approx 0.6$  meV, which is much less than the energy of thermal fluctuations at room temperature  $kT \approx 25$  meV, where  $k$  is the Boltzmann constant. Presence of a biased STM tip in proximity of the surface induces a strong electric field (typically  $\geq 10^7$  V cm<sup>-1</sup>) with maximum intensity  $E \approx U/d_{TS}$  under the tip apex, where  $d_{TS}$  is the tip-sample spacing and  $U$  is the tip-sample voltage. Along the surface, the field is non-uniform and almost vanishes at a distance of the tip radius. The influence of the gradient field on mobile dipoles on surfaces has been previously reported<sup>44</sup>. In case of the positive (negative) tip bias and dipoles  $\mu$  pointing perpendicularly to the surface, the field represents a potential well (hill) with depth (height)  $\mu E$  for each dipole. If the well is deeper than  $kT$ , an isolated molecule would be “trapped” by the tip. If a reservoir of molecules is available, their concentration would increase locally under the tip. Assuming the tip-sample separation of 1 nm,  $\mu E \approx kT$  at a sample bias of  $\sim -0.7$  V. Because the high concentration results in ordering of the molecules, this value can be considered a threshold for assembly of the CuPc molecules into ordered arrays.

When scanning at the tip bias inducing sufficiently deep potential well, the locally increased concentration of molecules allows formation of a stable CuPc array (see Fig. 3). If we lower or reverse the bias (e.g. during a voltage pulse), the well becomes shallow or even reversed, which rapidly decreases the molecular concentration under the tip. At the end of the voltage pulse, when we sweep the voltage back to the scanning voltage, the potential well is restored and the molecules reorder randomly in the region under the tip to one of 90 possible configurations. This explanation is supported experimentally by Fig. 1e, where the voltage necessary for the CuPc assembly obtained

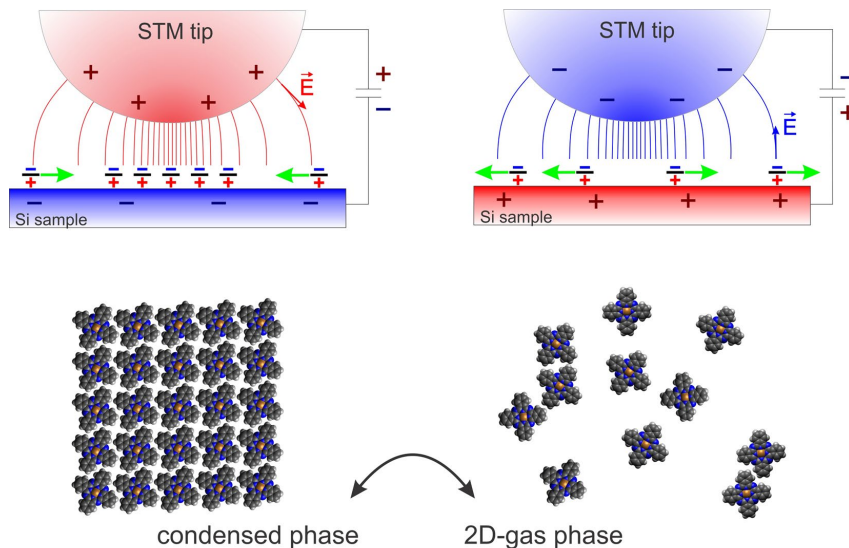


**Figure 3.** Graphic illustration of the field-controlled switching mechanism. Static dipoles carried by the CuPc molecules are represented schematically by the  $+/ -$  signs on the surface. Green arrows indicate forces acting upon the dipoles in the electric field.

from electrostatic relations and DFT calculations fits within the region of transition between zero and saturated switching probability, and by Fig. 1f, where the measured average switching probabilities correspond well to values expected in a system where domains switch into random domain layouts.

In order to further support the hypothesis that the existence of a potential well under the tip is sufficient for the self-assembly of molecules, we performed kinetic Monte Carlo simulations. In the simulations, the real shape of CuPc molecules is modeled by 15 lattice points of the substrate lattice and the interaction of molecules is limited to a steric repulsion which applies when the molecules overlap (see Supplementary). Apart from that, no inter-molecular interaction is included. Results of the simulations can be seen in Supplementary Fig. S6. On the intact surface the molecules at 0.75 ML coverage behave as a 2D gas (Fig. S6a and c). As a potential well is introduced to the surface, the local molecular coverage inside the well increases, inducing formation of the close-packed ordered molecular structure (Fig. S6b). The structure remains stable while the potential is held sufficiently low (Fig. S6d).

## Discussion

Our explanation neglects several factors. First, we consider a dipole moment only and omit higher moments of the molecule. The higher moments would affect a molecule-molecule interaction, which is though insignificant at RT, while the crucial interaction of the molecules with the tip field is driven by the dipole moment dominantly. Secondly, the strong field may affect molecule-substrate distance accompanied by a charge redistribution<sup>45</sup>. Such changes can be treated by the dipole approximation as well. If the dipole induced by the distance change was stronger than the static one, the tip-molecule interaction would be attractive at both bias polarities, in contrast to the experiment. Diffusion barriers can be modified by the field as well<sup>45</sup>, but we expect that at room temperature the diffusivity would be still very high, as supported by the field-independent 2D gaseous phase observed at coverage  $< 0.6$  ML. Thirdly, defects, such as step edges or point defects<sup>46</sup>, necessarily represent real boundary conditions, which may influence stability of ordered domains. In our experiments, we are able to find small areas isolated by defects where molecules are strongly confined and do not change their positions at any scanning conditions. Similarly, we are able to find areas with lower local concentration of molecules where we observe spontaneous switching even under otherwise stable conditions. Lastly, we note that experiments with different tips and coverage resulted in the qualitatively same results, however with different values of the threshold voltage in the range from  $-0.5$  V to  $-2$  V and different values of switching probabilities.

## Outlook

At sub-monolayer coverage and at room temperature, CuPc molecules behave like a 2D gas. We showed that, thanks to the permanent electric dipole between the molecules and the substrate, the local concentration of the molecules on the surface can be controlled by the nonuniform electric field. As ordering of the molecules is closely related to their local concentration, it is possible—at the scale of tens of nanometers—to switch between ordered and 2D-gas phases. An idea of patterning based on aggregation of molecules carrying dipoles by means of

a nonuniform field has been introduced theoretically by Suo and Hong a decade ago<sup>7</sup>. Later, Jiang *et al.* reported possibility of tip-field-induced freezing of molecules on metal surface at 77 K, benefiting of increasing diffusion barriers rather than of dipole moments<sup>45</sup>. Our results show that it is possible to achieve the adaptive field-induced patterning at room temperature on technologically well mastered silicon substrates (see Supplementary Fig. S7).

In general, adsorption of molecules at surfaces is often accompanied by a charge transfer and formation of adsorption-induced permanent dipoles. We therefore expect that interaction of an external electric field with the dipoles can be utilized to control the surface assembly of a wide range of weakly-interacting adsorbates and substrates, similarly to the case presented in this study.

## Methods

**STM.** Experiments were carried out in an ultra-high vacuum non-commercial STM apparatus with a base pressure below  $5 \times 10^{-9}$  Pa. Pressure during the experiments was sustained within the order of  $10^{-8}$  Pa. The Si(111)/Tl-(1 × 1) surface was prepared by the thermal deposition of 1 ML of thallium (purity 99.999 %) on the Si(111)-(7 × 7) surface and annealing at 300 °C for 2 minutes<sup>25</sup>. The Si(111)-(7 × 7) surface was prepared on the Sb-doped Si monocrystal (resistivity 0.005–0.01 Ω.cm) by flashing to 1200 °C. The samples were resistively heated by passing DC current. CuPc molecules were deposited on the passivated surface after cooling down the sample to the room temperature. Tunneling current was in the range 0.05–0.15 nA during the acquisition of all presented STM images.

**DFT.** Our theoretical study is based on the density functional theory as it is implemented in the Vienna Ab-initio Simulation Package (VASP)<sup>47–49</sup> and the use of plane wave basis set. In all presented calculations the description on the electron-ion interaction has been performed with the help of the projector-augmented wave (PAW) method while the exchange-correlation effects were included in the framework of generalized gradient approximation (GGA) in its Perdew-Burke-Ernzerhof (PBE) formulation<sup>50</sup>. The convergence of the energy of electronic states was performed using Davison-Block algorithm<sup>51</sup> and the atomic structure has been relaxed using the conjugate gradient method. All calculations presented in the paper were performed with the use of nine k-points. The influence of this factor was tested in separate check calculations. The cutoff energy applied during calculations was 450 eV. The considered system was represented by a repeated slab model composed of CuPc molecule at the top, one Tl layer and six Si layers. The bottom Si layer was saturated by H atoms. In the total-energy calculations the molecule and 5 topmost layers of the substrate were relaxed until the forces present were less than 0.01 eV/Å. The slabs were separated by 15 Å of vacuum. The van der Waals interactions were included using the scheme of Grimme<sup>52</sup>.

**KMC.** In the simulations, each molecule is represented by 15 lattice points which correspond to the real shape of CuPc molecules. The molecules can randomly either move to one of the 6 neighboring sites or rotate by 60°. Activation energy for both processes was calculated as the intersection point of neighboring harmonic potentials<sup>53</sup>. The energy of an adsorption configuration is increased by each lattice point in which two neighboring molecules overlap. Apart from that, no interaction was considered between non-overlapping molecules. The time-averaged maps of the local occupancy of lattice-points by molecules (see Supplementary Fig. S6) are obtained by averaging of the molecular positions over at least  $1.5 \times 10^6$  successive simulation steps per molecule.

## References

- Heath, J. R. Molecular Electronics. *Annu. Rev. Mater. Res.* **39**, 1–23 (2009).
- Claridge, S. A. *et al.* From the bottom up: dimensional control and characterization in molecular monolayers. *Chemical Society reviews* **42**, 2725–2745, <http://pubs.rsc.org/en/content/articlehtml/2013/cs/c2cs35365b> (2013).
- Borschchev, O. & Ponomarenko, S. A. Self-assembled organic semiconductors for monolayer field-effect transistors. *Polymer Science Series C* **56**, 32–46, doi:10.1134/S1811238214010044 (2014).
- Celestin, M., Krishnan, S., Bhansali, S., Stefanakos, E. & Goswami, D. Y. A review of self-assembled monolayers as potential terahertz frequency tunnel diodes. *Nano Research* **7**, 589–625 (2014).
- Ravi, S. K. & Tan, S. C. Progress and perspectives in exploiting photosynthetic biomolecules for solar energy harnessing. *Energy Environ. Sci.* **8**, 2551–2573 (2015).
- Sessolo, M. & Bolink, H. J. Hybrid organic-inorganic light-emitting diodes. *Advanced Materials* **23**, 1829–1845 (2011).
- Suo, Z. & Hong, W. Programmable motion and patterning of molecules on solid surfaces. *Proceedings of the National Academy of Sciences of the United States of America* **101**, 7874–7879 (2004).
- Pietzsch, O. *et al.* Current-Induced Hydrogen Tautomerization and Conductance Switching of Naphthalocyanine Molecules. *Science* **317**, 1203–1207 (2007).
- Qiu, X. H., Nazin, G. V. & Ho, W. Mechanisms of reversible conformational transitions in a single molecule. *Physical Review Letters* **93**, 1–4 (2004).
- Repp, J., Meyer, G., Olsson, F. E. & Persson, M. Controlling the charge state of individual gold adatoms. *Science* **305**, 493–495 (2004).
- Haijs, W. *et al.* Redox State Dependence of Single Molecular Conductivity. *JACS* **125**, 15294–15295 (2003).
- Yongfeng, W., Kröger, J., Berndt, R. & Hofer, W. A. Pushing and pulling a Sn Ion through an adsorbed phthalocyanine molecule. *Journal of the American Chemical Society* **131**, 3639–3643 (2009).
- Strózcka, A., Soriano, M., Pascual, J. I. & Palacios, J. J. Reversible change of the spin state in a manganese phthalocyanine by coordination of co molecule. *Phys. Rev. Lett.* **109**, 147202, <http://link.aps.org/doi/10.1103/PhysRevLett.109.147202> (2012).
- Zhang, J. L. *et al.* Reversible switching of a single-dipole molecule imbedded in two-dimensional hydrogen-bonded binary molecular networks. *Journal of Physical Chemistry C* **118**, 1712–1718 (2014).
- Zhang, J. L. *et al.* Towards single molecule switches. *Chem. Soc. Rev.* **44**, 2998, doi:10.1039/C4CS00377B (2015).
- Lörtscher, E. Wiring molecules into circuits. *Nature Nanotechnology* **8**, 381–384, <http://www.nature.com/doifinder/10.1038/nano.2013.105> (2013).
- Cui, K. *et al.* Potential-driven molecular tiling of a charged polycyclic aromatic compound. *Chemical Communications* **50**, 10376–10378, <http://pubs.rsc.org/en/content/articlepdf/2014/cc/c4cc04189e> (2014).
- Cometto, F. P., Kern, K. & Linzenfelder, M. Local Conformational Switching of Supramolecular Networks at the Solid/Liquid Interface. *ACS Nano* **9**, 5544–5550 (2015).

19. Lei, S. B. *et al.* Electric driven molecular switching of asymmetric tris(phthalocyaninato) lutetium triple-decker complex at the liquid/solid interface. *Nano Letters* **8**, 1836–1843 (2008).
20. Zhang, X. M., Zeng, Q. D. & Wang, C. Reversible Phase Transformation at the Solid-Liquid Interface: STM Reveals. *Chemistry—an Asian Journal* **8**, 2330–2340 <Go to ISI>://WOS:000324748600008 (2013).
21. Snegir, S. V. & Yu, P. Switching at the Nanoscale: Light- and STM-Tip-Induced Switch of a Thiolated Diarylthene Self-Assembly on Au(111). *Langmuir* **30**, 13556–13563 (2014).
22. Pace, G. *et al.* Cooperative light-induced molecular movements of highly ordered azobenzene self-assembled monolayers. *Proceedings of the National Academy of Sciences* **104**, 9937–9942, <http://www.pnas.org/cgi/doi/10.1073/pnas.0703748104> (2007).
23. Wortmann, B. *et al.* Reversible 2d phase transition driven by an electric field: Visualization and control on the atomic scale. *Nano Letters* **16**, 528–533 (2016).
24. Zhang, Y. *et al.* Simultaneous and coordinated rotational switching of all molecular rotors in a network. *Nature Nanotechnology* **11**, 706–713, <http://www.nature.com/doifinder/10.1038/nnano.2016.69> (2016).
25. Matvija, P., Sobotík, P., Oštádal, I. & Kocán, P. Diverse growth of Mn, In and Sn islands on thallium-passivated Si(111) surface. *Applied Surface Science* **331**, 339–345, <http://www.sciencedirect.com/science/article/pii/S0169433215000914> (2015).
26. Lee, S. S. *et al.* Structural and electronic properties of thallium overlayers on the Si(111) – 7 × 7 surface. *Phys. Rev. B* **66**, 233312, <http://link.aps.org/doi/10.1103/PhysRevB.66.233312> (2002).
27. Sakamoto, K. *et al.* Core-level photoemission study of thallium adsorbed on a Si(111) – (7 × 7) surface: Valence state of thallium and the charge state of surface si atoms. *Phys. Rev. B* **74**, 075335, <http://link.aps.org/doi/10.1103/PhysRevB.74.075335> (2006).
28. Papageorgiou, N. *et al.* Physics of ultra-thin phthalocyanine films on semiconductors. *Progress in Surface Science* **77**, 139–170 (2005).
29. Rochet, F. *et al.* Copper phthalocyanine on Si(111) – 7 × 7 and Si(001) – 2 × 2: an XPS/AES and STM study. *Surface Science* **319**, 10–20 (1994).
30. Krejčí, O. *et al.* Chemisorption of acetophenone on Si(111) – 7 × 7, polar aromatic molecule on electronically complex surface. *The Journal of Physical Chemistry C* **120**, 9200–9206, <http://dx.doi.org/10.1021/acs.jpcc.6b00486> (2016).
31. Tao, F. & Xu, G. Q. Attachment chemistry of organic molecules on Si(111) – (7 × 7). *Accounts of chemical research* **37**, 882–893 (2004).
32. Gottfried, J. M. Surface chemistry of porphyrins and phthalocyanines. *Surface Science Reports* **70**, 259–379, <http://linkinghub.elsevier.com/retrieve/pii/S0167572915000114> (2015).
33. Stadler, C., Hansen, S., Kröger, I., Kumpf, C. & Umbach, E. Tuning intermolecular interaction in long-range-ordered submonolayer organic films. *Nature Physics* **5**, 153–158, <http://dx.doi.org/10.1038/nphys1176> (2009).
34. Peisert, H., Uihlein, J., Petraki, F. & Chass, T. Charge transfer between transition metal phthalocyanines and metal substrates: The role of the transition metal. *Journal of Electron Spectroscopy and Related Phenomena* **204**, 49–60, <http://dx.doi.org/10.1016/j.elspec.2015.01.005>.
35. Kröger, I. *et al.* Submonolayer growth of copper-phthalocyanine on Ag(111). *New Journal of Physics* **12** (2010).
36. Stadtmüller, B., Kröger, I., Reinert, F. & Kumpf, C. Submonolayer growth of CuPc on noble metal surfaces. *Physical Review B - Condensed Matter and Materials Physics* **83**, 085416, doi:[10.1103/PhysRevB.83.085416](http://dx.doi.org/10.1103/PhysRevB.83.085416) (2011).
37. Menzli, S. *et al.* Adsorption study of copper phthalocyanine on Si(111) ( $\sqrt{3} \times \sqrt{3}$ ) R30° Ag surface. *Applied Surface Science* **369**, 43–49, <http://linkinghub.elsevier.com/retrieve/pii/S0169433216302161> (2016).
38. Arbi, I. *et al.* Molecular arrangement investigation of copper phthalocyanine grown on hydrogen passivated Si(111) surfaces. *Applied Surface Science* **305**, 396–401, doi:[10.1016/j.apsusc.2014.03.100](http://dx.doi.org/10.1016/j.apsusc.2014.03.100) (2014).
39. Xiao, K. *et al.* Surface-Induced Orientation Control of CuPc Molecules for the Epitaxial Growth of Highly Ordered Organic Crystals on Graphene. *JACS* **135**, 3680–3687 (2013).
40. Floreano, L., Cossaro, A. & Gotter, R. Periodic arrays of Cu-phthalocyanine chains on Au (110). *J. Phys. Chem. C* **112**, 10794–10802, <http://pubs.acs.org/doi/abs/10.1021/jp11140e> (2008).
41. Upward, M. D., Beton, P. H. & Moriarty, P. Adsorption of cobalt phthalocyanine on Ag terminated Si(111). *Surface Science* **441**, 21–25 (1999).
42. Wagner, S. R. *et al.* Growth of Metal Phthalocyanine on Deactivated Semiconducting Surfaces Steered by Selective Orbital Coupling. *Physical Review Letters* **115**, 096101, doi:[10.1103/PhysRevLett.115.096101](http://dx.doi.org/10.1103/PhysRevLett.115.096101) (2015).
43. Amin, B., Nazir, S. & Schwingerschlogl, U. Molecular distortion and charge transfer effects in ZnPc/Cu(111). *Sci Rep* **3**, 1705, <http://www.ncbi.nlm.nih.gov/pmc/articles/PMC3609223/> (2013).
44. Whitman, L. J., Stroscio, J. A., Dragoset, R. A. & Celotta, R. J. Manipulation of Adsorbed Atoms and Creation of New Structures on Room-Temperature Surfaces with a Scanning Tunneling Microscope. *Science* **251**, 1206–1210, <http://www.sciencemag.org/content/251/4998/1206.abstract> (1991).
45. Jiang, N. *et al.* Diffusivity control in molecule-on-metal systems using electric fields. *Nano Letters* **10**, 1184–1188 (2010).
46. Kocán, P., Sobotík, P. & Oštádal, I. Metallic-like thallium overlayer on a si(111) surface. *Phys. Rev. B* **84**, 233304, doi:[10.1103/PhysRevB.84.233304](http://dx.doi.org/10.1103/PhysRevB.84.233304) (2011).
47. Kresse, G. & Hafner, J. Ab initio molecular dynamics for liquid metals. *Phys. Rev. B* **47**, 558–561, doi:[10.1103/PhysRevB.47.558](http://dx.doi.org/10.1103/PhysRevB.47.558) (1993).
48. Kresse, G. & Hafner, J. Ab initio molecular-dynamics simulation of the liquid-metal21amorphous-semiconductor transition in germanium. *Phys. Rev. B* **49**, 14251–14269, doi:[10.1103/PhysRevB.49.14251](http://dx.doi.org/10.1103/PhysRevB.49.14251) (1994).
49. Kresse, G. & Furthmüller, J. Efficient iterative schemes for ab initio total-energy calculations using a plane-wave basis set. *Phys. Rev. B* **54**, 11169–11186, doi:[10.1103/PhysRevB.54.11169](http://dx.doi.org/10.1103/PhysRevB.54.11169) (1996).
50. Perdew, J. P., Burke, K. & Ernzerhof, M. Generalized gradient approximation made simple. *Phys. Rev. Lett.* **77**, 3865–3868, doi:[10.1103/PhysRevLett.77.3865](http://dx.doi.org/10.1103/PhysRevLett.77.3865) (1996).
51. Davison, E. R. *Methods in Computational Molecular Physics* (Plenum, New York, 1983).
52. Grimme, S. Semiempirical GGA-type density functional constructed with a long-range dispersion correction. *Journal of Computational Chemistry* **27**, 1787–1799, doi:[10.1002/jcc.20495](http://dx.doi.org/10.1002/jcc.20495) (2006).
53. Hood, E. S., Toby, B. H. & Weinberg, W. H. Precursor-mediated molecular chemisorption and thermal desorption: the interrelationships among energy, kinetics, and adsorbate lattice structure. *Phys. Rev. Lett.* **55**, 2437 (1985).

## Acknowledgements

This work was supported by Czech Science Foundation (contract no. 16–15802S) and by the Charles University (project GAUK No. 326515). DFT calculations reported in this work have been performed at the Interdisciplinary Center of Mathematical and Computational Modeling of the University of Warsaw within Grant No. G44-10. B.P. and L.J. acknowledge the support from the University of Wrocław (Grant No. 1010/S/IFD/17).

## Author Contributions

P.M. performed STM measurements and analyzed the measured data. P.K. conceived and designed the experiments. I.O. and P.S. designed and constructed the experimental equipment. B.P. and L.J. performed DFT

calculations. F.R. performed KMC simulations. P.M. and P.K. wrote the paper. All authors discussed the results and commented on the manuscript.

**Additional Information**

**Supplementary information** accompanies this paper at doi:[10.1038/s41598-017-07277-7](https://doi.org/10.1038/s41598-017-07277-7)

**Competing Interests:** The authors declare that they have no competing interests.

**Publisher's note:** Springer Nature remains neutral with regard to jurisdictional claims in published maps and institutional affiliations.

 **Open Access** This article is licensed under a Creative Commons Attribution 4.0 International License, which permits use, sharing, adaptation, distribution and reproduction in any medium or format, as long as you give appropriate credit to the original author(s) and the source, provide a link to the Creative Commons license, and indicate if changes were made. The images or other third party material in this article are included in the article's Creative Commons license, unless indicated otherwise in a credit line to the material. If material is not included in the article's Creative Commons license and your intended use is not permitted by statutory regulation or exceeds the permitted use, you will need to obtain permission directly from the copyright holder. To view a copy of this license, visit <http://creativecommons.org/licenses/by/4.0/>.

© The Author(s) 2017

# **Electric-field-controlled phase transition in a 2D molecular layer**

(Supplementary information)

Peter Matvija<sup>1\*</sup>, Filip Rozbořil<sup>1</sup>, Pavel Sobotík<sup>1</sup>, Ivan Ošťádal<sup>1</sup>, Barbara Pieczyrak<sup>2</sup>, Leszek Jurczyszyn<sup>2</sup>, Pavel Kocán<sup>1</sup>

<sup>1</sup> Faculty of Mathematics and Physics, Charles University, Prague, Czech Republic

<sup>2</sup> Institute of Experimental Physics, University of Wrocław, Wrocław, Poland

\* corresponding author, email: matvija.peter@gmail.com

## Domain structure of the CuPc molecular array

Based on the STM experiments and DFT calculations we were able to determine the structural model of the most stable dense configuration of CuPc molecules on the Ti-1 × 1 surface (see Fig. 2 of the main article). To explain the switching experiment presented in Fig. 1 of the main article, it is important to understand the symmetry of the structure and its implications to number of possible configurations and number of configurations distinguishable in our STM experiments.

First of all, DFT calculations showed that the most stable position of the CuPc molecule on the Ti-1 × 1 surface is a bridge site. To obtain the minimal energy, central Cu atoms of CuPc molecules have to sit directly above the bridge sites and their orientation must be as it is shown in Fig. 2c in the main article. In order to create the molecular array with the minimal energy, all molecules of the same domain have to have the same orientation. There are 3 possible orientations of CuPc molecules corresponding to 3 different bridge positions within a 1 × 1 Ti cell (see Fig. S1a and Fig. S1c-e). Since CuPc molecules and bridge positions have common mirror symmetry (shown in Fig. S1), there are two different ways the molecules can be arranged on the substrate at each of the three orientations. The two different arrangements are marked by two different colors at each panel c-e. In the figure, only positions of central Cu atoms of CuPc molecules are marked and only one central molecule is fully depicted. Orientation of the rest of the molecules is the same as the orientation of the central molecule. Super-cells of the molecular arrays are marked by red, green and blue squares. If we count only configurations where central CuPc molecules sit above one given unit cell of the Ti-1 × 1 lattice, we obtain  $3 \times 2 = 6$  possible configurations. A super-cell of the CuPc molecular array, however, contains 15 unit cells of the Ti-1 × 1 lattice (see Fig. S1b). Therefore the total number of configurations of the CuPc molecular array equals to  $3 \times 2 \times 15 = 90$ .

In our STM experiments, a dominant feature of CuPc molecule imaging at room temperature and  $U_s \sim -3$  V is its central C-N macrocycle (see Fig. S5c). As a consequence, we are often not able to determine the orientation of individual molecules. Domains with the same orientation of the molecular superlattice, but the different orientation of individual molecules are perceived as

identical (see the different domains marked by the same color in Fig. S1c-S1e). The identity reduces the total number of 90 domains to 45 distinguishable domains and the total number of domain orientations to 3 distinguishable orientations.

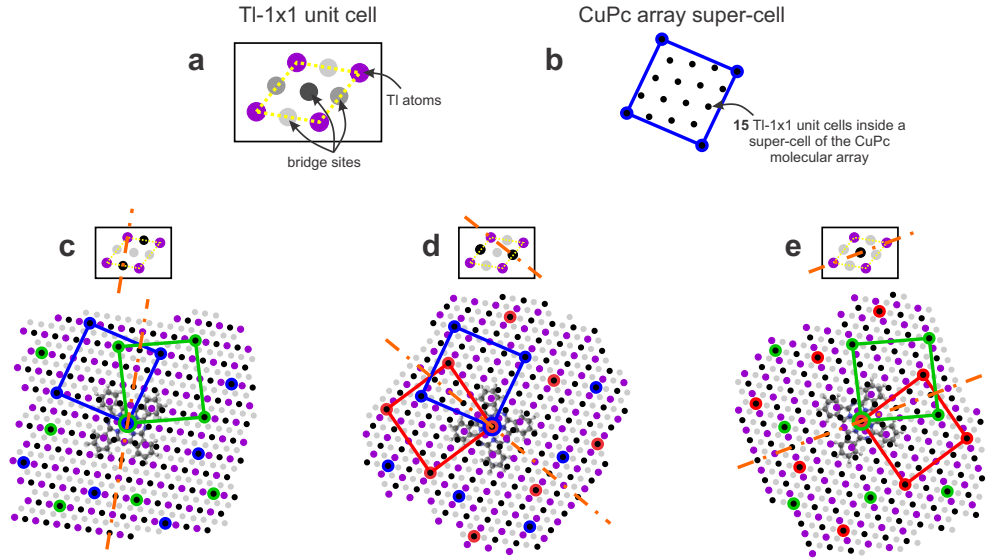


**Figure S1: Possible configurations of the CuPc molecular array on the  $\text{Ti}-1 \times 1$  surface.** **a**, Unit cell of the  $\text{Ti}-1 \times 1$  surface reconstruction. Positions of Tl atoms are marked by purple dots. Gray dots represent 3 bridge sites with different orientation in the unit cell. **b**, Example of a super-cell of the CuPc molecular array on the  $\text{Ti}-1 \times 1$  surface. Black dots mark positions of  $\text{Ti}-1 \times 1$  unit cells inside the super-cell of the CuPc array. **c-e**, Schematic drawing of possible configurations of CuPc molecular array on the  $\text{Ti}-1 \times 1$  surface. Each panel corresponds to one possible orientation of CuPc molecules on the surface. Bridge sites that can be occupied by a central Cu of a CuPc molecule in a given orientation are marked by black dots. Bridge sites corresponding to a different orientation of the molecules are marked by gray dots. There are two possible molecular arrangements in case of each orientation of the molecules (marked by two different colors on each panel). Positions of central Cu atoms of CuPc molecules are marked by red, green and blue dots. Unit cells of the molecular arrays are marked by squares of the same color. The same colors in different panels indicate the same orientations of the whole molecular arrays.

## Domain switching viewed by STM

Figures S2 - S4 display dynamic behavior of CuPc domains during the STM scanning. All images were acquired at  $U_s < -2$  V, which is above the switching threshold (i.e. the voltage is sufficiently high to stabilize CuPc domains). After application of voltage pulses which penetrate below the threshold, sudden domain changes are observed. Fig. S2 illustrates the domain changes on a large area. The imaged area is initially covered by a single domain of the CuPc molecules. The orientation of the domain is marked by blue lines. After application of a voltage pulse (top purple star), the right part of the domain is shifted (red lines), while the left part remains without a change. Domain boundary emerges between the two domains. The second pulse induces rotation of both domains.

More detailed images of the domain switching are presented in Fig. S3. Note that a big fraction of the pulses, especially in Fig. S3f, does not induce any domain change. We observe this effect on areas with high density of defects which represent boundary condition for the ordering of molecules and can pin or prevent certain domains.

The influence of defects on CuPc ordering is even more pronounced in Fig. S4. Here high density of defects induces stabilization of domains on certain areas (marked by 1a), while other areas remain covered by unstable and spontaneously switching domains (marked by 2). Areas where defects prevent formation of stable domains and areas where defects hinder aggregation of molecules from surrounding surface are covered by a 2D molecular gas (marked by 3). At the interface of the stable domains and the gas, gradual decrease of the apparent molecular brightness can be seen. The lower brightness of the molecules can be explained as lower probability to find a molecule at a given position. The lower probability arises as a result of the dynamic equilibrium between the gas and condensed phase and it is the clear evidence of presence of the 2D gas phase on the surface.

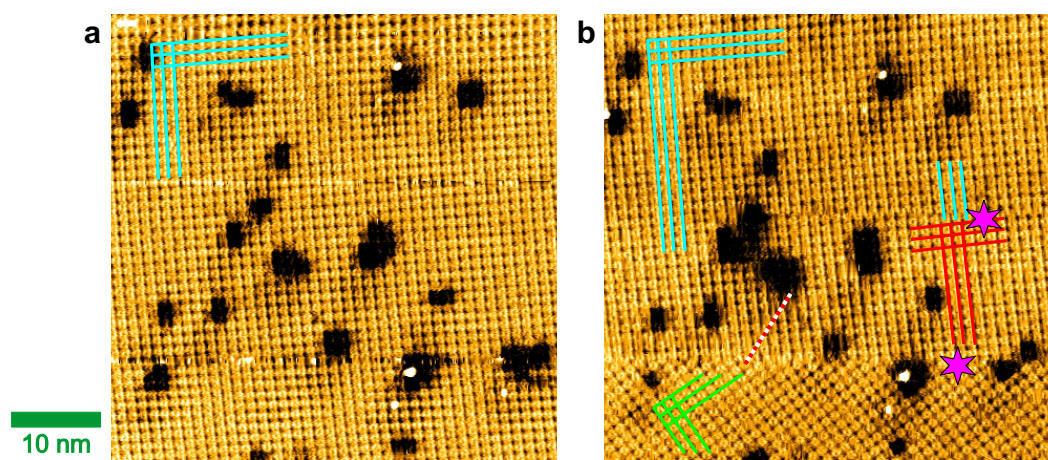


**Figure S2: Domain switching on a large area.** Two successive STM images of the same area are displayed. Differently colored solid lines mark orientations of different domains. Red-white line marks a domain boundary. Purple stars on the panel **b** marks positions where triangular voltage pulses ( $U_f = 1$  V) were executed.  $U_s = -3$  V. Note that (i) images were not corrected for a thermal drift and piezo-creep and that (ii) positions of defects remain unchanged after the pulses. Scanning direction is from the top to the bottom.

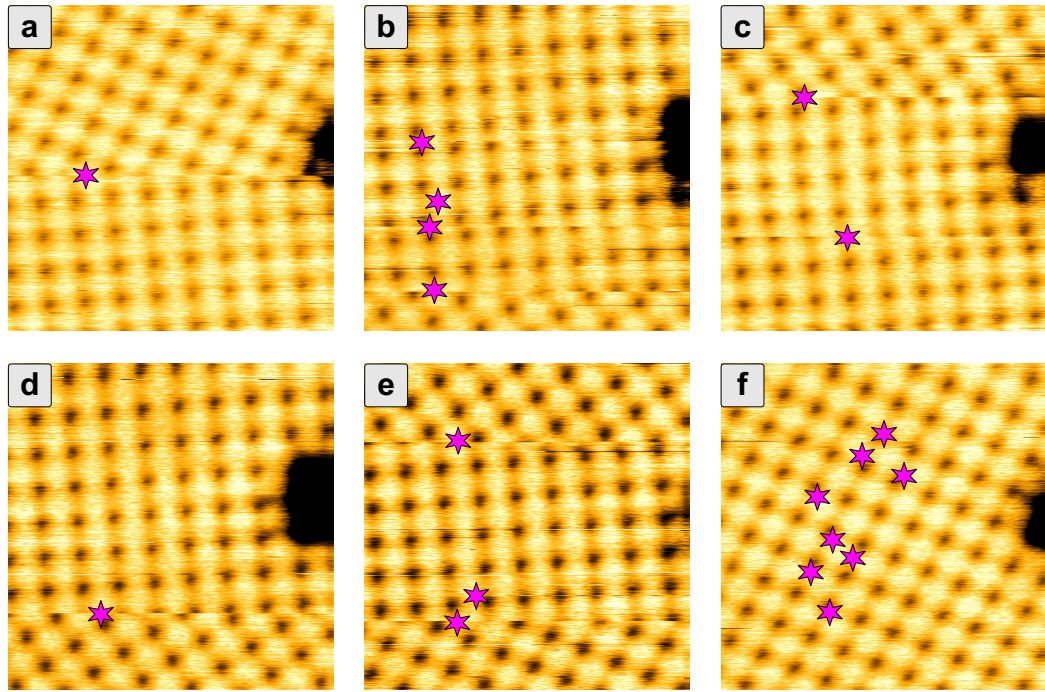


**Figure S3: Multiple domain switching.** Six consecutive STM images,  $U_s = -2.3$  V, showing abrupt domain changes after voltage pulses. 19 triangular voltage pulses from -2.3 V to 0 V were executed. 9 domain changes were identified. Positions of the voltage pulses are marked by purple stars. Note that slight deviations in the position of the dark defect are caused by inaccurate manual compensation of the thermal drift. Size of the imaged area is 10 nm  $\times$  10 nm. Scanning direction is from the top to the bottom.

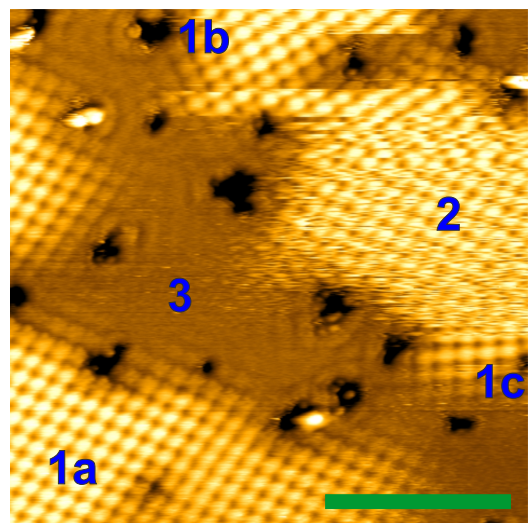


Figure S4: **Coexistence of the 2D gas and condensed phase on the surface.** **1a**, **1b** and **1c** mark three possible orientations of stable CuPc domains. **2** marks an unstable CuPc domain which is spontaneously switching during the STM measurement. Area between the domains is filled by a 2D gas (marked by **3**). Surface coverage  $\approx 0.7$  ML.  $U_s = -2.5$  V. Green bar denotes 10 nm.

### DFT calculations

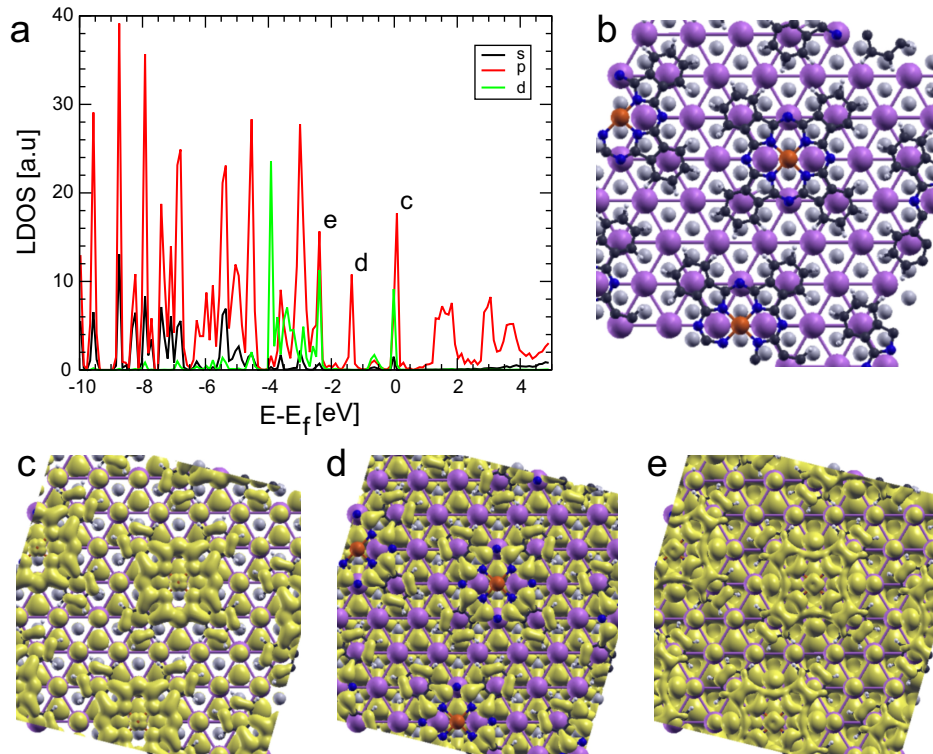


Figure S5: **a**, Calculated local density of states (LDOS) of the CuPc molecule deposited on the Si(111)/Tl-(1x1) surface projected on the s (black line), p (red line) and d (green line) orbitals of the molecule. **b**, Top view of the corresponding system. **c**, **d**, **e**, Partial charge distributions of the LDOS features shown in the panel **a**; isosurface values are  $0.0035$ ,  $0.0035$  and  $0.002 \text{ e\AA}^{-3}$ , respectively.

### KMC simulations

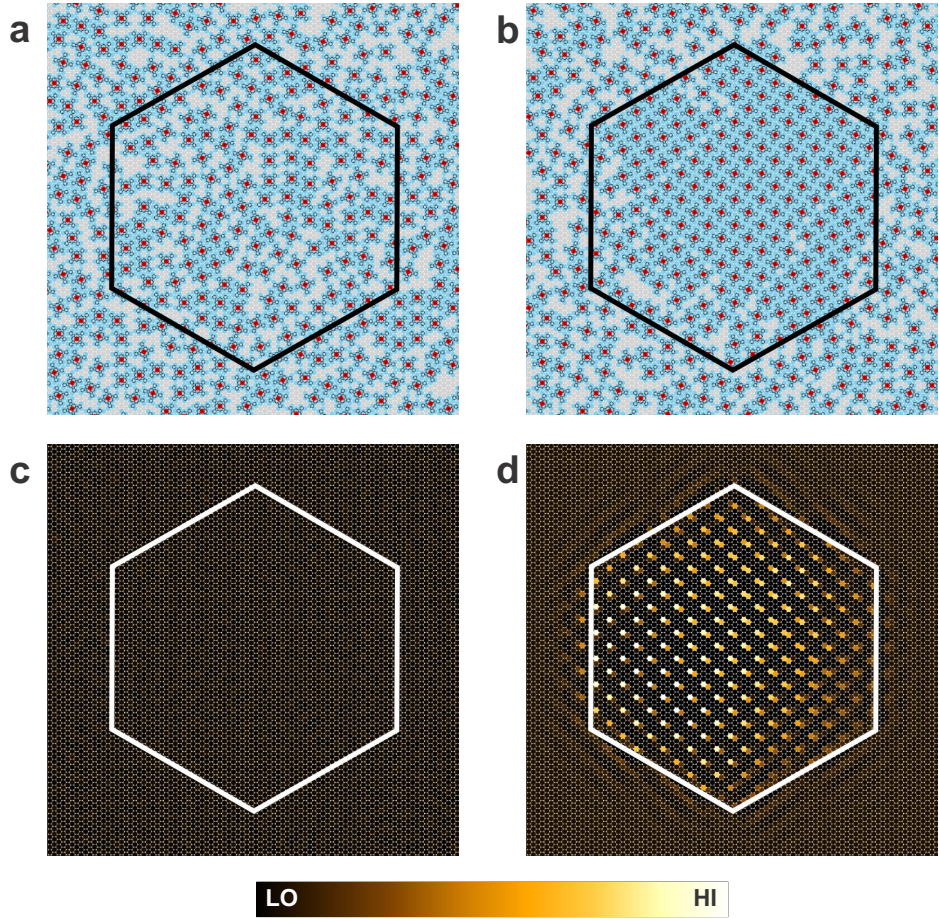


Figure S6: KMC simulations of the molecular condensation in the STM-tip-induced potential well on the surface with 0.75 ML molecular coverage at a temperature of 300 K. The figure displays snapshots of KMC simulations without (a) and with (b) the 0.075 eV potential well and the corresponding maps of the time-averaged lattice-points occupancy (c and d, respectively). The hexagonal potential well is outlined by black and white lines. The well has a rectangular cross-section, i.e. the adsorption energy per one lattice point is increased for every lattice point inside the well by the constant value of 0.075 eV. Close-packed ordering of molecules in the potential well can be clearly seen even without any attractive interaction between CuPc molecules.

### Stable switchable molecular arrays

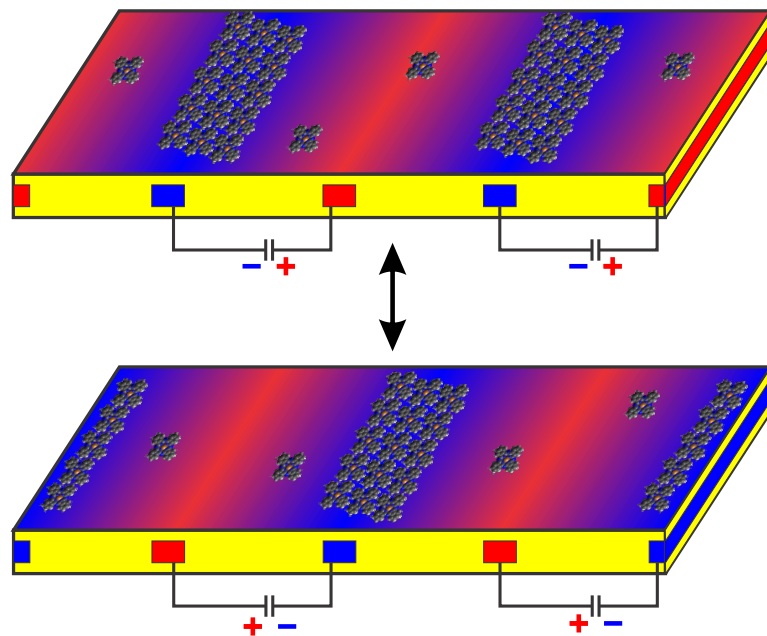


Figure S7: The proposition of a stable switchable molecular array consisting of Tl-covered undoped silicon layer (yellow), conducting buried electrodes (red and blue) and mobile CuPc 2D gas on top of the surface. Red and blue colors of the surface represent areas of potential hills and wells, respectively.

# Summary

This work is devoted to study of the Tl-passivated Si(111) surface. The main goal of the study is to investigate the behavior of organic molecules on this specific surface, however the results can be applied to a wide range of other systems comprising metal surfaces, weakly interacting organic molecules, 2D gases etc.

Main results of our work can be summarized as follows:

- We revealed that the polarity of adsorbed molecules affects the initial stage of their chemisorption on the Si(111) – (7 × 7) surface. (paper V)
- We showed that the nature of Tl bonding in the (1 × 1) and in the desorption-induced ( $\sqrt{3} \times \sqrt{3}$ ) structures is similar, i.e. Tl atoms are single-bonded in both structures. (paper IV)
- We showed that the Tl passivation of the Si(111) surface substantially increases surface diffusion of single-atom adsorbates (at least by nine orders of magnitude). As a result of the increased diffusivity, growth modes of different adsorbates on the Si(111)/Tl – (1 × 1) surface resemble the growth modes observed on low-reactive metal surfaces. (paper I)
- We proposed a novel method for observation of a local time-averaged density of 2D molecular gases on surfaces. (paper II)
- We performed, to the best of our knowledge, the first direct observation of a pair correlation function of a 2D molecular gas. (paper II)
- We determined the adsorption configurations of individual and self-assembled CuPc and F<sub>16</sub>CuPc molecules on the Si(111)/Tl – (1 × 1) surface. (papers II and III)
- We discovered that the phase of CuPc molecules on the Si(111)/Tl – (1 × 1) surface can be controlled by a non-uniform electric field. We explained the mechanism of the phase control by a simple model considering only the electrostatic interaction of molecules and the STM tip. (paper III)

These results offer a new perspective on dynamic molecular processes on reactive and non-reactive surfaces. Thanks to the methods proposed in the work, mobile molecules on non-reactive surfaces can be studied and even controlled by means of the STM. The possibility to study and to control the mobile molecules is the first step towards building more complex molecular surface architectures that will be used in future molecular-electronic devices.

# Bibliography

- [1] P. Matvija, P. Sobotík, I. Oštádal, and P. Kocán, “Diverse growth of Mn, In and Sn islands on thallium-passivated Si(111) surface,” *Applied Surface Science*, vol. 331, pp. 339–345, 2015.
- [2] P. Matvija, F. Rozbořil, P. Sobotík, I. Oštádal, and P. Kocán, “Pair correlation function of a 2D molecular gas directly visualized by scanning tunneling microscope,” *Journal of Physical Chemistry Letters*, vol. 8, pp. 4268–4272, 2017.
- [3] P. Matvija, F. Rozbořil, P. Sobotík, I. Oštádal, B. Pieczyrak, L. Jurczyszyn, and P. Kocán, “Electric-field-controlled phase transition in a 2D molecular layer,” *Scientific Reports*, vol. 7, p. 7357, 2017.
- [4] P. Kocán, P. Sobotík, P. Matvija, M. Setvín, and I. Oštádal, “An STM study of desorption-induced thallium structures on the Si(111) surface,” *Surface Science*, vol. 606, no. 13-14, pp. 991–995, 2012.
- [5] O. Krejčí, P. Matvija, P. Zimmermann, P. Sobotík, I. Oštádal, and P. Kocán, “Chemisorption of acetophenone on Si(111)-7×7. polar aromatic molecule on electronically complex surface,” *Journal of Physical Chemistry C*, vol. 120, no. 17, pp. 9200–9206, 2016.
- [6] “Samsung starts industry’s first mass production of system-on-chip with 10-nanometer FinFET technology.” <https://news.samsung.com/global/samsung-starts-industrys-first-mass-production-of-system-on-chip-with-10-nanometer-finfectechnology>.
- [7] A. Emboras, J. Niegemann, P. Ma, C. Haffner, A. Pedersen, M. Luisier, C. Hafner, T. Schimmel, and J. Leuthold, “Atomic scale plasmonic switch,” *Nano letters*, vol. 16, no. 1, pp. 709–714, 2015.
- [8] J. L. Zhang, J. Q. Zhong, J. D. Lin, W. P. Hu, K. Wu, G. Q. Xu, A. T. Wee, and W. Chen, “Towards single molecule switches,” *Chemical Society Reviews*, vol. 44, no. 10, pp. 2998–3022, 2015.
- [9] J. Repp, G. Meyer, F. E. Olsson, and M. Persson, “Controlling the charge state of individual gold adatoms,” *Science*, vol. 305, no. 5683, pp. 493–495, 2004.
- [10] C. Dekker *et al.*, “Carbon nanotubes as molecular quantum wires,” *Physics today*, vol. 52, pp. 22–30, 1999.
- [11] V. Amendola, L. Fabbrizzi, C. Mangano, and P. Pallavicini, “Molecular machines based on metal ion translocation,” *Accounts of chemical research*, vol. 34, no. 6, pp. 488–493, 2001.
- [12] D. Xiang, X. Wang, C. Jia, T. Lee, and X. Guo, “Molecular-scale electronics: from concept to function,” *Chem. Rev.*, vol. 116, no. 7, pp. 4318–4440, 2016.

- [13] Y. Suzuki, M. Hietschold, and D. R. Zahn, “Growth of copper phthalocyanine on hydrogen passivated vicinal silicon (111) surfaces,” *Applied surface science*, vol. 252, no. 15, pp. 5449–5452, 2006.
- [14] I. Arbi, B. B. Hamada, A. Souissi, S. Menzli, C. B. Azzouz, A. Laribi, A. Akremi, *et al.*, “Molecular arrangement investigation of copper phthalocyanine grown on hydrogen passivated Si(111) surfaces,” *Applied Surface Science*, vol. 305, pp. 396–401, 2014.
- [15] M. Gruyters, “Growth and structure of Fe, Co and Ni films on hydrogen-terminated Si(111) surfaces,” *Surface science*, vol. 515, no. 1, pp. 53–60, 2002.
- [16] L. Vitali, F. P. Leisenberger, M. G. Ramsey, and F. P. Netzer, “Thallium overlayers on Si(111): structures of a ‘new’ group III element,” *Journal of Vacuum Science & Technology A: Vacuum, Surfaces, and Films*, vol. 17, no. 4, pp. 1676–1682, 1999.
- [17] K. Sakamoto, T. Oda, A. Kimura, K. Miyamoto, M. Tsujikawa, A. Imai, N. Ueno, H. Namatame, M. Taniguchi, P. Eriksson, *et al.*, “Abrupt rotation of the Rashba spin to the direction perpendicular to the surface,” *Physical review letters*, vol. 102, no. 9, p. 096805, 2009.
- [18] K. Sakamoto, T. Oda, A. Kimura, Y. Takeichi, J. Fujii, R. Uhrberg, M. Donath, and H. W. Yeom, “Symmetry induced peculiar rashba effect on thallium adsorbed Si(111) surfaces,” *Journal of Electron Spectroscopy and Related Phenomena*, vol. 201, pp. 88–91, 2015.
- [19] S. Lee, H. Song, N. Kim, J. Chung, K. Kong, D. Ahn, H. Yi, B. Yu, and H. Tochihara, “Structural and electronic properties of thallium overlayers on the Si(111)-7×7 surface,” *Physical Review B*, vol. 66, no. 23, p. 233312, 2002.
- [20] L. Vitali, M. Ramsey, and F. Netzer, “Rotational epitaxy of a ‘soft’ metal overlayer on Si(111),” *Surface science*, vol. 452, no. 1, pp. L281–L286, 2000.
- [21] J. M. Gottfried, “Surface chemistry of porphyrins and phthalocyanines,” *Surface Science Reports*, vol. 70, no. 3, pp. 259–379, 2015.
- [22] N. Papageorgiou, E. Salomon, T. Angot, J.-M. Layet, L. Giovanelli, and G. Le Lay, “Physics of ultra-thin phthalocyanine films on semiconductors,” *Progress in surface science*, vol. 77, no. 5, pp. 139–170, 2004.
- [23] W. Wu, L. A. Rochford, S. Felton, Z. Wu, J. Yang, S. Heutz, G. Aeppli, T. S. Jones, N. Harrison, and A. Fisher, “Magnetic properties of copper hexadecaphthalocyanine ( $F_{16}CuPc$ ) thin films and powders,” *Journal of Applied Physics*, vol. 113, no. 1, p. 013914, 2013.
- [24] Z. Bao, A. J. Lovinger, and A. Dodabalapur, “Organic field-effect transistors with high mobility based on copper phthalocyanine,” *Applied Physics Letters*, vol. 69, no. 20, pp. 3066–3068, 1996.

- [25] J. Yuan, J. Zhang, J. Wang, X. Yan, D. Yan, and W. Xu, “Bottom-contact organic field-effect transistors having low-dielectric layer under source and drain electrodes,” *Applied physics letters*, vol. 82, no. 22, pp. 3967–3969, 2003.
- [26] L. Hung and C. W. Tang, “Interface engineering in preparation of organic surface-emitting diodes,” *Applied physics letters*, vol. 74, no. 21, pp. 3209–3211, 1999.
- [27] T. T. T. Luong, Z. Chen, and H. Zhu, “Flexible solar cells based on copper phthalocyanine and buckminsterfullerene,” *Solar Energy Materials and Solar Cells*, vol. 94, no. 6, pp. 1059–1063, 2010.
- [28] R. Young, J. Ward, and F. Scire, “The topografiner: An instrument for measuring surface microtopography,” *Review of Scientific Instruments*, vol. 43, no. 7, pp. 999–1011, 1972.
- [29] R. D. Young, “Field emission ultramicrometer,” *Review of Scientific Instruments*, vol. 37, no. 3, pp. 275–278, 1966.
- [30] J. S. Villarrubia, “The topografiner: An instrument for measuring surface microtopography,” *A Century of Excellence in Standards, Measurements, and Technology*, pp. 214–218, 2001.
- [31] G. Binnig and H. Rohrer, “Scanning tunneling microscopy - from birth to adolescence,” *Reviews of Modern Physics*, vol. 59, no. 3, p. 615, 1987.
- [32] G. Binnig and H. Rohrer, “Scanning tunneling microscopy,” *IBM Journal of research and development*, vol. 44, no. 1/2, p. 279, 2000.
- [33] G. Binnig, H. Rohrer, C. Gerber, and E. Weibel, “Surface studies by scanning tunneling microscopy,” *Physical Review Letters*, vol. 49, pp. 57–61, Jul 1982.
- [34] G. Binnig, H. Rohrer, C. Gerber, and E. Weibel, “ $7\times7$  reconstruction on Si(111) resolved in real space,” *Physical Review Letters*, vol. 50, pp. 120–123, Jan 1983.
- [35] K. Takayanagi, Y. Tanishiro, M. Takahashi, and S. Takahashi, “Structural analysis of Si(111)- $7\times7$  by UHV-transmission electron diffraction and microscopy,” *Journal of Vacuum Science & Technology A: Vacuum, Surfaces, and Films*, vol. 3, no. 3, pp. 1502–1506, 1985.
- [36] C. Kittel, *Introduction to solid state physics*. Wiley, 2005.
- [37] P. A. M. Dirac, “On the theory of quantum mechanics,” *Proceedings of the Royal Society of London A: Mathematical, Physical and Engineering Sciences*, vol. 112, no. 762, pp. 661–677, 1926.
- [38] L. Skála, *Úvod do kvantové mechaniky*. Academia, 2005.
- [39] J. Bardeen, “Tunnelling from a many-particle point of view,” *Physical Review Letters*, vol. 6, no. 2, p. 57, 1961.
- [40] M. Born and R. Oppenheimer, “Zur quantentheorie der moleküle,” *Annalen der Physik*, vol. 389, no. 20, pp. 457–484, 1927.

- [41] A. D. Gottlieb and L. Wesoloski, “Bardeen’s tunnelling theory as applied to scanning tunnelling microscopy: a technical guide to the traditional interpretation,” *Nanotechnology*, vol. 17, no. 8, p. R57, 2006.
- [42] P. A. Dirac, “The quantum theory of the emission and absorption of radiation,” in *Proceedings of the Royal Society of London A: Mathematical, Physical and Engineering Sciences*, vol. 114, pp. 243–265, The Royal Society, 1927.
- [43] J. Tersoff and D. Hamann, “Theory and application for the scanning tunneling microscope,” *Physical review letters*, vol. 50, no. 25, p. 1998, 1983.
- [44] J. Tersoff and D. Hamann, “Theory of the scanning tunneling microscope,” *Physical Review B*, vol. 31, no. 2, p. 805, 1985.
- [45] A. Selloni, P. Carnevali, E. Tosatti, and C. D. Chen, “Voltage-dependent scanning-tunneling microscopy of a crystal surface: Graphite,” *Physical Review B*, vol. 31, pp. 2602–2605, Feb 1985.
- [46] C. J. Chen, “Tunneling matrix elements in three-dimensional space: The derivative rule and the sum rule,” *Phys. Rev. B*, vol. 42, pp. 8841–8857, Nov 1990.
- [47] O. Krejčí, P. Hapala, M. Ondráček, and P. Jelínek, “Principles and simulations of high-resolution STM imaging with a flexible tip apex,” *Physical Review B*, vol. 95, p. 045407, Jan 2017.
- [48] L. Gross, N. Moll, F. Mohn, A. Curioni, G. Meyer, F. Hanke, and M. Persson, “High-resolution molecular orbital imaging using a p-wave STM tip,” *Physical review letters*, vol. 107, no. 8, p. 086101, 2011.
- [49] J. A. Stroscio and W. J. Kaiser, *Scanning tunneling microscopy*, vol. 27. Academic Press, 1993.
- [50] S. Bychikhin, V. V. Potemkin, and A. Stepanov, “Estimation of tunneling-barrier width in scanning tunneling microscope from noise characteristics,” *Measurement Techniques*, vol. 42, no. 12, pp. 1187–1192, 1999.
- [51] P. Becker, P. Scyfried, and H. Siegert, “The lattice parameter of highly pure silicon single crystals,” *Zeitschrift für Physik B Condensed Matter*, vol. 48, no. 1, pp. 17–21, 1982.
- [52] W. Souder and P. Hidnert, “Thermal expansion of a few steels,” *Journal of the Franklin Institute*, vol. 194, no. 1, pp. 93–94, 1922.
- [53] P. Kocán, *Study of Heteroepitaxial Growth on Reconstructed Si Surfaces*. PhD thesis, Charles University, 2004.
- [54] J. Broughton and X. Li, “Phase diagram of silicon by molecular dynamics,” *Physical Review B*, vol. 35, no. 17, p. 9120, 1987.

- [55] E. Khramtsova, A. Zotov, A. Saranin, S. Ryzhkov, A. Chub, and V. Lifshits, “Growth of extra-thin ordered aluminum films on Si(111) surface,” *Applied surface science*, vol. 82, pp. 576–582, 1994.
- [56] J. Nogami, S.-i. Park, and C. Quate, “Indium-induced reconstructions of the Si(111) surface studied by scanning tunneling microscopy,” *Physical Review B*, vol. 36, no. 11, p. 6221, 1987.
- [57] R. Hamers, “Effects of coverage on the geometry and electronic structure of Al overlayers on Si(111),” *Physical Review B*, vol. 40, no. 3, p. 1657, 1989.
- [58] J. Kraft, M. Ramsey, and F. Netzer, “Surface reconstructions of In on Si(111),” *Physical Review B*, vol. 55, no. 8, p. 5384, 1997.
- [59] D. Chen, J. A. Golovchenko, P. Bedrossian, and K. Mortensen, “Tunneling images of gallium on a silicon surface: reconstructions, superlattices, and incommensuration,” *Physical review letters*, vol. 61, no. 25, p. 2867, 1988.
- [60] J. Zegenhagen, P. Lyman, M. Böhringer, and M. Bedzyk, “Discommensurate reconstructions of (111) Si and Ge induced by surface alloying with Cu, Ga and In,” *physica status solidi (b)*, vol. 204, no. 2, pp. 587–616, 1997.
- [61] F. Tao, Z. H. Wang, Y. H. Lai, and G. Q. Xu, “Attachment of styrene and phenylacetylene on Si(111)-7×7: The influence of substitution groups on the reaction mechanism and formation of π-conjugated skeletons,” *Journal of the American Chemical Society*, vol. 125, no. 22, pp. 6687–6696, 2003.
- [62] S. R. Schofield, S. A. Saraireh, P. V. Smith, M. W. Radny, and B. V. King, “Organic bonding to silicon via a carbonyl group: New insights from atomic-scale images,” *Journal of the American Chemical Society*, vol. 129, no. 37, pp. 11402–11407, 2007.
- [63] H. H. Tang, Y. H. Cai, Y. S. Ning, Y. H. Lai, and G. Q. Xu, “A selective [4+2]-like cycloaddition of α, β-unsaturated ketone on Si(111)-7×7,” *Surface science*, vol. 601, no. 16, pp. 3293–3302, 2007.
- [64] M. Carbone, G. Comtet, G. Dujardin, L. Hellner, and A. Mayne, “Different role of filled and empty surface states in a polyfunctional molecule adsorption: Geranyl acetone on Si(111) 7×7,” *The Journal of chemical physics*, vol. 117, no. 10, pp. 5012–5017, 2002.
- [65] N. YUESHENG, *Adsorption of some carbonyl and related compounds on Si(111)-7×7 surface*. PhD thesis, National University of Singapore, 2008.
- [66] S. R. Schofield, O. Warschkow, D. R. Belcher, K. A. Rahnejat, M. W. Radny, and P. V. Smith, “Phenyl attachment to Si(001) via STM manipulation of acetophenone,” *The Journal of Physical Chemistry C*, vol. 117, no. 11, pp. 5736–5741, 2013.

- [67] A. Janshoff, K.-P. S. Dancil, C. Steinem, D. P. Greiner, V. S.-Y. Lin, C. Gurtner, K. Motesharei, M. J. Sailor, and M. R. Ghadiri, “Macroporous p-type silicon Fabry-Perot layers. fabrication, characterization, and applications in biosensing,” *Journal of the American Chemical Society*, vol. 120, no. 46, pp. 12108–12116, 1998.
- [68] M. Schulze, M. Utecht, A. Hebert, K. Rück-Braun, P. Saalfrank, and P. Tegeder, “Reversible photoswitching of the interfacial nonlinear optical response,” *The journal of physical chemistry letters*, vol. 6, no. 3, pp. 505–509, 2015.
- [69] F. Tao and G. Q. Xu, “Attachment chemistry of organic molecules on Si(111)- $7\times7$ ,” *Accounts of chemical research*, vol. 37, no. 11, pp. 882–893, 2004.
- [70] Y. S. Ning, Y. X. Shao, and G. Q. Xu, “p-Benzoquinone on Si(111)- $7\times7$ : [6+2]-like cycloaddition,” *The Journal of Physical Chemistry C*, vol. 114, no. 23, pp. 10455–10462, 2010.
- [71] H. Mehdipour, “Single-hydrogen dissociation paths for upright and flat acetophenone adsorbates on the Si(001) surface,” *The Journal of Physical Chemistry C*, vol. 118, no. 41, pp. 23682–23689, 2014.
- [72] K. M. O’Donnell, O. Warschkow, A. Suleman, A. Fahy, L. Thomsen, and S. R. Schofield, “Manipulating the orientation of an organic adsorbate on silicon: a NEXAFS study of acetophenone on Si(001),” *Journal of Physics: Condensed Matter*, vol. 27, no. 5, p. 054002, 2014.
- [73] Y. Bu, J. Breslin, and M. Lin, “Adsorption and thermal decomposition of acetaldehyde on Si(111)- $7\times7$ ,” *The Journal of Physical Chemistry B*, vol. 101, no. 10, pp. 1872–1877, 1997.
- [74] T. Jarolímek, J. Mysliveček, P. Sobotík, and I. Ošt’ádal, “Adsorption and diffusion of Ag atoms on Si(111)-(7×7) surface,” *Surface science*, vol. 482, pp. 386–390, 2001.
- [75] H. Jeong and S. Jeong, “Diffusion of ag adatom on the H-terminated and clean Si(111) surfaces: A first-principles study,” *Physical Review B*, vol. 71, no. 3, p. 035310, 2005.
- [76] T. Noda, S. Mizuno, J. Chung, and H. Tochihara, “T4 site adsorption of Tl atoms in a Si(111)-(1×1)-Tl structure, determined by low-energy electron diffraction analysis,” *Japanese journal of applied physics*, vol. 42, no. 3B, p. L319, 2003.
- [77] K. Sakamoto, P. Eriksson, S. Mizuno, N. Ueno, H. Tochihara, and R. Uhrberg, “Core-level photoemission study of thallium adsorbed on a Si(111)-(7×7) surface: Valence state of thallium and the charge state of surface Si atoms,” *Physical Review B*, vol. 74, no. 7, p. 075335, 2006.
- [78] K. Sakamoto, P. Eriksson, N. Ueno, and R. Uhrberg, “Photoemission study of a thallium induced Si(111)-( $\sqrt{3}\times\sqrt{3}$ ) surface,” *Surface Science*, vol. 601, no. 22, pp. 5258–5261, 2007.

- [79] P. Kocán, P. Sobotík, and I. Ošt'ádal, “Metallic-like thallium overlayer on a Si(111) surface,” *Physical Review B*, vol. 84, no. 23, p. 233304, 2011.
- [80] S. D. Stolwijk, A. B. Schmidt, M. Donath, K. Sakamoto, and P. Krüger, “Rotating spin and giant splitting: Unoccupied surface electronic structure of Tl/Si(111),” *Physical review letters*, vol. 111, no. 17, p. 176402, 2013.
- [81] K. Yaji, Y. Ohtsubo, S. Hatta, H. Okuyama, K. Miyamoto, T. Okuda, A. Kimura, H. Namatame, M. Taniguchi, and T. Aruga, “Large Rashba spin splitting of a metallic surface-state band on a semiconductor surface,” *Nature communications*, vol. 1, p. 17, 2010.
- [82] K. Sakamoto, T.-H. Kim, T. Kuzumaki, B. Müller, Y. Yamamoto, M. Ohtaka, J. R. Osiecki, K. Miyamoto, Y. Takeichi, A. Harasawa, *et al.*, “Valley spin polarization by using the extraordinary Rashba effect on silicon,” *Nature communications*, vol. 4, p. 2073, 2013.
- [83] D. V. Gruznev, L. V. Bondarenko, A. V. Matetskiy, A. A. Yakovlev, A. Y. Tupchaya, S. V. Eremeev, E. V. Chulkov, J.-P. Chou, C.-M. Wei, M.-Y. Lai, *et al.*, “A strategy to create spin-split metallic bands on silicon using a dense alloy layer,” *Scientific reports*, vol. 4, 2014.
- [84] D. Gruznev, A. Zotov, and A. Saranin, “Tailoring of spin-split metallic surface-state bands on silicon,” *Journal of Electron Spectroscopy and Related Phenomena*, vol. 201, pp. 81–87, 2015.
- [85] S. Higashi, P. Kocán, and H. Tochihara, “Reactive epitaxial growth of MnSi ultrathin films on Si(111) by Mn deposition,” *Physical Review B*, vol. 79, no. 20, p. 205312, 2009.
- [86] A. Kumar, M. Tallarida, M. Hansmann, U. Starke, and K. Horn, “Thin manganese films on Si(111)-(7×7): electronic structure and strain in silicide formation,” *Journal of Physics D: Applied Physics*, vol. 37, no. 7, p. 1083, 2004.
- [87] Z.-Q. Zou, H. Wang, D. Wang, Q.-K. Wang, J.-J. Mao, and X.-Y. Kong, “Epitaxial growth of manganese silicide nanowires on Si(111)-7×7 surfaces,” *Applied physics letters*, vol. 90, no. 13, p. 133111, 2007.
- [88] Z.-Q. Zou, W.-C. Li, J.-M. Liang, and D. Wang, “Self-organized growth of higher manganese silicide nanowires on Si(111), (110) and (001) surfaces,” *Acta Materialia*, vol. 59, no. 20, pp. 7473–7479, 2011.
- [89] K. Jithesh, U. Waghmare, and S. Shivaprasad, “Experimental deduction of In/Si(111) 2D phase diagram and ab-initio DFT modeling of 2 × 3 phase,” *Applied Surface Science*, vol. 256, no. 2, pp. 348–352, 2009.
- [90] T. Ichikawa, “Structural study of ultrathin Sn layers deposited onto Ge(111) and Si(111) surfaces by RHEED,” *Surface science*, vol. 140, no. 1, pp. 37–63, 1984.

- [91] A. v. Braun and J. Tcherniac, “Über die produkte der einwirkung von acetanhydrid auf phthalamid,” *European Journal of Inorganic Chemistry*, vol. 40, no. 2, pp. 2709–2714, 1907.
- [92] M. Matsuoka, “Phthalocyanine and naphthalocyanine dyes,” in *Infrared Absorbing Dyes*, pp. 45–55, Springer, 1990.
- [93] H. De Diesbach and E. von Der Weid, “Quelques sels complexes des o-dinitriles avec le cuivre et la pyridine,” *Helvetica Chimica Acta*, vol. 10, no. 1, pp. 886–888, 1927.
- [94] M. G. Walter, A. B. Rudine, and C. C. Wamser, “Porphyrins and phthalocyanines in solar photovoltaic cells,” *Journal of Porphyrins and Phthalocyanines*, vol. 14, no. 09, pp. 759–792, 2010.
- [95] O. A. Melville, B. H. Lessard, and T. P. Bender, “Phthalocyanine-based organic thin-film transistors: A review of recent advances,” *ACS applied materials & interfaces*, vol. 7, no. 24, pp. 13105–13118, 2015.
- [96] J. Otsuki, “STM studies on porphyrins,” *Coordination Chemistry Reviews*, vol. 254, no. 19, pp. 2311–2341, 2010.
- [97] C. M. Drain, A. Varotto, and I. Radivojevic, “Self-organized porphyrinic materials,” *Chemical reviews*, vol. 109, no. 5, pp. 1630–1658, 2009.
- [98] W. Auwärter, D. Écija, F. Klappenberger, and J. V. Barth, “Porphyrins at interfaces,” *Nature chemistry*, vol. 7, no. 2, pp. 105–120, 2015.
- [99] S. Mohnani and D. Bonifazi, “Supramolecular architectures of porphyrins on surfaces: The structural evolution from 1D to 2D to 3D to devices,” *Coordination Chemistry Reviews*, vol. 254, no. 19, pp. 2342–2362, 2010.
- [100] S. Yoshimoto, “Molecular assemblies of functional molecules on gold electrode surfaces studied by electrochemical scanning tunneling microscopy: Relationship between function and adlayer structures,” *Bulletin of the Chemical Society of Japan*, vol. 79, no. 8, pp. 1167–1190, 2006.
- [101] S. Berner, M. Brunner, L. Ramoino, H. Suzuki, H.-J. Güntherodt, and T. Jung, “Time evolution analysis of a 2D solid–gas equilibrium: a model system for molecular adsorption and diffusion,” *Chemical physics letters*, vol. 348, no. 3, pp. 175–181, 2001.
- [102] I. Kröger, B. Stadtmüller, C. Stadler, J. Ziroff, M. Kochler, A. Stahl, F. Pollinger, T.-L. Lee, J. Zegenhagen, F. Reinert, *et al.*, “Submonolayer growth of copper-phthalocyanine on Ag(111),” *New Journal of Physics*, vol. 12, no. 8, p. 083038, 2010.
- [103] M. Böhringer, W.-D. Schneider, and R. Berndt, “Scanning tunneling microscope-induced molecular motion and its effect on the image formation,” *Surface science*, vol. 408, no. 1, pp. 72–85, 1998.

- [104] Y. Shi-Chao, X. Nan, G. Hui-Qi, S. Qian, G. Yang, S. Xin-Yan, and L. Xing-Hua, “Mapping the diffusion potential of a reconstructed Au(111) surface at nanometer scale with 2D molecular gas,” *Chinese Physics Letters*, vol. 29, no. 4, p. 046803, 2012.
- [105] M. Böhringer, K. Morgenstern, W.-D. Schneider, and R. Berndt, “Reversed surface corrugation in STM images on Au(111) by field-induced lateral motion of adsorbed molecules,” *Surface Science*, vol. 457, no. 1, pp. 37–50, 2000.
- [106] S. Stranick, M. Kamna, and P. Weiss, “Atomic-scale dynamics of a two-dimensional gas-solid interface,” *Science*, pp. 99–99, 1994.
- [107] Z. Suo and W. Hong, “Programmable motion and patterning of molecules on solid surfaces,” *Proceedings of the National Academy of Sciences of the United States of America*, vol. 101, no. 21, pp. 7874–7879, 2004.
- [108] K. Cui, O. Ivasenko, K. S. Mali, D. Wu, X. Feng, K. Müllen, S. De Feyter, and S. F. Mertens, “Potential-driven molecular tiling of a charged polycyclic aromatic compound,” *Chemical Communications*, vol. 50, no. 72, pp. 10376–10378, 2014.
- [109] F. P. Cometto, K. Kern, and M. Lingenfelder, “Local conformational switching of supramolecular networks at the solid/liquid interface,” *ACS nano*, vol. 9, no. 5, pp. 5544–5550, 2015.
- [110] S.-B. Lei, K. Deng, Y.-L. Yang, Q.-D. Zeng, C. Wang, and J.-Z. Jiang, “Electric driven molecular switching of asymmetric tris (phthalocyaninato) lutetium triple-decker complex at the liquid/solid interface,” *Nano letters*, vol. 8, no. 7, pp. 1836–1843, 2008.
- [111] X.-M. Zhang, Q.-D. Zeng, and C. Wang, “Reversible phase transformation at the solid–liquid interface: STM reveals,” *Chemistry—An Asian Journal*, vol. 8, no. 10, pp. 2330–2340, 2013.
- [112] S. V. Snegir, P. Yu, F. Maurel, O. L. Kapitanchuk, A. A. Marchenko, and E. Lacaze, “Switching at the nanoscale: Light and STM-tip-induced switch of a thiolated diarylethene self-assembly on Au(111),” *Langmuir*, vol. 30, no. 45, pp. 13556–13563, 2014.
- [113] G. Pace, V. Ferri, C. Grave, M. Elbing, C. von Hänisch, M. Zharnikov, M. Mayor, M. A. Rampi, and P. Samori, “Cooperative light-induced molecular movements of highly ordered azobenzene self-assembled monolayers,” *Proceedings of the National Academy of Sciences*, vol. 104, no. 24, pp. 9937–9942, 2007.
- [114] B. Wortmann, D. v. Vörden, P. Graf, R. Robles, P. Abufager, N. Lorente, C. Bobisch, and R. Möller, “Reversible 2D phase transition driven by an electric field: visualization and control on the atomic scale,” *Nano letters*, vol. 16, no. 1, pp. 528–533, 2015.
- [115] Y. Zhang, H. Kersell, R. Stefak, J. Echeverria, V. Iancu, U. Perera, Y. Li, A. Deshpande, K.-F. Braun, C. Joachim, *et al.*, “Simultaneous and coordinated

rotational switching of all molecular rotors in a network,” *Nature nanotechnology*, vol. 11, no. 8, 2016.

# List of Abbreviations

**AP** acetophenone. 27

**CuPc** copper phthalocyanine. 4, 62, 76, 95

**DAS** dimer-adatom-stacking fault. 6, 24, 43

**DOS** density of states. 8, 9, 12

**F<sub>16</sub>CuPc** copper hexadecafluoro-phthalocyanine. 62, 63, 64, 76, 95

**HUC** half-unit-cell. 24, 27, 42

**KMC** kinetic Monte Carlo. 4, 64, 76

**LDOS** local density of states. 13, 14

**ML** monolayer. 42, 43, 50, 59

**MPcs** metalo-phthalocyanines. 4

**SPM** Scanning Probe Microscopy / Scanning Probe Microscope. 6, 63

**STM** Scanning Tunneling Microscopy / Scanning Tunneling Microscope. 4, 6, 7, 9, 13, 16, 17, 18, 19, 21, 22, 24, 25, 27, 44, 50, 62, 63, 64, 76, 95

**STS** Scanning Tunneling Spectroscopy. 4, 27

**UHV** ultra-high vacuum. 21, 76

**VAC** volt-ampere characteristic. 13, 14

# Nomenclature

$d_{ts}$  tip-sample distance

$n(x, y)$  time-averaged density of molecules at the position (x, y)

$p_m(x, y)$  probability of finding a molecule at the position (x, y)

$V_T$  threshold voltage for the order/disorder transition of CuPc molecules

$V_{ts}$  tip-sample voltage